ATOMIC LAYER ETCHING OF METAL FILMS, METAL NITRIDES, AND METAL OXIDES WITH BCL_3 AND HF/XEF_2

by

Nicholas Johnson

A.A., Santa Rosa Junior College, 2011

B.S., UC Santa Barbara, 2013

A thesis submitted to the

Faculty of the Graduate School of the

University of Colorado in partial fulfillment

of the requirement for the degree of

Doctor of Philosophy

Department of Chemistry and Biochemistry

2018

This thesis entitled:

Atomic Layer Etching of Metal Films, Metal Nitrides, and Metal Oxides with BCl_3 and HF/XeF_2

written by Nicholas Johnson

has been approved for the Department of Chemistry and Biochemistry

Professor Steven M. George

Professor Michael Marshak

Date

The final copy of this thesis has been examined by the signatories, and we find that both the content and the form meet acceptable presentation standards of scholarly work in the above mentioned discipline.

Johnson, R, Nicholas (Ph.D., Chemistry)
Atomic Layer Etching of Metal Films and Metal Nitrides

Thesis directed by Professor Steven M. George

The continued miniaturization and increase in architectural complexity of transistor-based devices require new process methods. One such method is called atomic layer etching (ALE). ALE is based upon sequential self-limiting or pseudo-self-limiting reactions that remove materials with atomic level control. Until recently, ALE was based upon halogen adsorption followed by high energy ion bombardments for isotropic (directional) etching of materials. However, recently, new thermal based techniques have been developed for anisotropic (non-directional) etching of semiconductor-based devices.

New approaches for thermal ALE have been demonstrated for crystalline AlN, W/WO_3, TaN/Ta_2O_5, MOCVD GaN and Ga_2O_3. Crystalline AlN was demonstrated to etch with $Sn(acac)_2$ and HF as the reactants. WO_3, Ta_2O_5 and Ga_2O_3 were demonstrated to etch with BCl_3 and HF. TaN and W were etched with O_2/O_3 in conjunction with BCl_3 and HF. MOCVD GaN was etched with BCl_3 and XeF_2.

All systems were analyzed with spectroscopic ellipsometry as the main technique for thickness analysis. Thermal ALE of all systems was shown to be possible in the general temperature range of 150 to 250 ^{o}C. Investigations into the reaction pathway were conducted for each system. Ga_2O_3, MOCVD GaN, and AlN proceeded through a fluorination and ligand exchange. In this process, the surface is fluorinated, and the resulting fluoride is transferred for the ligand on $Sn(acac)_2$ or BCl_3 creating volatile complexes. In the case for WO_3 and Ta_2O_5,

BCl_3 converts the surface to a B_2O_3 layer while forming volatile metal chlorides. B_2O_3 is then spontaneously removed by interaction with HF which does not fluorinate WO_3 or Ta_2O_5. This pathway is important when a fluorination step would create volatile fluorides leading to non-controlled spontaneous etching. TaN and W are etched similarly, except that an oxidation step is required. The thermal ALE of other metal derivatives such as metal phosphides, sulfides, tellurides and elemental metals can be etched through these two pathways.

Acknowledgements

First and foremost, I would like to thank my advisor, Professor Steve George. He has always engaged with me in thoughtful conversations and guided me through difficult times in my graduate career. He has allowed me to experiment with unusual ideas backed up with chemical intuition. In fact, most of my papers are a result of these ideas. Throughout the years here in the George group, I have had the best time with my fellow students and post-docs. I want to thank Andrew Cavanagh for always making time for me to help with XPS, random but helpful conversations, and for being a friend. Dave Zywatko, and Tyler Meyers for all the adventures outside the lab, as well as general help when I needed it. Jess Murdzek for running XRR/XRD experiments as well as growing films for me. Jasmine Wallas for the help through the years. Austin Cano for being my desk buddy. Brian Welch for taking over the lab proctoring and doing a great job. Joel Clancey for helping me get into the George group as well as always being helpful. I'm thankful for the past George group members as well for all their help/insightful viewpoints throughout the years. I want to thank my collaborators from Intel, IBM, TEL, their insight has been so helpful. Also a thank you to my friends outside of the lab. They kept me sane throughout the years. I also want to thank my parents and my sister. They have always pushed me and never let me limit myself. Although thanking is not a strong enough term, I want to thank my lucky lady Laura Smith. Through the nearly 4 years we have been together she has listened to me babble about work, been with me when I was stressed for a deadline and was and still is the foundation of support that I need. This work was funded by DARPA and the Semiconductor Research Corporation.

CONTENTS

CHAPTER

Tables

Figures

Chapter 1

INTRODUCTION

1.1 History of the Transistor

In the last century there has been many inventions that have brought mankind from the Stone Age to now, where we are in the Technological Age, or “Silicon Age.” Inventions such as the assembly line and Model T by Henry Ford, the discovery of penicillin, and the first radios and televisions have changed how society functions. These inventions deserve their due credit; however, it can be argued one of the most important inventions that has been discovered is the computer. Today in society, computers are everywhere. Computers allowed for cellphones to be invented, computers access the internet, help in education, and computers help run calculations for a multitude of applications that would take days if not longer to solve by hand.

To appreciate how important ALE methods are to the semiconductor industry, it is important to know the history of computers. The first digital computers had a large number of vacuum transistors for calculations. The first experimental digital computers such as the Atanasoff-Berry Computer used 300 vacuum tube transistors with capacitors used for the memory. Computers were soon used by the military for cracking codes of enemies, primarily the Germans in WW2[1]. This led to the invention of the computer Colossus Mark 1 which contained 1500 vacuum tube transistors for calculations. The Colossus Mark 2 was later invented with 2400 vacuum tube transistors for calculations. The size of these first computers was incredibly large. The Colossus Mark 2 was 7ft high by 17ft wide and 11 feet deep.

Computer language is based upon 1’s and 0’s, or on/off in colloquial terms. This type of language uses Boolean algebra to perform calculations. As the language for Boolean algebra is “on” or “off” a system can be designed to designate these values with components that have only two states. This is the primary reason that transistors are used in computers. A transistor is an electrical switch. At the time, vacuum transistors, which are an electrical switch satisfied the on/off conditions. The flow of the electrical current during an on state, or the lack thereof was then used to perform calculations. During this time, the only type of reliable transistor was vacuum tubes, hence, why they were used, even with their drawbacks (more on that later)

The reason for the size of these computers were the components. Each computer had thousands of resistors, capacitors and miles worth of wiring. Each vacuum transistor being the size of a small coke can added up. If we glance at a computer now, the size is miniscule in comparison, but the processing speed for even low-cost computers is astronomically larger. The size difference is that the components of computers system have gotten smaller and smaller. One main difference between the first computers and todays computers is that vacuum tube transistors aren’t use anymore.

Invention of the Field Effect Transistor and creation of solid state FET computers

In the late 1940’s three scientists at Bell Labs created a working solid-state transistor. Using germanium as the semiconductor, and gold as the contacts, and a metal base; John Bardeen, William Shockley, and Walter Brattain discovered the first point contact transistor.[2] In doing so they also invented the first Field Effect Transistor. The Bell Labs team noticed that the potential applied to the gate electrode controlled the current through the contacts.

At the time of the discovery of the solid state transistor, tubes were still in use for early computers. However, tubes required a significant amount of power to turn on, generated an immense amount of heat, and broke down frequently[3]. For computing to continue to become more powerful, more tubes would be necessary, however, the constant breakdown and amount of power needed for run time made these machines expensive to run. A replacement was needed. When Bell labs discovered the point contact transistor, they also showed that the device required low power for on/off operation, had a long lifetime of use, and it was significantly smaller than vacuum tubes[2].

It was only a matter of time until transistors replaced computers. In 1953, the first computer made entirely of solid state transistors was invented at Sussex University by Dick Grimsdale, a research student in electrical engineering[4]. This system was far more efficient than vacuum tube systems, and much faster. Eventually companies started making solid state transistor computers. In 1955 IBM came out with the first transistor calculator containing 3000 germanium transistors. Companies such as Philco, RCA, Olivetti and IBM then released transistor-based computers in the following years.

Early computers used germanium as the semiconductor material, however transistor technology switched to silicon[5]. This is primarily due to Bell Labs investigating silicon as the semiconductor material, and single crystal silicon's ease of development. At this same time, Texas instruments also created working silicon transistors. With the two largest suppliers of transistors researching and developing silicon based transistors, the devices switched from germanium to silicon.

The point contact transistor was the first solid state transistor used in computer devices. This type of transistor was eventually replaced by a junction gate field-effect-transistor JFET called the static induction transistor (SIT). A JFET is a type of transistor where the source and drain are connected and current flows. A schematic of the JFET is shown in Figure 1-1. When a bias is applied, the conduction channel is changed from n-type to p-type or vise versa stopping the current and the switch is effectively turned off. This then lead to the invention of the metal-oxide-semiconductor field-effect transistor (MOSFET) shown in figure 1-2. This device works in opposite to the JFET. No current is flowing until a bias is applied to the gate. An additional architectural change was completed as well, the gate is now insulated from the conduction channel so no current would travel through the conductive gate as shown in figure 1-2

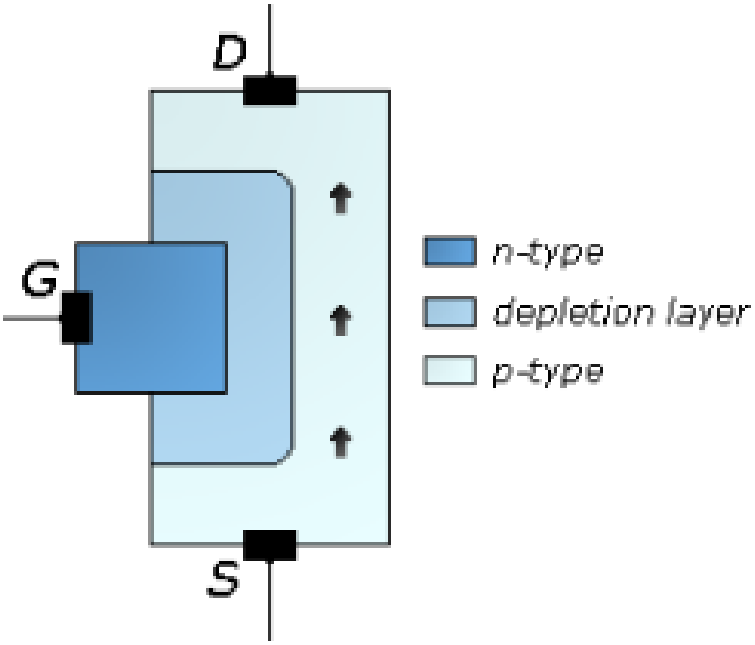

Figure 1-1. Schematic of a Junction Gate Field Effect Transistor[6]

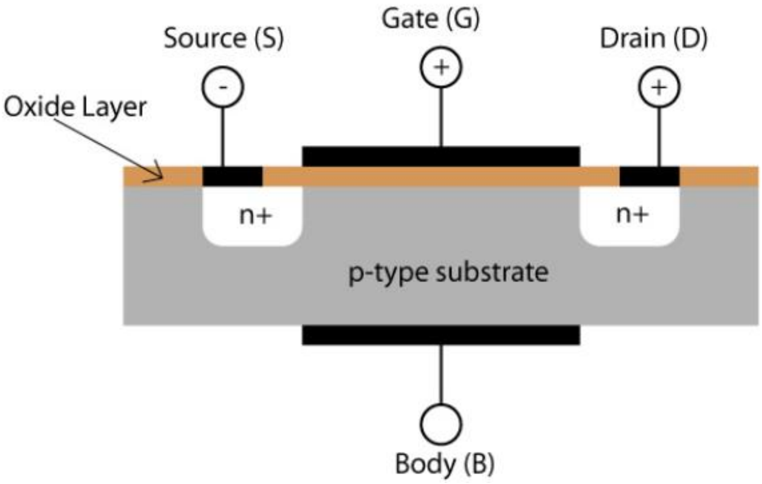

Figure 1-2. Schematic of a MOSFET[7]

The MOSFET has been the chosen transistor device for the last 50 years in computer devices. In comparison to other types of transistors such as the bipolar junction transistor, the MOSFET exhibits better thermal stability. In addition, a MOSFET requires little voltage to open the conduction channel. In comparison to the JFET, the MOSFET doesn't have free flowing current through the channel, making it more efficient in current consumption. MOSFET devices can also handle higher current loads than BJT's[8].

The transition from Vacuum tubes to point contact transistor to the MOSFET was based upon a few factors: efficiency, reliability but most importantly size. The decrease of size correlated to an ability for faster switching of the transistors, lower power consumption and greater computing ability due to far greater transistor density. With these factors, integrated circuits were being researched and developed. Initial transistor devices were made individually and wired together. Integrated circuits removed the individual components from a separate substrate to the same substrate. This allowed for the packing density of transistors to increase as well as decrease use of bulky wiring.

The development of integrated circuits led to the decrease of transistor price, and the increase of transistors per unit area. This observation was famously noticed by Gordon E. Moore, where he stated that the amount of transistors per unit area would double approximately every two years[9]. He also noted that the price per transistor would ultimately drop as the number of components per unit area increased. This increase of transistors per unit area would also increase processing speed and decrease price[9]. From Moore's paper, it is evident that there will be a continued increase of components per unit area, or a decrease of transistor size and distance between each other.

The dimensions of a transistor are important to understand what is meant by a size reduction of the node. Figure 1-3 shows a schematic of a MOSFET with its components labeled. The dimensions that are reported for a are the device pitch, gate length, and node length (half pitch). The device pitch is the physical length between the contacts, the gate length is the gate width, half pitch is the approximately half the distance of the pitch. When companies report the dimensions of transistor devices they report the node length. The node length is approximately ½ the pitch length. Why companies do not just report the physical dimensions of the transistor produced rather than state pitch which isn't a concrete dimension, is unknown.

In 1971 a MOSFET had a node length of 10,000 nm, or approximately 20,000 nm pitch length[10]. The number of transistors per unit area was 2300. In 2012 the transistor node dimension was 22nm and the transistors per unit area was $1.4x10^9$ transistors[10]. Moore predicted that the number of transistors on each chip would increase and the size of each would decrease. For transistor devices to decrease in size, new process technology/steps would have to be developed. The number of processing steps that go into the creation of one MOSFET is extensive.

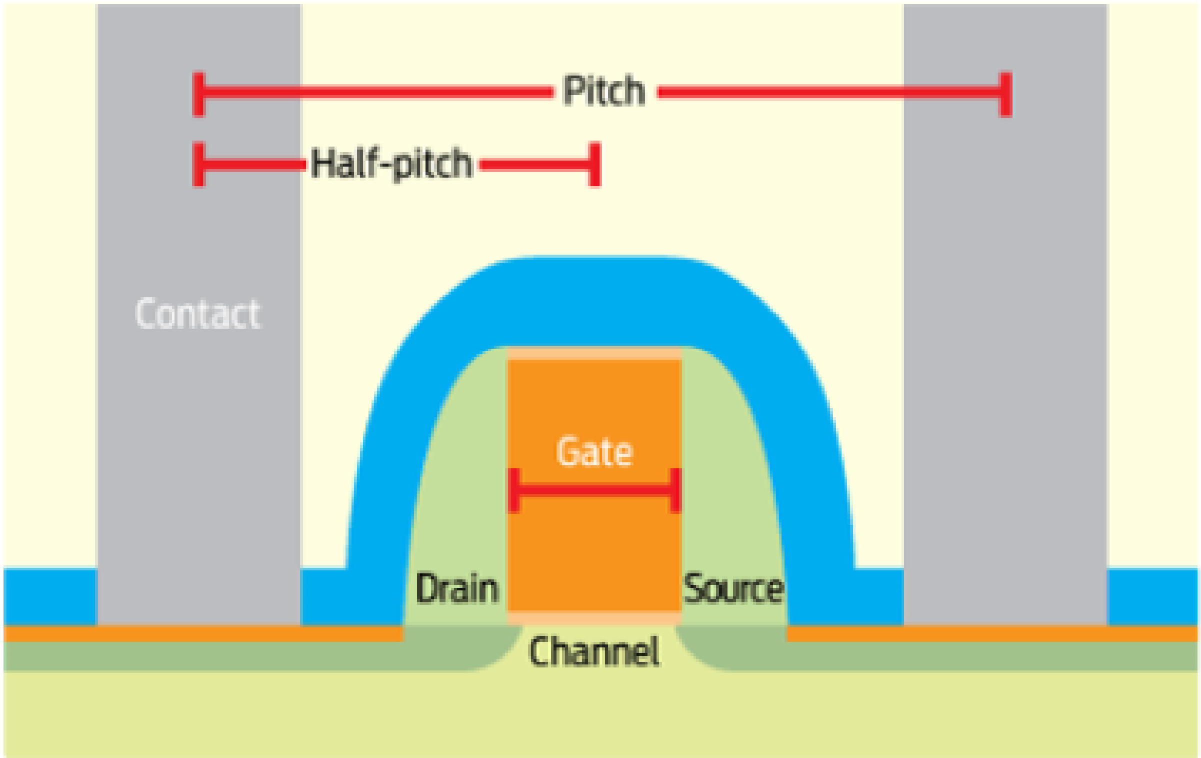

Figure 1-3. Diagram depicting correlation pitch and half-pitch (node)

1.2 Etching Techniques

There can hundreds of steps to produce a working microchip[10]. In figure xx., only a few steps of a CMOS MOSFET device are shown. This figure excludes steps pertaining to lithography of which there are several between each shown step. The figure overlays three important processes for CMOS production: ion implantation, deposition, and etching. Each technique has been critical for the continued miniaturization of CMOS devices from the 10,000 nm node in 1971 to the 22 nm node in 2012.[11-13] A thesis could be written on each individually, however, for this thesis, thermal etching techniques are its focus.

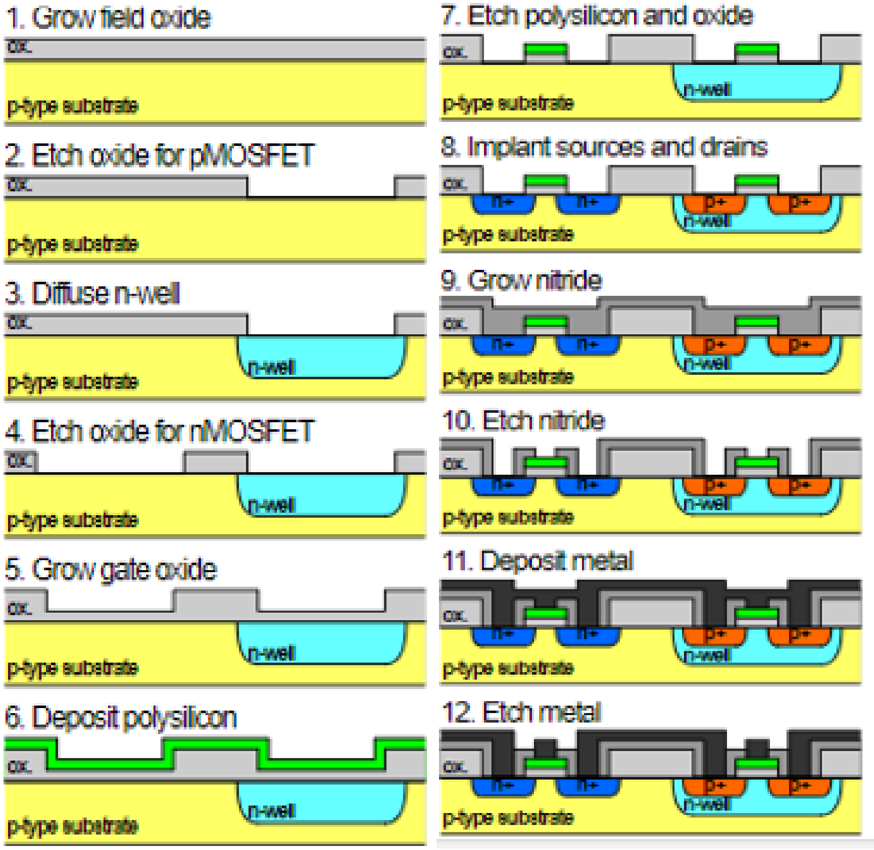

Figure 1-4. Examples of the steps taken to make a transistor device

Etching techniques have been critical to device fabrication over the years[11, 14-15]. This section will focus on dry etching techniques. Dry etching can be broken down into two different subsets: Atomic layer etching (ALE) and continuous etching. Atomic layer etching is a sequential self-limiting or pseudo self-limiting reaction process based upon thermal or plasma-based reactions[11, 14-15]. Continuous etching can be a thermal etch method or a plasma-based method. Figure 1-5 shows the saturation behavior of ALE and continuous etching methods. a,b are both saturating, c is pseudo-saturating and d is continuous etching with no saturation.

Each method of etching whether ALE based or continuous based falls into the category of isotropic (non-directional) etching, or anisotropic (directional) etching. A comparison of anisotropic and isotropic etching is shown in figure 1-6. Isotropic etching will cut under the mask, whereas, anisotropic etching will stay in line with the mask. Anisotropic etching is necessary for FINFET fabrication, or where linear device geometry is importatnt.[15] Isotropic etching will be necessary for etching in a 3D fashion or large aspect ratios[15].

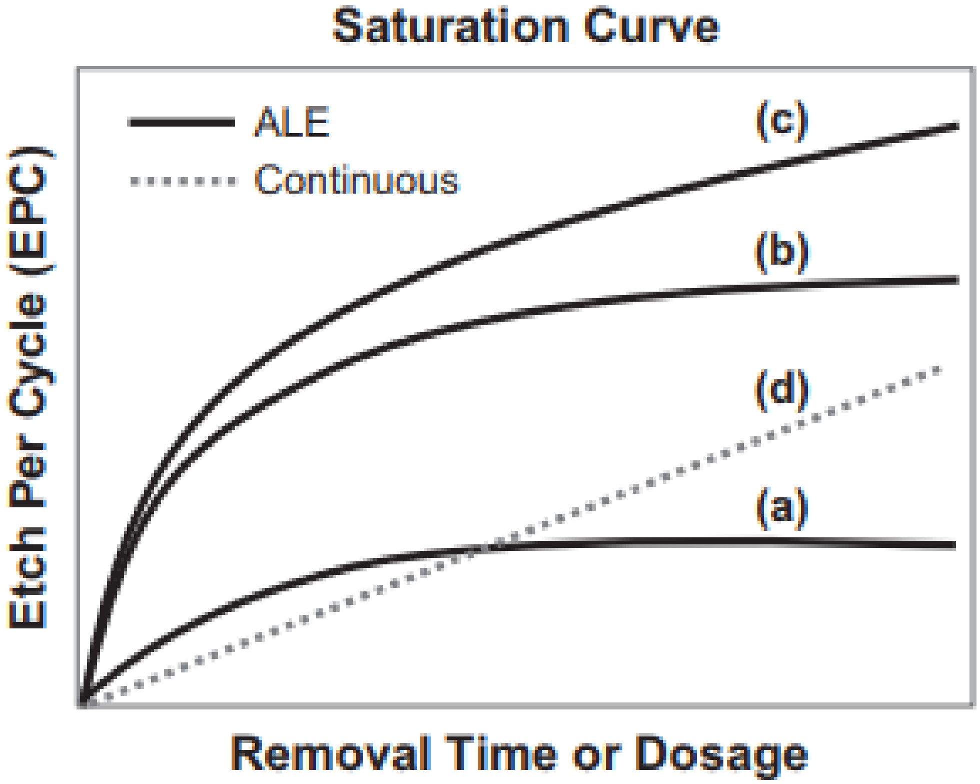

Figure 1-5. Saturation curves for ALE processes. (a) and (b) are both self-limiting, (c) is pseudo-self-limiting as the etch does not stop with increase dosage time but only slows, and (d) shows no saturation and is a continuous etch[14]

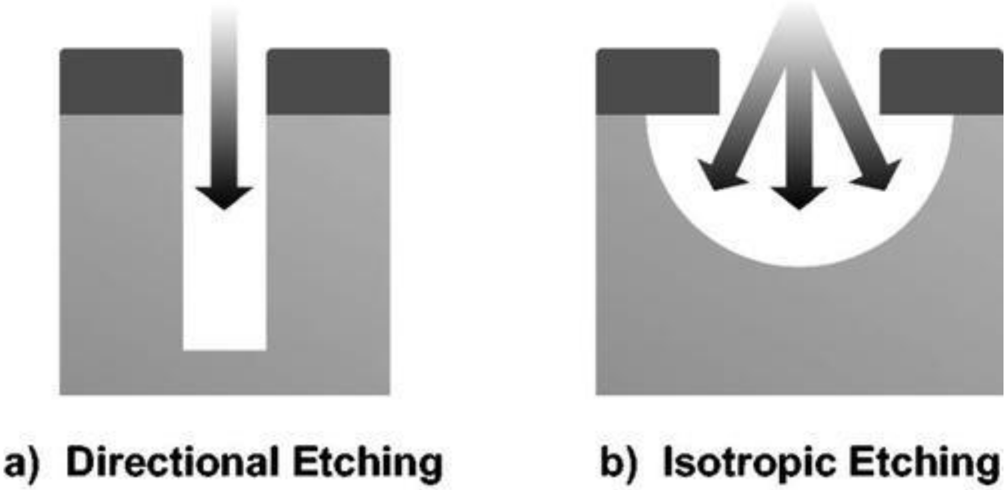

Figure 1-6. Depiction of the two types of etching. Directional etching or anisotropic etch has a greater removal of material in one direction with almost no etch laterally and isotropic etching where the etch rate is equal in all directions.[14]

1.2.1 Continuous Etching

Continuous etching can be either plasma or thermal based. The most famous type of thermal based spontaneous isotropic etching is that of Si with XeF_2.[16] This method is useful as it causes little damage to the electrical properties and can be used for releasing free standing Si, Ge, SiGe structures[14]. This method is always isotropic. The other type of continuous etching is plasma-based methods. Both useful for releasing free standing structures, however etch rates are in general faster than thermal based spontaneous methods[16]. Additionally, etching only occurs while the plasma is discharging. The two general types of plasma-based methods are halogen/gas mixtures etching, or physical sputter etching. Examples of halogen based methods are SF_6, CF_2H_2/O_2, BCl_3 which can be used to etch W, SiN, Si, HfO_2, ZrO_2, TiN and many others[14, 17]. These methods can vary from highly anisotropic to isotropic and also can etch specific materials selectively. Physical sputter etching is a technique that is in general highly anisotropic, but not selective. Physical sputter etching is based upon sending fast moving ions towards the surface and blasting the material away. Examples of physical sputter etching are Pt with an O_2/Cl_2 mixture[18], and Co, Fe, Ni with a CO/NH_3 mixture[19]

The continuous etch process although useful, have drawbacks. The control of continuous etchings can range on the order of nm to microns per second[14, 18-19]. As mentioned earlier, the dimensions of device structures are on the order of 20 nm as of 2014 and as of 2018 on the order of 7nm. The control of the etch rate, and overall amount of material etched is incredibly important. Without this, small device structures could be removed completely. Luckily atomic layer etching is a new technique that can be used for small device structures. This is a technique that the semiconductor industry has been in great need of[14].

1.2.2 Atomic Layer Etching

Atomic layer etching is a technique with great etch control; one with etch rates on the order of an atomic layer. ALE is important for the continued miniaturization of device structures. The tolerances for devices are now going to be on the order of a few atoms[15]. ALE's excellent control of etch rates will be able to meet the strict device dimension requirement. In addition to the control that atomic layer etching gives, another important aspect of this technique is its selectivity. The amount of materials that have been introduced into the semiconductor industry has increased with multiple materials on each wafer. Current continuous etching techniques cannot meet the strict selective etch that is required, but ALE can[14-15, 20]. Another attribute of ALE that is necessary for the semiconductor industry is its ability to leave a miniscule amount of impurities on the surface and keeps proper electrical properties for device function. In contrast, continuous etch processes have been shown to leave impurities 20nm deep into the etched film altering electrical properties[14].

Atomic layer etching is based upon sequential, self-limiting/pseudo-self-limiting reactant exposures separated by a purge. The sequence for ALE can be represented as ABABAB where between A and B there is a purge step. A general scheme for ALE is shown in figure 1-7. The first step (A) of an ALE process is to modify the reactant surface. This step can range from a change in oxidation state i.e. $Si \rightarrow SiCl_x$ or an adsorption of a chemical species on the surface that interacts with the underlying surface i.e. C_4H_8[21-22] or CHF_3[21]. The next step is to remove any excess species that were used to modify the surface that could react with the reactant in step B. Additionally, this removes any further surface modification by residual reactant A during the etch step allowing for a greater control of the etch rate. In the second step (B) of an ALE process, the modified surface is removed by interacting with reactant B leaving a pristine or near pristine original surface. In the case of SiO_2 a fluorocarbon layer is removed by Ar or O_2 ions.[21-22] Another purge occurs after step B. This can be repeated in a cyclical fashion for continual removal until the desired thickness is achieved. It should be noted that atomic layer etching is a misnomer. Etch rates of materials can be, depending on the chemistry, less than or greater than one atomic layer per cycle, but on the order of one atomic layer.

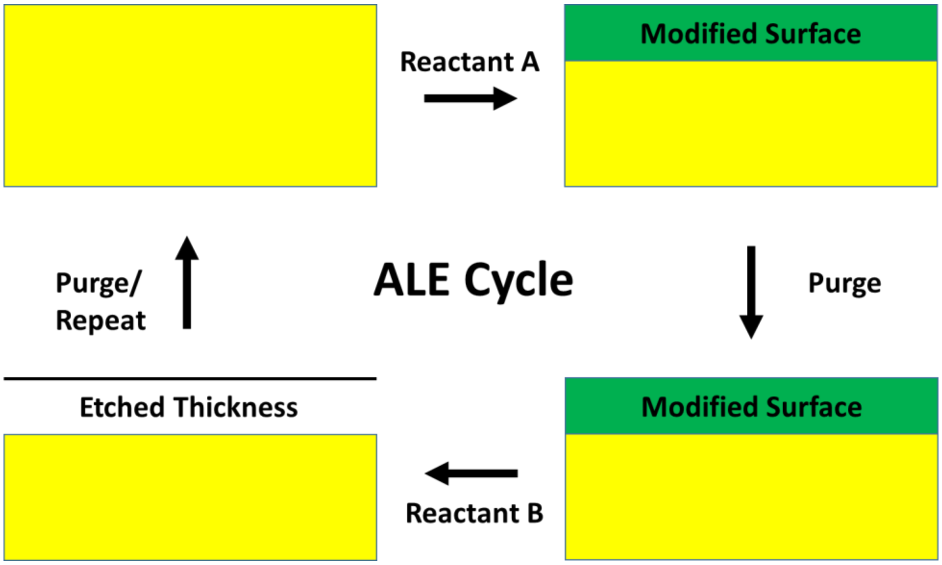

Figure 7. Schematic representing a full ALE cycle. Step 1 is introducing the surface to reactant A that changes the chemical nature of the initial surface. A purge step to remove excess reactant A. The modified surface is then interacted with reactant B which etches away that surface leaving a thinner film. A purge follows to remove reactant B from the chamber.

The concept and practice of atomic layer etching has been around for nearly 30 years. Atomic layer etching has been called many names such as: digital etching, monolayer chemical beam etching, atomic layer removal and many others.[14] The first atomic layer etching process published was ALE of diamond[23]. This then lead to the ALE of Si[24], GaAs[25] and Ge[26]. Dielectric materials such as HfO_2[27], TiO_2[28] and Al_2O_3[29] were also etched through ALE pathways. Atomic layer etching can go through two different processe:, thermal or plasma.

Plasma Based ALE

In these last 30 years ALE has in general been based upon a surface modification by halogen adsorption followed by Ar^+ ion bombardment. In the case of Si etching, Cl_2 adsorption onto the surface followed by Ar^+ ions led to etching of Si[24]. What was noticed by studying this process was the adsorption of Cl_2 on Si formed $SiCl_x$ surface on top of the Si. The Si-Cl bond is stronger than the Si-Si bond, however, due to the electronegativity of the chlorine, the transfer of electrons towards the surface lowers the Si-Si bond immediately below the chlorinated surface[30]. Ar^+ ion energy is then tuned to an energy that removes only the modified surface but does not physically sputter the Si surface underneath. This method of halogen adsorption followed by ions, or neutrals removing the modified surface is the main approach for atomic layer etching. It also allows for selective etching of one material over the other. This is the case for SiO_2 etching over Si_3N_4[31] and vice-versa[32]

The main application for plasma based ALE techniques is its anisotropic nature. This allows for near linear trench structures being formed. Steps 7, 10 and 12 show how the anisotropic nature can be useful for device fabrication. Anisotropic etching is important for MOSFET architecture as it’s changing from 2D to 3D bringing technology to the finFET shown in figure 1-8. The change from the gate being in contact with the high k one side to three sides is due to lower power consumption for operation and faster speeds[33]. It's important for the anisotropic nature of the ALE to keep fin architecture as its imperative for device function[14-15, 20].

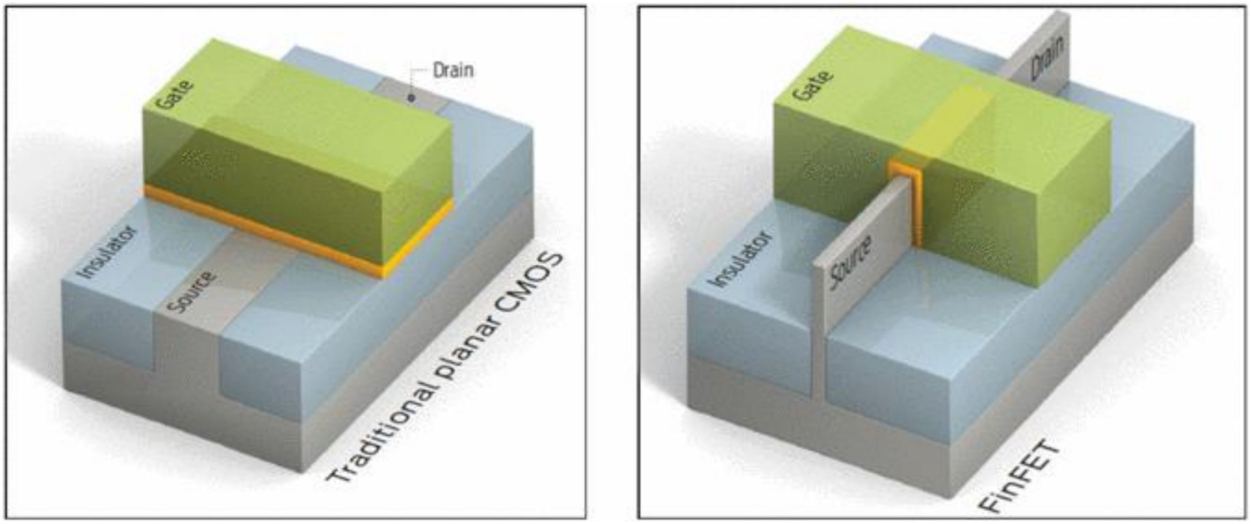

Figure 1-8. 3D diagram of traditional planar CMOS (MOSFET) and FinFET where the gate has three sides of contact on the dielectric.[34]

Most plasma based atomic layer etching processes have their limitations. They are mainly anisotropic, and can induce line edge roughness, surface impurities, and surface defects that will effect device performance[14-15, 20]. A procedure that can clean up the roughness and surface defects/impurities from conventional plasma ALE has in general been wet etch based chemistries. Wet etching is useful as an isotropic etching technique; however, miniaturization of device structures creates fragile structures that can collapse due to the capillary forces of the wet etch[15]. Wet etching also has issues of reproducibility when aspect ratios are high or spaces are tight. A gas phase technique that is anisotropic and thermal is of incredible use as a replacement for wet etching.

In addition to a replacement of wet etching, a gas phase thermal ALE process will be critical in the formation of gate all around trasistors (GAA)[15]. A stack of GAA or nanowire transistor is shown in figure 1-9. The gate wraps completely around the dielectric material and conductive channel giving the transistor faster on/off switching and lower power consumption. An issue with GAA transistors using plasma-based ALE is the top of the Si wire receives a higher flux of plasma based species than the bottom. Further complications for GAA transistor production with Plasma based ALE techniques is the harsh plasma conditions on nanowires only a few nm across. The development of a completely thermal etch process that is isotropic with greater atomic control will be necessary for these types of devices.

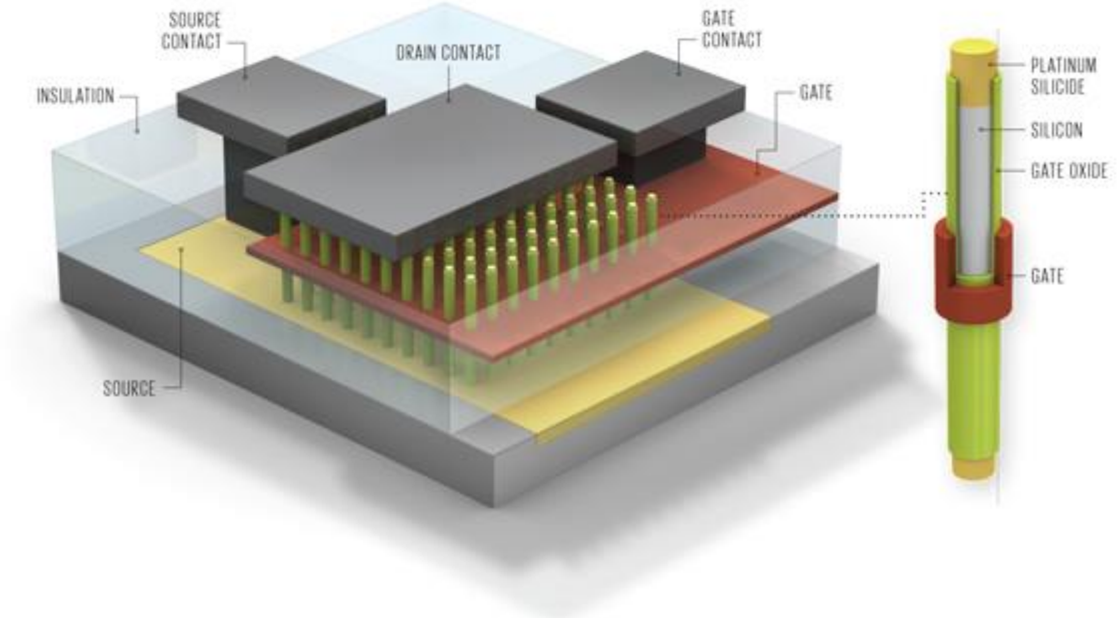

Figure 1-9. Nanowire transistor shown to the left where the gate wraps around all sides of the dielectric materials. An integrated cuircuit showing a device made out of multiple nanowire transistors (GAA)

A last point showing the necessary need for a thermal based ALE process is selectivity. Research methods with a plasma-based ALE technique do have selectivity for etching one material over the other, nonetheless, each material generally etches. A case for this is work on SiO_2 and Si_3N_4 using $C_xF_yH_z/Ar^+$ plasmas.[21, 32] One etches faster than the other but they both etch. The ability to tune the modification step of one material over the other and design specific ligands thus creating selective etching to only the desired material is probably the largest application for thermal ALE[14, 20].

Until recently it seemed that the prospects for a sequential self-limiting would have to wait as there were no journal publications on thermal ALE until 2015. It was by accident that the first thermal ALE process was discovered. In 2015 Younghee Lee was investigating the ALD of SnF_2 with Sn(acetylacetonate)$_2$ and HF on an Al_2O_3 surface. When reaching temperatures 150 ^{o}C and above, the QCM showed a mass decrease corresponding to etching.[35] This first publication sparked a new field of ALE based upon sequential self/pseudo-self-limiting thermal reactions

The first proposed mechanistic process that was discovered for thermal ALE has been shown in Figure XX. The initial aluminum oxide surface is converted to an aluminum fluoride surface. This aluminum fluoride surface is then exposed to Sn(acac)$_2$ which etches away the aluminum fluoride layer, leaving an Al_2O_3 surface.[36] This process of Sn(acac)$_2$ and HF has been used to etch AlF_3[37], HfO_2[38], ZrO_2[39].

1.3 Overview of Remaining Chapters

Chapter 2 is the experimental techniques. Chapter 3 is ALN ALE with HF and $Sn(acac)_2$. Chapter 4 is WO_3/W ALE with BCl_3/HF. Chapter 5 is TaN/Ta_2O_5 ALE with BCl_3/HF. Chapter 6 is MOCVD GaN ALE with BCl_3/XeF_2. Chapter 7 is Ga_2O_3 ALE with BCl_3/HF

Chapter 2

EXPERIMENTAL TECHNIQUES

2.1 Spectroscopic Ellipsometry

Spectroscopic ellipsometry (SE) is an optical technique measuring changes in polarized light after reflection from a thin film. S and P polarized light are shown onto a sample: upon interaction, the polarization of the light changes from linearly polarized to elliptically polarized light. The change from linear to elliptical is a result of a change in angle and magnitude of polarization vector for S and P light. The amplitude ratio (Ψ) and the angle between (Δ) S and P polarized light, are the two variables measured by ellipsometry. From these two variables, information such as optical constants, film thickness, roughness, crystallinity and other properties can be determined. Figure 2-1 is a picture of the S and P polarized light and its interaction with a thin film.

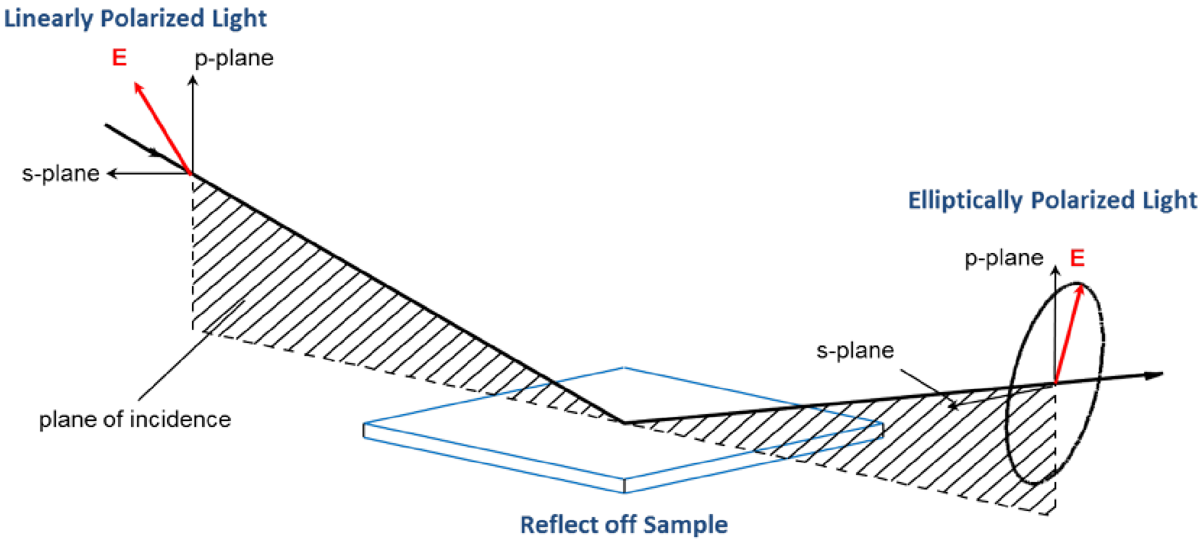

Figure 2-1. Diagram depicting linearly polarized light shown onto a sample that is reflected and changed to elliptical polarization.[40]

In order to understand the basics of ellipsometry and how it measures optical properties and thickness, it is important to understand a few concepts. The concepts that need to be understood are: light and matter interaction on a macro and atomic level, polarization of light, and optical constants n, k, ε. The following paragraphs will be broken down into those three sections. This discussion does not cover in depth all the math necessary for deriving equations used in ellipsometry. A more in depth analysis can be found in Spectroscopic Ellipsometry: Principles and Applications by Hiroyuki Fujiwara.

2.1.1 Polarization of Light

Shown below in figure 2-2 is examples of two light waves (without the B field shown) and how they appear with respect to polarization. All of these are poloarized, however, the type of polarization is dependent upon the angle between the two waves. If the two waves are offset by 45^{o} with respect to (w.r.t.) the sin wave, then they circularly polarized. If they are 0^{o} w.r.t. the sin wave, they are linearly polarized. Any angle in-between results in elliptically polarized light.

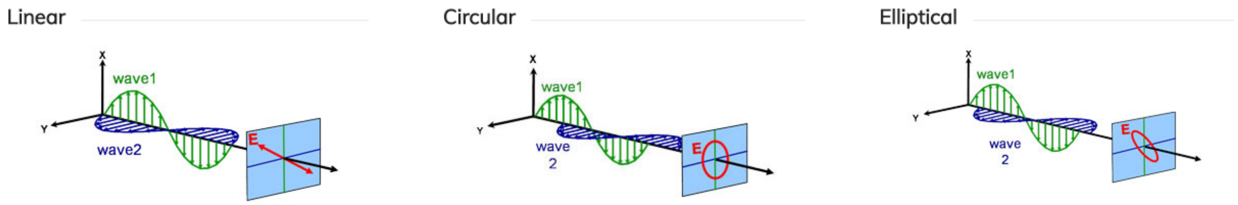

Figure 2-2. Combinations of orthogonal waves exhibiting polarization. The B field of light is omitted for clarity.[41]

2.1.2 Interaction of Light and Materials

Snells law describes the relationship between index of refraction and refracted angles. Shown below in Figure **xx** is how incident light refracts and reflects in a medium. It also has the relationship between the angle of refraction and the index of refraction at an interface of two media. Incident light is shown unto the medium at an angle of θ_i. Part of the light is refracted and travels into the medium at an angle θ_t. The other part of the light is reflected at an angle θ_r. The transmitted wave will also reflect and refract at the interface of the bottom of the medium.

$$n_i \sin\theta_i = n_t \sin\theta_t$$

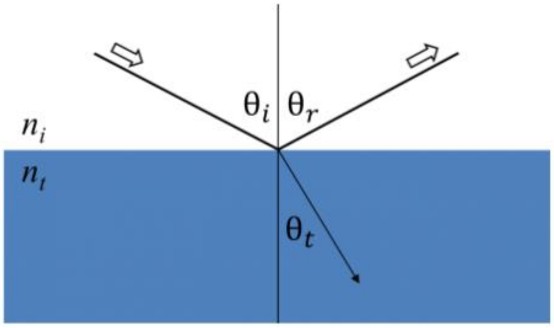

Light reflects and refracts according to Snell's law.

Figure 2-2. Snell's law of light reflecting and refracting on a surface.[42]

This process continues at each new interface of two or more media. To further understand how the light is transmitted and reflects out of the medium, the Fresnel equations are used. It should be noted that the angle of the incident light needs to be taken into account. As S and P polarized light are parallel and perpendicular to the plane of incident, the Fresnel equations will be slightly different. Shown below are the Fresnel equations with subscript p and s referring to their polarization.

$$\mathrm{r_p} \equiv \frac{\mathrm{E_{rp}}}{\mathrm{E_{ip}}} = \frac{\mathrm{n_t}\cos\theta_\mathrm{i} - \mathrm{n_i}\cos\theta_\mathrm{t}}{\mathrm{n_t}\cos\theta_\mathrm{i} + \mathrm{n_i}\cos\theta_\mathrm{t}}$$

$$\mathrm{t_p} \equiv \frac{\mathrm{E_{tp}}}{\mathrm{E_{ip}}} = \frac{2\mathrm{n_i}\cos\theta_\mathrm{i}}{\mathrm{n_t}\cos\theta_\mathrm{i} + \mathrm{n_i}\cos\theta_\mathrm{t}}$$

$$\mathrm{r_s} \equiv \frac{\mathrm{E_{rs}}}{\mathrm{E_{is}}} = \frac{\mathrm{n_i}\cos\theta_\mathrm{i} - \mathrm{n_t}\cos\theta_\mathrm{t}}{\mathrm{n_i}\cos\theta_\mathrm{i} + \mathrm{n_t}\cos\theta_\mathrm{t}}$$

$$\mathrm{t_s} \equiv \frac{\mathrm{E_{ts}}}{\mathrm{E_{is}}} = \frac{2\mathrm{n_i}\cos\theta_\mathrm{i}}{\mathrm{n_i}\cos\theta_\mathrm{i} + \mathrm{n_t}\cos\theta_\mathrm{t}}$$

In a thin film, or film stack, there will be multiple reflections and refractions at each one of the interfaces. To determine the total reflected and transmitted light, each component of phase for light reflected and transmitted must be tracked. For this, another equation by Fresnel is used which is dependent upon thickness.

$$\beta = 2\pi\left(\frac{d_1}{\lambda}\right)n_1\cos(\theta_1)$$

A film stack and the resulting reflected and transmitted waves are shown in figure xx with the Fresnel equations. As can be seen the β term increases with each additional reflection and transmission through the film. As the number of reflections and refractions increase the intensity of the transmitted light decreases. This should make physical sense as at each interface the light beam is split, i.e. some reflected, some refracted. The overall amount of light reflected r_{012} is used to determine film properties (more on that later) and thickness. Thickness changes result in the value of β changing the amount of light that reaches the detector.

The representation of a light wave traveling through space in Cartesian coordinates is represented by the equation:

$$\varphi = A\sin(Kx - \omega t + \delta)$$

Where K is the propagation number (index of refraction), x is the wave at position x before propagation, ωt depicts the wave at time t, A is the amplitude of the initial wave and δ represents the initial phase before interaction with a media. As the index N is defined to be a complex number, the equation for a light wave should be defined as a complex number as well. The equation above defined in complex coordinates:

$$\varphi = A\exp[\mathrm{i}(\omega t - Kx + \delta)]$$

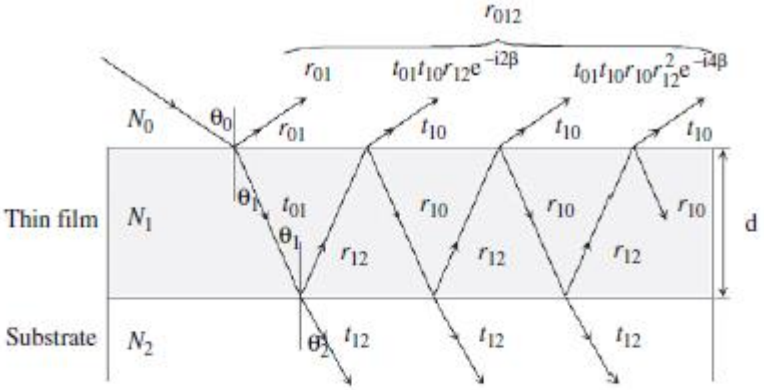

Figure 2-3. Cartoon showing the reflection and refraction of a single incident beam through a thin film and its infinite summation as r_{012}.[43]

2.1.3 Optical Properties of Films

The index of refraction (N) is a specific property of the material that the light wave is traveling through. The index of refraction dictates the frequency and speed of light in a media; therefore, it must be accounted for in the representation of a light wave traveling through any media. Interaction of light with media can be described the complex index of refraction

$$N \equiv n - ik$$

Where n is the is the index of refraction and k is the absorption coefficient.

In the simple case with no absorption, K is defined as 2πn/λ and the wave of light in the transparent media behaves as such:

$$E = E_{t0} \exp\left[\mathrm{i}\left(\omega t - \frac{2\pi n}{\lambda}x + \delta\right)\right]$$

In the second case where k is non-zero, light interaction in the media is represented as such:

$$E = E_{t0}\, exp\left(\frac{-2\pi k}{\lambda}\right) \exp\left[\mathrm{i}\left(\omega t - \frac{2\pi n}{\lambda}x + \delta\right)\right]$$

Addition of the absorption coefficient term shows that as light interacts with an absorbing medium, It loses its initial energy. Light propagation through media for both cases is shown in Figure 2-4 below

Both n and k are good representations of how light interacts with the films, however, there is better optical properties that correlate with the atoms themselves. This allows for a better understanding of the material, and how modeling is used to determine Ψ and Δ.

The optical constant that better describes atoms and their environment is the complex dielectric constant. This is a mathematical representation of how the electromagnetic wave interacts with the electrons and nucleus of an atom. As the light travels into the medium it's slowed by the transition of opposing electric dipoles created by electrons and nuclei. Essentially the dielectric constant is the ability for electric polarization to occur.

The complex dielectric constant is equal to the square of the complex index. Two terms define the dielectric constant

$$\varepsilon = \varepsilon_1 - i\varepsilon_2$$

Where

$$\varepsilon_1 = n^2 - k^2;\ \varepsilon_2 = 2nk$$

As can be seen from these relations, ε_1 is related to the index of refraction when k is zero and ε_2 is related to the absorption. A simple analogy to understand how ε_2 is related to absorption is this: dielectric polarization (or coulombic force between charged particles) is often describes as a spring, and when light with the appropriate frequency, it resonates with the spring, losing energy.

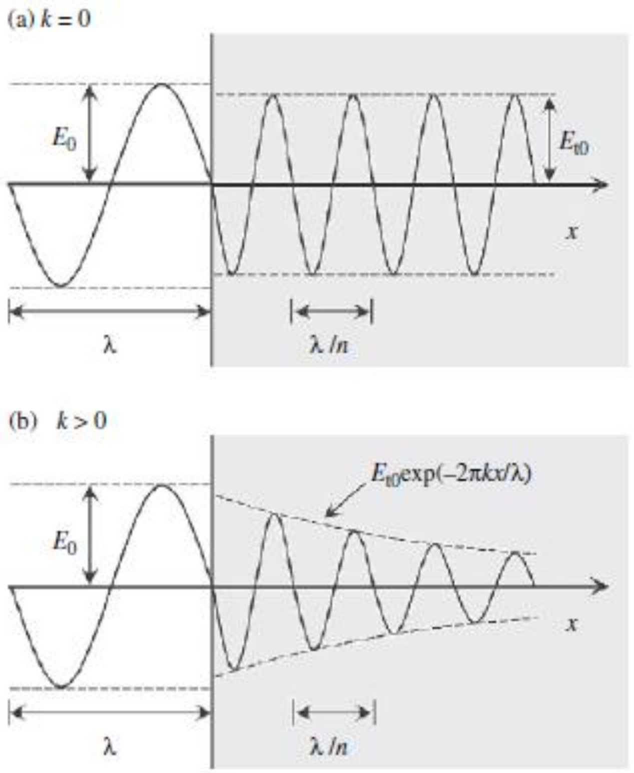

Figure 2-4. Propagation of electromagnetic waves through two different media. (a) a non-absorptive film (k=0), (b) an absorptive film (k>0).[43]

2.1.4 Ellipsometry Measurement

Ellipsometry measures the change in phase (angle) between of S and P polarized light (Δ) as well as the amplitude change between the two (Ψ). Application of the Fresnel equations to Ψ and Δ, can solve for n and k. Ellipsometry can be run in two modes: transmission, or reflection. Dependent upon the mode used, the values of psi and delta are equal to the ratio of P polarized light over S polarized light, whether it is reflectance or transmittance.

$$\rho \equiv \tan \Psi \exp(\mathrm{i}\Delta) \equiv \frac{r_p}{r_s}$$

The Fresnel equations defining reflectance is a ratio of the reflected E field divided by the incident field. Applying this, the equation above can be rewritten as

$$\tan \Psi \exp(\mathrm{i}\Delta) \equiv \frac{r_p}{r_s} \equiv \frac{E_{rp}/E_{ip}}{E_{rs}/E_{is}} = \frac{E_{rp}}{E_{rs}}$$

This equation proves that Δ is related to the phase difference between the reflected waves, and that tan(Ψ) is related to the amplitude (remember that E_{rp} is the equation for an electric field in space) . Thus the equation can be broken up into polar coordinates. Knowing that

$$r_k = |r_k| \exp(i\delta_{rk})$$

Where $|r_k|$ is the magnitude of S and P polarized light and δ_{rk} is the angle of S or P polarized light. Using this we arrive at

$$\tan \Psi = \frac{|r_p|}{|r_s|} \qquad \Delta = \delta_p - \delta_s$$

A physical representation of the transformation into polar coordinates is shown below in figure 2-5.

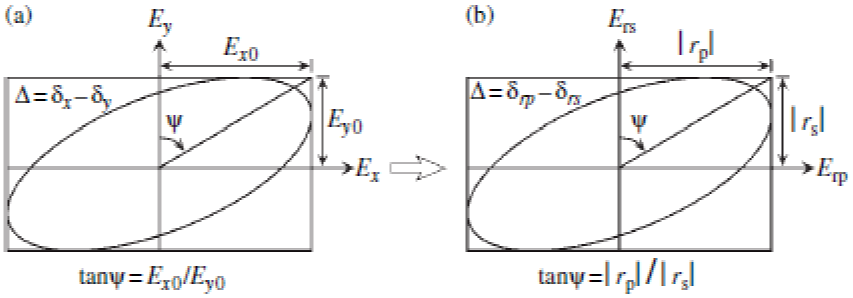

Figure 2-5. Transformation of the electromagnetic wave (E_i) from cartesian to polar coordinates.[43]

Figure 2-3 shows how an incident beam of light interacts with the thin film and substrate. The total amount of reflection r_{012} is the equivalent of r_p. The total reflected waves, have the summation of the infinite series

$$y = a + ax + ax^2 + ax^3 \cdots$$

Which can be reduced to y=a/(1-x) to

$$r_{012} = r_{01} + \frac{t_{10}t_{01}r_{12}\exp(-i2\beta)}{1 - r_{01}r_{12}\exp(-i2\beta)} = \frac{r_{01} + r_{12}\exp(-i2\beta)}{1 + r_{01}r_{12}\exp(-i2\beta)}$$

The last relation comes from r_{10}=-r_{01} and $t_{10}t_{01}$= 1-r_{01}^2 from the Fresnel equations. Everything together leads to the relation below, which is a film stack in ambient on an infinite substrate. The representation of r_p/r_s for a film stack with a thickness on an infinite substrate is given in the equation below:

$$\tan(\psi)\exp(i\Delta) = \frac{r_p}{r_s} = \left(\frac{r_{01,p} + r_{12,p}\exp(-i2\beta)}{1 + r_{01,p}r_{12,p}\exp(-i2\beta)} \middle/ \frac{r_{01,s} + r_{12,s}\exp(-i2\beta)}{1 + r_{01,p}r_{12,p}\exp(-i2\beta)} \right)$$

This equation is used to determine n and k from the values of psi and delta. The information needed is how many layers are in the film stack to correctly integrate the correct Fresnel equations into the computer software.

2.1.5 Modelling with Ellipsometry

After a measurement of a film is taken, it is important to translate the information of Psi and Detlta to ε_1 and ε_2 (or n and k). For this process to occur, a model is built to help describe the dielectric constants. A variety of models can be used if the film is absorptive, but mainly, the Lorentzian is used. For the case that it is transparent, a Cauchy or Sellmeier model is used.

Lorentz

The Lorentz model is a classical model of an electron connected to the nucleus by a spring (the bond). When light is illuminated, the electric field of light [$E=E_o\exp(i\omega t)$] will induce oscillations in the X direction. A physical representation for a Lorentz is shown in figure 2-6. The equation of motion for an electron fixed to a non moving nucleus is

$$m_e\frac{d^2x}{dt^2} = -m_e\Gamma\frac{dx}{dt} - m_e\omega_0^2x - eE_0\exp(i\omega t)$$

where Γ is the damping coefficient, the second term is electron movement when connected to a spring, and the last term is the electrostatic force of an electron in an oscillating electric field. Now if it's assumed that the electron is moving at time t, we can express this as $x(t)=a\exp(i\omega t)$. As there are many electrons, we can then state the polarization as $P= -eN_e a\exp(i\omega t)$. Also, we can use ω as the photon energy E_n. Using these equations we arrive at the dielectric function of the Lorentz model

$$\varepsilon = 1 + \sum_j \frac{A_j En_{0j}}{En_{0j}^2 - En^2 + i\Gamma_j En}$$

This model is useful for crystalline absorptive materials.

Modelling with the program CompleteEase, the Lorentzian is defined as:

$$\varepsilon_{lorentz} = \frac{Amp_n Br_n E_n}{En_n^2 - E^2 - iEBr_n}$$

n denotes oscillator number, Amp is the amplitude of ε_2 at its highest point, Br is the full width at half-max, E is the electric field energy, and E_n is the energy position of the lorentzian.

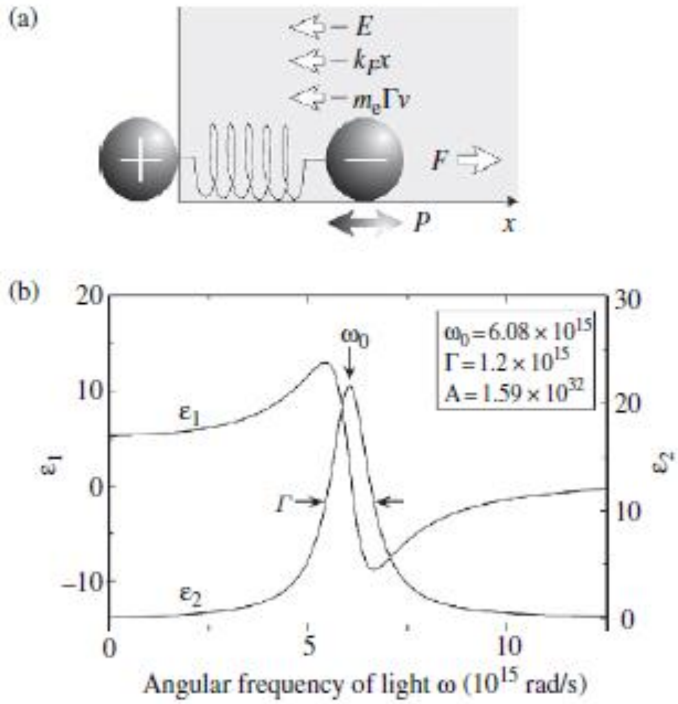

Figure 2-6. (a) Physical representation of the Lorentz model and (b) calculation of the dielectric constants vs angular frequency from the Lorentz Model.[43]

Cauchy

If the material is a dielectric, then $\varepsilon_2=0$ or approximately zero. For this model, we use the lorentzian model and assume that Γ is zero. The Sellmeier model can then be expressed by

$$\varepsilon = n^2 = A + \sum_j \frac{B_j \lambda^2}{\lambda^2 - \lambda_{0j}^2}$$

where A and B_j represent fitting parameters and λ_0 is ω_o. In the case of the Cauchy model, it is a taylor expansion of the Sellmeier model where

$$n = A + \frac{B}{\lambda^2} + \frac{C}{\lambda^4} + \cdots$$

The parameters A, B, C are the same parameters fit with the CompleteEase software

2.2 X-Ray Photoelectron Spectroscopy

2.2.1 Photoemission Process

X-ray photelectron spectroscopy (XPS) is a technique used to investigate the chemical composition and chemical environment of materials. XPS uses the principle of photoemission on core electrons to determine the chemical environment of materials. Figure 2-7 shows the basic principle of photoemission. A monochromatic photon with large kinetic energy penetrates the core orbitals of the atoms and excites the core electron. During this process, the electron is ejected from the core, through the valence band, Fermi level and into vacuum where it can be analyzed.

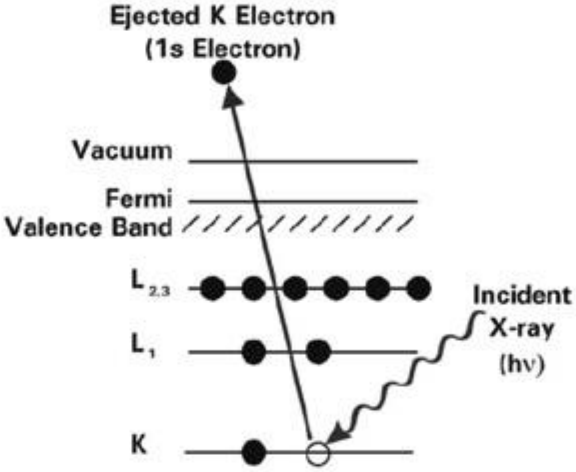

Figure 2-7. Photoemission process: incident x-ray causes core electron ejection.[44]

The analyzed constant is the kinetic energy of the ejected electron. The kinetic energy can be related to the binding energy by the equation:

$$E_k = E_{h\upsilon} - E_{\varphi} - E_B$$

$E_{h\upsilon}$ is known as it's the photelectron energy, E_k is the analyzed kinetic energy, E_{φ} is the correlation factor for solid effects during ejection (i.e. work function). The remaining unknown is the binding energy of the analyzed electron. This gives information on the orbital the electron was ejected from and its chemical environment.

2.2.2 Chemical Environment

Binding energy for all electrons in atoms shift to higher or lower binding energies depending on the chemical environment. For materials that are oxidized, the binding energy of the orbitals will be shifted higher. A simple illustration is to think of the oxidized molecule as a cation. The extra nuclear charge will cause a contraction of the core electrons and increase of the coulombic force between the electron and the nucleus. The greater coulombic interaction needs more energy to remove the core electron (i.e. the core electrons binding energy is higher). The converse is the opposite. A higher reduction state of an atom correlates to an expansion and less coulombic force between the nucleus and core electron. XPS' ability to differentiate oxidation states of the atoms in their chemical environment is a strength of this technique.

2.2.3 XPS Apparatus and X-Ray Generation

A schematic of an XPS apparatus is shown in the figure below. X-rays are generated by shooting an electron beam into a metal target. As the electrons interact with the electric field of the atomic nucleus, they lose energy giving off high energy photons. This type of radiation is called Bremsstrahlung radiation. The generated X-rays are not all the same wavelength and must be for analysis. The X-ray photons are put through a material, typically quartz, that makes them monochromatic. The X-rays are then introduced to the sample ejecting core electrons. The ejected core electrons are then put through a retarding field that will reduce their energy, and then into an energy analyzer. Electrons of too high an energy will crash into the walls of the circular energy analyzer. Electrons that make it to the MCD have a specific kinetic energy and, generate a current which is analyzed by a detector. The retarding field varies the KE of the electrons into the electron analyzer. This allows for analysis of a spectrum of different kinetic energies

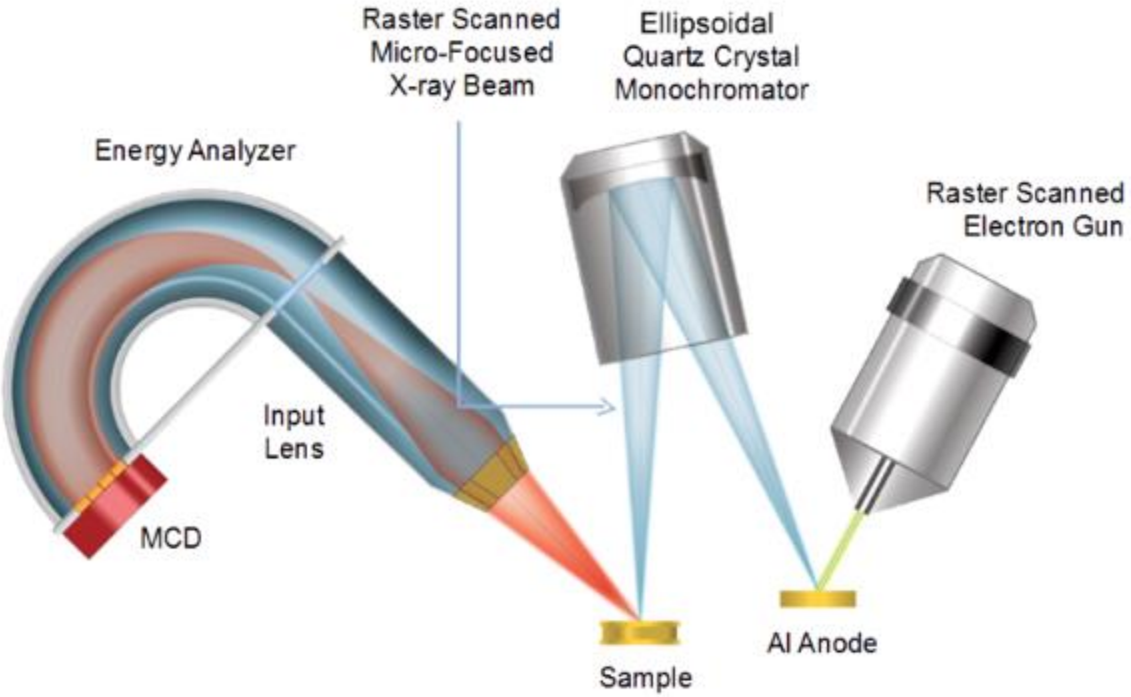

Figure 2-8. Apparatus of an XPS machine.[45]

CHAPTER 3

Thermal Atomic Layer Etching of Crystalline Aluminum Nitride Using Sequential, Self-Limiting HF and Sn(acac)$_2$ Reactions and Enhancements by H_2 and Ar Plasmas

3.1 Introduction

Atomic layer etching (ALE) is a sequential, self-limiting thin film removal technique that can etch materials precisely with Ångstrom-level precision. ALE is needed for future semiconductor manufacturing processes.[46] Until recently, most ALE processes have been conducted using halogen or halocarbon adsorption followed by energetic ion or atom bombardment to remove material.[47-48] This approach has been demonstrated for a variety of materials including Si,[49] Ge,[50] GaAs,[51] SiO_2,[52] HfO_2,[53] and graphene.[54] Etching with energetic ion or atom bombardment produces anisotropic material removal, but can also damage the underlying substrate.[53]

Recently, new ALE methods have been developed based on sequential, self-limiting thermal reactions.[55] Thermal ALE has been demonstrated for Al_2O_3 ALE and HfO_2 ALE using hydrogen fluoride (HF) and tin(II) acetylacetonate (Sn(acac)$_2$) as the reactants.[37, 56-57] Al_2O_3 ALE has also been performed using HF and trimethylaluminum (TMA) as the reactants.[58] During the thermal ALE reactions, HF fluorinates the metal oxide and forms a metal fluoride layer on the surface.[55] The metal precursors, Sn(acac)$_2$ and TMA, then accept fluorine from the metal fluoride and transfer their ligands to the metal fluoride in a ligand-exchange reaction.[55] This transmetalation[59] or redistribution[60] process can form volatile species such as AlF(acac)$_2$ or Al(acac)$_3$.

The fluorination and ligand-exchange reactions have etched amorphous metal oxides such as Al_2O_3 and HfO_2 films that were grown using atomic layer deposition (ALD).[37, 56-57] A related study also described the thermal ALE of amorphous AlF_3 films.[61] In contrast, there have been no reports for the thermal ALE of crystalline material. There also have been no previous demonstrations of the thermal ALE of a metal nitride, such as AlN, or any III-V semiconductor. However, the continuous dry etching of crystalline III-V metal nitrides, such as AlN, has been previously documented using different halogen plasma sources.[62-64] To extend the development of atomic layer processing methods, this letter presents the thermal ALE of crystalline AlN films using sequential, self-limiting exposures of HF and $Sn(acac)_2$ and the enhancement of the etching rates using plasma exposures. AlN ALE should be useful for the processing of AlN in high power and high temperature transistors, MEMS acoustic resonators and photonic devices.[62-64]

3.2 Experimental

3.2.1 AlN Films

AlN samples were grown epitaxially on Si(111) wafers by Kyma Technologies using their plasma vapor deposition of nanocolumns (PVDNC™) crystal growth process. The AlN films are in the wurtzite crystalline phase with the (0001) plane parallel to the surface. The initial AlN films had a thickness of ~500 Å. Etching of the AlN films was analyzed using *in situ* spectroscopic ellipsometry (SE) in a reaction chamber that has been described elsewhere.[65-66] This reaction chamber is very similar to plasma atomic layer deposition (ALD) reactors equipped for *in situ* ellipsometry measurements.[67] The chamber was pumped by a rotary vane pump (Alcatel 2010). The chamber was also equipped with a capacitance manometer for pressure measurements and a differentially-pumped mass spectrometer for gas analysis. The base pressure of the reaction chamber was ~10 mTorr.

3.2.2 Reaction Conditions

The AlN films on the Si(111) wafers had dimensions of 1.5 cm x 1.5 cm. These samples were placed on a heated sample stage inside the reaction chamber. The temperature of the samples was held constant at 275°C for all of the experiments. The walls of the chamber were held at ~170°C. Sn(acac)$_2$ (99.9%, Sigma-Aldrich) and HF-pyridine (70 wt% HF, Sigma-Aldrich) were used as the reactants.[37, 56-57] Each reactant was separately dosed into the chamber and held statically for 10 seconds. After each reactant exposure, the reaction chamber was purged with 80 sccm of ultrahigh purity (UHP) N_2 gas at a pressure of 840 mTorr for 130 seconds

3.2.3 Spectroscopic Ellipsometry

AlN films were analyzed with in situ SE to allow analysis after each full AB cycle or A/B half cycle. AlN samples were analyzed with a Sellmeier model with Complete Ease software. Due to the high bandgaps of AlN (6.15eV) it behaves as a dielectric in the SE spectral range and can be modeled as such in our spectral range (0.73-5.18eV). This allows for accurate thickness measurements without a complex model accounting for light absorption.

3.2.4 X-Ray Photoelectron Spectroscopy

X-ray photoemission spectroscopy (XPS) analysis was performed using a PHI 5600 X-ray photoelectron spectrometer using a monochromatic Al Kα source. The XPS depth-profiling was obtained using Ar ion sputtering. The XPS data were collected using Auger Scan (RBD Instruments) and analyzed in CASA XPS (Casa Software Ltd.). The x-ray reflectivity (XRR) scans were recorded by a high resolution x-ray diffractometer (Bede D1, Jordan Valley Semiconductors) using Cu Kα (λ = 1.540 Å) radiation. The analysis software (Bede REFS, Jordan Valley Semiconductors) fitted the XRR scans to determine film thicknesses.

3.2.5 Inductively Coupled Plasma

The reactor was equipped with a remote inductively coupled plasma (ICP) source. The ICP plasma source was positioned with the opening roughly 3-4 cm above a heated sample stage. The ICP source was a quartz tube (6 cm inner diameter x 25 cm long) surrounded by a copper helical coil. The ICP was generated using a 13.56 MHz RF generator (Paramount RF Power Supply, Advanced Energy) and 50 ohm impedance matching network (Navigator Digital Matching Network, Advanced Energy).

3.3 Results & Discussion

3.3.1 Thermal ALE

3.3.1.1 ALN ALE Under Self-Limiting Conditions

Figure 3-1 shows the etching of a typical AlN sample for 600 reaction cycles at 275°C under self-limiting reaction conditions with an HF exposure of 1270 mTorr·s and a $Sn(acac)_2$ exposure of 900 mTorr·s. The slow etch rate over the first 300 reaction cycles is attributed to an AlO_xN_y layer on the surface of the AlN film. The etch rate in this AlO_xN_y region is ~0.07 Å/cycle. After a thickness change of ~30 Å corresponding with ~300 ALE reaction cycles, there is an increase in the etch rate. This increase is attributed to reaching a purer AlN film with less oxidation. After a thickness change of ~50 Å corresponding with ~400 ALE reaction cycles, the etch rate increases to ~0.36 Å/cycle in the pure AlN region.

3.3.1.2 Film Composition Determination by XPS

To confirm the presence of an AlO_xN_y layer on the AlN film, the film composition was evaluated using x-ray photoelectron spectroscopy (XPS). Figure 2 displays the results of an XPS depth-profile experiment versus sputtering time. Figure 2 indicates that there is a large concentration of oxygen on the surface that decays as a function of sputtering time. The oxygen concentration in the bulk of the AlN film is only ~1.5-2.0 at%. Using the sputtering time and the Si XPS signal as a marker for the removal of the entire AlN film with an initial thickness of ~500 Å, the thickness of the AlO_xN_y layer is estimated to be ~40 Å. This AlO_xN_y layer thickness agrees with the etching results in Figure 1. The thickness of the AlO_xN_y layer is also consistent with x-ray reflectivity (XRR) experiments that yield an oxide thickness of ~44 Å on the AlN film. The AlO_xN_y layer thickness is slightly higher than the typical oxide thicknesses of ~20-30 Å reported on AlN samples exposed to ambient air at room temperature.[68-69] Figure 2 also observes that the AlN films are Al-rich in agreement with previous XPS characterization by Kyma Technologies. Similar Al-rich AlN films are reported by XPS depth-profiling studies of AlN films grown using various techniques.[70-72]

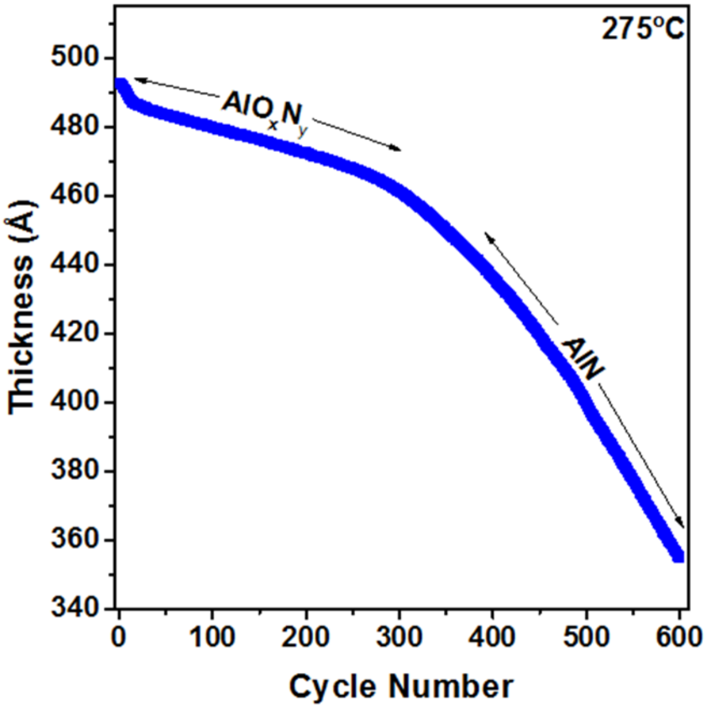

Figure 3-1. Film thickness measured by spectroscopic ellipsometry vs number of AlN ALE reaction cycles at 275 ºC. The etch rate increases after removing the AlOxNy layer on the AlN film.

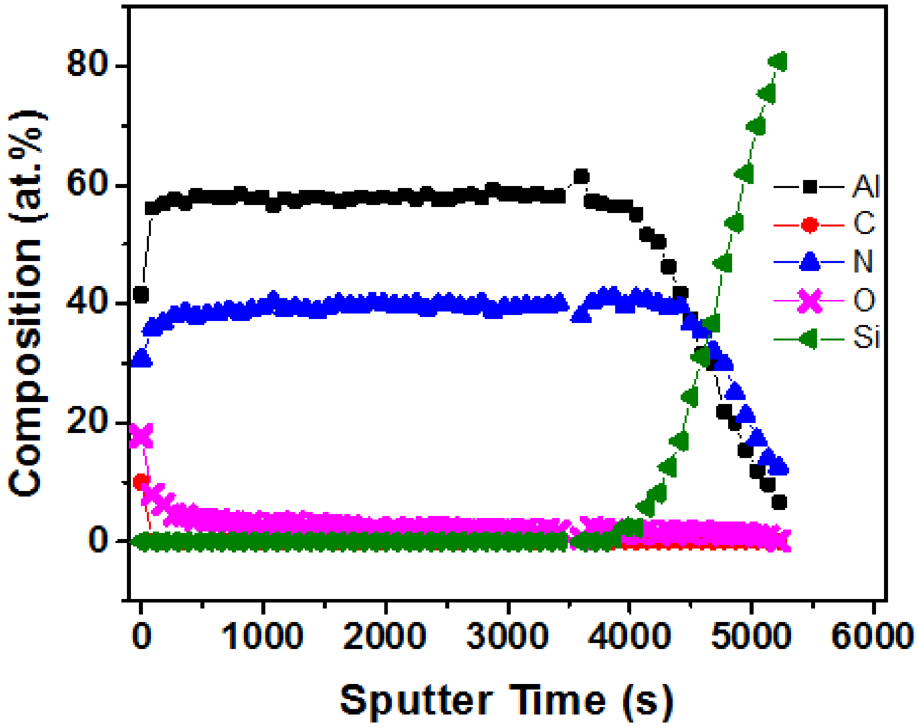

Figure 3-2. Film composition vs sputter time obtained by XPS depth-profiling analysis. The initial AlN film on the Si(111) wafer had a thickness of ~500 Å.

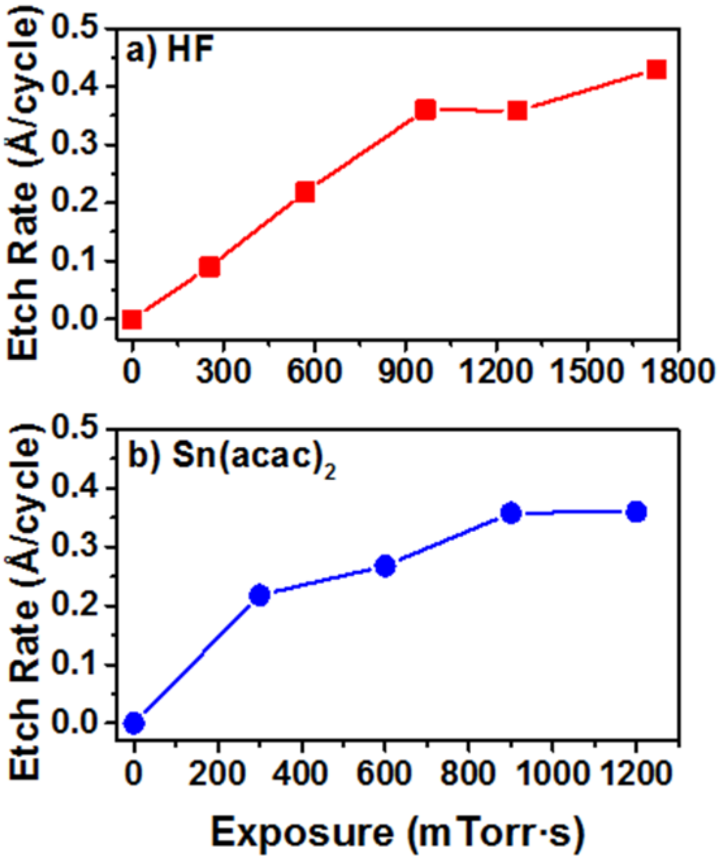

Figure 3-3. Etch rate vs reactant exposure during AlN ALE at 275 °C. (a) Etch rate vs HF exposure with Sn(acac)2 exposure fixed at 900 mTorrs and (b) etch rate vs Sn(acac)2 exposure with HF exposure fixed at 1270 mTorrs.

3.3.1.3 Self-Limiting Experiments

Figure 3 investigates the self-limiting nature of the HF and $Sn(acac)_2$ reactions during the AlN ALE reactions at 275°C. Etch rates were determined by varying one reactant exposure while keeping the other reactant exposure constant. Figure 3a depicts the self-limiting behavior of the HF reaction with a $Sn(acac)_2$ exposure of 900 mTorr·s defined by a $Sn(acac)_2$ exposure time of 10 s and a $Sn(acac)_2$ pressure of 90 mTorr. The HF exposures were changed from 254 to 1730 mTorr·s using an HF exposure time of 10 s and different HF pressures. The reaction chamber was purged with 80 sccm of UHP N_2 gas at a pressure of 840 mTorr for 130 seconds after each reactant exposure.

Figure 3a shows that small etch rates were observed for low HF exposures when the surface has not yet formed a saturated fluoride layer thickness. After an exposure of 966 mTorr·s, the fluorination by HF has reached self-limiting conditions and the etch rate is ~0.36 Å/cycle. The slight increase of the etch rate at an HF exposure of 1730 mTorr·s is likely caused by chemical vapor etching (CVE). HF has a long residence time in the reaction chamber and purge times over 10 minutes are needed to remove HF completely from the reactor after large HF exposures.

Figure 3b demonstrates the self-limiting nature of the $Sn(acac)_2$ reaction. $Sn(acac)_2$ exposures were varied while HF exposures were held constant at an exposure of 1270 mTorr·s defined by a HF exposure time of 10 s and a HF pressure that varied between 140-110 mTorr. The $Sn(acac)_2$ exposures were varied from 300 to 1200 mTorr·s using an exposure time of 10 s and different $Sn(acac)_2$ pressures. The etch rate slowly increases with $Sn(acac)_2$ exposure until reaching an etch rate of ~0.36 Å/cycle at an $Sn(acac)_2$ exposure of 900 mTorr·s. At this point, the $Sn(acac)_2$ reaction is self-limiting. Both Figure 3a and 3b show self-limiting behavior with an AlN etch rate of ~0.36 Å/cycle.

3.3.1.4 AlN ALE at 275 ºC

Figure 4 shows an expansion of a section of Figure 1 for 21 AlN ALE reaction cycles corresponding to reaction cycles #471-491 under self-limiting reaction conditions. The change in AlN thickness versus number of ALE reaction cycles is linear. The measured etch rate of 0.38 Å/cycle is consistent with the etch rate of ~0.36 Å/cycle determined by the self-limiting studies displayed in Figure 3. Numerous experiments were performed for AlN ALE at 275°C. The measured etch rates varied from 0.34 Å/cycle to 0.38 Å/cycle and the majority of the individual measurements yielded an etch rate of 0.36 Å/cycle.

3.3.1.5 AlN ALE Mechanism Proposal

Figure 3 investigates the self-limiting nature of the HF and $Sn(acac)_2$ reactions during the AlN ALE reactions at 275°C. Etch rates were determined by varying one reactant exposure while keeping the other reactant exposure constant. Figure 3a depicts the self-limiting behavior of the HF reaction with a $Sn(acac)_2$ exposure of 900 mTorr·s defined by a $Sn(acac)_2$ exposure time of 10 s and a $Sn(acac)_2$ pressure of 90 mTorr. The HF exposures were changed from 254 to 1730 mTorr·s using an HF exposure time of 10 s and different HF pressures. The reaction chamber was purged with 80 sccm of UHP N_2 gas at a pressure of 840 mTorr for 130 seconds after each reactant exposure.

Figure 3a shows that small etch rates were observed for low HF exposures when the surface has not yet formed a saturated fluoride layer thickness. After an exposure of 966 mTorr·s, the fluorination by HF has reached self-limiting conditions and the etch rate is ~0.36 Å/cycle. The slight increase of the etch rate at an HF exposure of 1730 mTorr·s is likely caused by chemical vapor etching (CVE). HF has a long residence time in the reaction chamber and purge times over 10 minutes are needed to remove HF completely from the reactor after large HF exposures.

Figure 3b demonstrates the self-limiting nature of the Sn(acac)$_2$ reaction. Sn(acac)$_2$ exposures were varied while HF exposures were held constant at an exposure of 1270 mTorr·s defined by a HF exposure time of 10 s and a HF pressure that varied between 140-110 mTorr. The Sn(acac)$_2$ exposures were varied from 300 to 1200 mTorr·s using an exposure time of 10 s and different Sn(acac)$_2$ pressures. The etch rate slowly increases with Sn(acac)$_2$ exposure until reaching an etch rate of ~0.36 Å/cycle at an Sn(acac)$_2$ exposure of 900 mTorr·s. At this point, the Sn(acac)$_2$ reaction is self-limiting. Both Figure 3a and 3b show self-limiting behavior with an AlN etch rate of ~0.36 Å/cycle.

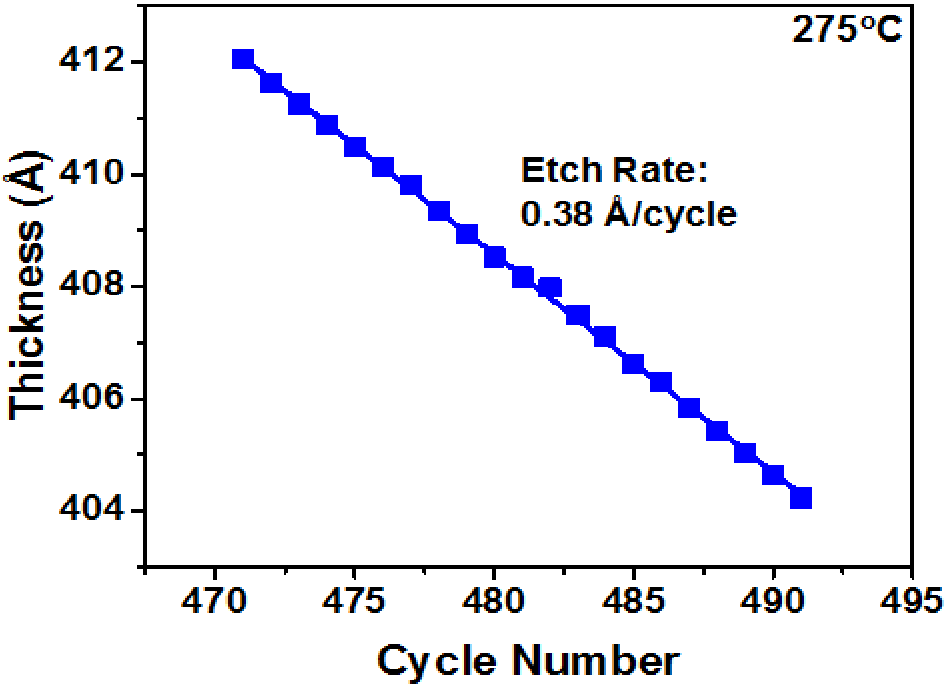

Figure 3-4. Film thickness vs number of AlN ALE reaction cycles at 275 °C in pure AlN region of AlN film. Change of thickness vs number of AlN ALE reaction cycles gives an etch rate of 0.38Å/cycle.

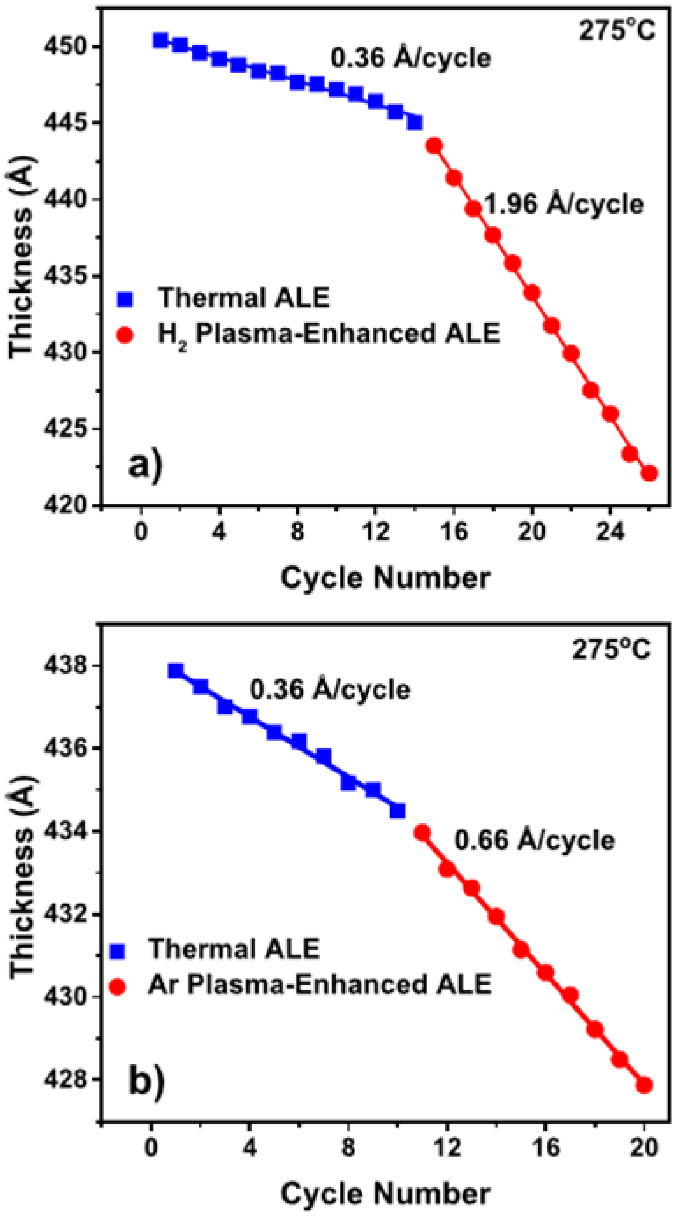

Figure 3-5. Film thickness vs number of AlN ALE reaction cycles at 275 °C in pure AlN region of AlN film showing results for thermal AlN ALE and plasma-enhanced ALE. (a) H2 plasma increases AlN etch rate from 0.36 to 1.96A Å/cycle. (b) Ar plasma increases AlN etch rate from 0.36 to 0.66 Å/cycle.

3.3.2 Plasma-Enhanced Thermal ALE of AlN

3.3.2.1 H_2 Plasma

The effect of H_2 plasma exposure on thermal AlN ALE was also examined using *in situ* SE analysis. Plasma exposures are known to enhance ALD and similar plasma effects may be beneficial during thermal ALE.[73] During the H_2 plasma experiments, the reactant exposures and purge times were the same as the reactant exposures and purge times used for thermal ALE. The H_2 plasma exposure was added after each $Sn(acac)_2$ exposure. The H_2 plasma with a power of 100 W was generated at a H_2 pressure of 40 mTorr and exposed to the surface for 15 seconds. After the H_2 plasma exposure, the chamber was purged for 60 seconds with the same conditions as used for the HF and $Sn(acac)_2$ reactants.

Figure 5a shows the effect of adding the H_2 plasma exposure after the $Sn(acac)_2$ exposure during each thermal ALE reaction cycle. These thickness measurements were performed in the pure AlN region of the AlN film. The etch rate increases from 0.36 Å/cycle for thermal ALE to 1.96 Å/cycle for H_2 plasma-enhanced thermal ALE. This large increase in the etch rate is attributed to the removal of acac surface species by H radicals from the H_2 plasma. Earlier experiments have shown that acac surface species may block surface sites and limit the etching during thermal Al_2O_3 ALE with HF and $Sn(acac)_2$ as the reactants.[37] Removal of these blocking species may allow for more HF to fluorinate the surface and, subsequently, for more ligand-exchange with $Sn(acac)_2$. Additionally, heat released by recombination of H radicals may facilitate desorption of the acac surface species.[74] The H_2 plasma by itself did not etch the AlN film unless the H_2 plasma was used in conjunction with the thermal ALE reaction cycles.

3.3.2.2 Argon Plasma

Recent studies have explored the effect of plasmas on ALD processing.[73, 75] Plasmas are believed to enhance ALD reactions primarily through reactive radical species. However, ions and radiation produced by plasmas can also influence surface reactions.[75] The enhancement of the etch rate for AlN ALE by the Ar plasma indicates that ions or radiation may be playing a role. The ions from ICP sources typically have energies <50 eV and could desorb the acac surface species that may limit the etching.[73, 75] Ar plasmas also have a variety of optical emission lines at wavelengths <200 nm that have photon energies larger than the AlN bandgap at ~6.2 eV.[76] These photons may be able to photodesorb acac surface species or excite electron/hole pairs by bandgap excitation that may lead to desorption. Optical emission from the H_2 plasma may also be adding to the effect of H radicals on thermal AlN ALE.[73]

The plasma enhancement effects on thermal ALE are very promising. Thermal ALE will be valuable for etching three-dimensional nanostructures, such as semiconductor nanowires, because thermal ALE is expected to be isotropic and conformal.[46] The plasma enhancement effects on thermal ALE from ions can facilitate anisotropic etching that will be useful for fabricating high aspect ratio nanodevices.[55] In addition, the plasma enhancement of thermal ALE will also lower the required processing temperatures for semiconductor nanofabrication.

3.3.2.3 Explanation of Plasma Enhancement

l Recent studies have explored the effect of plasmas on ALD processing.[73, 75] Plasmas are believed to enhance ALD reactions primarily through reactive radical species. However,

ions and radiation produced by plasmas can also influence surface reactions.[75] The enhancement of the etch rate for AlN ALE by the Ar plasma indicates that ions or radiation may be playing a role. The ions from ICP sources typically have energies <50 eV and could desorb the acac surface species that may limit the etching.[73, 75] Ar plasmas also have a variety of optical emission lines at wavelengths <200 nm that have photon energies larger than the AlN bandgap at ~6.2 eV.[76] These photons may be able to photodesorb acac surface species or excite electron/hole pairs by bandgap excitation that may lead to desorption. Optical emission from the H_2 plasma may also be adding to the effect of H radicals on thermal AlN ALE.[73]

The plasma enhancement effects on thermal ALE are very promising. Thermal ALE will be valuable for etching three-dimensional nanostructures, such as semiconductor nanowires, because thermal ALE is expected to be isotropic and conformal.[46] The plasma enhancement effects on thermal ALE from ions can facilitate anisotropic etching that will be useful for fabricating high aspect ratio nanodevices.[55] In addition, the plasma enhancement of thermal ALE will also lower the required processing temperatures for semiconductor nanofabrication.

3.4 Conclusion

The thermal ALE of crystalline AlN was performed using sequential, self-limiting HF and $Sn(acac)_2$ reactions. This is the first demonstration of the thermal ALE of a metal nitride and the first report of the thermal ALE of a crystalline III-V material. At self-limiting reaction conditions, the etch rate for AlN ALE was 0.36 Å/cycle at 275°C. These results suggest that other similar crystalline III-V metal nitrides, such as GaN and InN, should also be etched using HF and $Sn(acac)_2$. H_2 or Ar plasma exposures increased the AlN etch rate to 1.96 Å/cycle or

0.66 Å/cycle, respectively, at 275°C. The plasma enhancement of thermal ALE should be useful for introducing anisotropic etching and also for lowering the temperatures required for etching. Thermal ALE and plasma-enhanced thermal ALE have great promise for etching a number of important materials and expanding the tool set for advanced semiconductor manufacturing.

3.5 Acknowledgements

This work was supported by the Defense Advanced Research Projects Agency (DARPA) under Grant W911NF-13-1-0041. The authors thank Tyler McQuade from DARPA for his support and encouragement.

Chapter 4

WO_3 and W Thermal Atomic Layer Etching Using "Conversion-Fluorination" and "Oxidation-Conversion-Fluorination" Mechanisms

4.1 Introduction

The continued miniaturization of advanced semiconductor devices requires atomic layer control in both growth and etching processes.[46] Atomic layer deposition (ALD) and atomic layer etching (ALE) techniques can provide the necessary atomic level precision.[77] ALD techniques have been developed for a wide range of materials over the past few decades and have been extensively adapted by the semiconductor industry.[78-79] In contrast, the need for ALE techniques has emerged more recently and ALE methods are still in an early stage of development.[48]

Initial plasma ALE methods have been based on surface activation by halogenation followed by ion bombardment to remove surface material.[48] Plasma processes have been developed for a variety of materials including Si,[49, 80] compound semiconductors,[51, 81] metal oxides[52-53, 82] and carbon materials.[83-84] The plasma ALE method can achieve anisotropic etching. Thermal ALE techniques have also been demonstrated with fluorination and ligand-exchange reactions.[55] Thermal ALE methods have been developed for Al_2O_3,[56, 58, 85-86] HfO_2,[57] ZrO_2,[87] AlN,[88] and AlF_3.[61] Thermal ALE is able to provide isotropic etching.

Materials with volatile metal fluorides do not have thermal ALE pathways using fluorination and ligand-exchange reactions because their fluorides are gases. Other materials, such as elemental metals, may fluorinate readily and produce fluoride layers too thick for ALE. For these materials, alternative pathways are required for controlled atomic layer etching.

Some new strategies in thermal ALE have recently been introduced based on “conversion-etch” mechanisms.[89-90] In the conversion-etch procedure, the surface layer is converted to a different material that can be fluorinated and removed by ligand-exchange. Conversion-etch approaches also have the potential to provide pathways for the ALE of materials with volatile fluorides.

In this paper, “conversion-fluorination” and “oxidation-conversion-fluorination” mechanisms are demonstrated for thermal ALE. The conversion reactions utilize BCl_3 as the reactant. BCl_3 has the ability to convert many metal oxides to B_2O_3. B_2O_3 has a volatile fluoride and can be easily removed spontaneously as BF_3 and H_2O by HF exposures. The example of “conversion-fluorination” is WO_3 ALE using BCl_3 and HF as the reactants in an AB sequence. The example of “oxidation-conversion-fluorination” is W ALE using O_3, BCl_3 and HF in an ABC sequence.

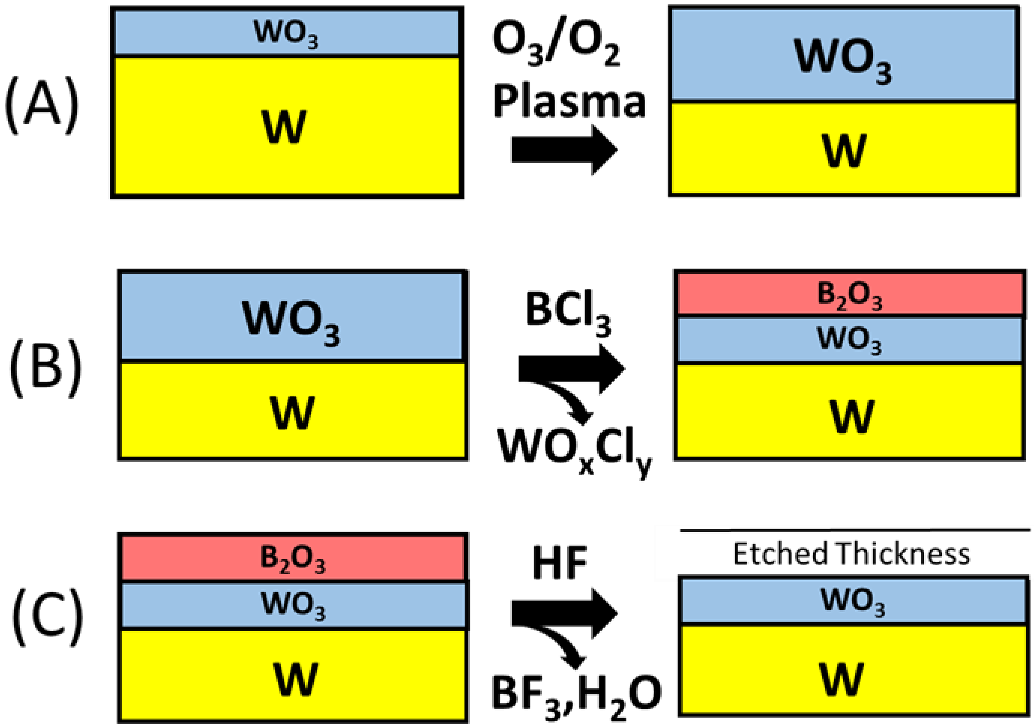

Figure 4-1. Oxidation, conversion, and fluorination reactions: (A) oxidation of W using O_2/O_3; (B) conversion of W to WO_3 using BCl_3; and (C) fluorination of B_2O_3 by HF to form volatile BF_2 and H_2O.

Figure 1 shows the various reaction steps for W and WO_3 ALE. In reaction A, W is oxidized to WO_3 using ozone (O_2/O_3). In reaction B, BCl_3 is used to convert the surface of WO_3 to a B_2O_3 surface layer. During this conversion, the chlorine ligands are transferred from BCl_3 to the surface to form volatile WO_xCl_y products. In reaction C, the B_2O_3 surface layer can then be etched spontaneously by HF to form H_2O and BF_3 products. The conversion of WO_3 to B_2O_3 is necessary because HF cannot spontaneously etch WO_3.

Reactions A, B and C in Figure 1 based on oxidation, conversion and fluorination are all thermochemically favorable.[91] The reaction and standard free energy changes for the oxidation of W to WO_3 using O_3 or O_2 are:

$W + O_3(g) \rightarrow WO_3 + O_2(g)$ $\Delta G°(200°C) = -296.7$ kcal/mol (1)

$W + 3/2O_2(g) \rightarrow WO_3$ $\Delta G°(200°C) = -171.7$ kcal/mol (2)

Proposed conversion reactions of WO_3 with BCl_3 to yield various possible WO_xCl_y reaction products and their standard free energy changes are:

$WO_3 + 2BCl_3(g) \rightarrow B_2O_3 + WCl_6(g)$ $\Delta G°(200°C) = -7.7$ kcal/mol (3)

$WO_3 + 4/3BCl_3(g) \rightarrow 2/3B_2O_3 + WOCl_4(g)$ $\Delta G°(200°C) = -4.3$ kcal/mol (4)

$WO_3 + 2/3BCl_3(g) \rightarrow 1/3B_2O_3 + WO_2Cl_2(g)$ $\Delta G°(200°C) = -7.8$ kcal/mol (5)

In addition, the reaction for the fluorination of B_2O_3 to volatile BF_3 and H_2O reaction products and the standard free energy change is:

$B_2O_3 + 6HF(g) \rightarrow 2BF_3(g) + 3H_2O(g)$ $\Delta G°(200°C) = -17.3$ kcal/mol (6)

After removal of the B_2O_3 surface layer, a new W or WO_3 surface remains. The reactions can then be repeated to etch either W or WO_3. W ALE uses reactions A, B and C. WO_3 ALE uses reactions B and C.

HF alone should not etch or react with the WO_3 or W surface. Likewise, BCl_3 should not react with the W surface. The expectations for these reactions are based on their positive standard free energy changes:

$$WO_3 + 6HF(g) \rightarrow WF_6 + 3H_2O\ (g) \qquad \Delta G°(200°C) = +32.6\ \text{kcal/mol} \qquad (7)$$

$$W + 6HF(g) \rightarrow WF_6(g) + 3H_2(g) \qquad \Delta G°(200°C) = +19.0\ \text{kcal/mol} \qquad (8)$$

$$W + 2BCl_3(g) \rightarrow 2B + WCl_6(g) \qquad \Delta G°(200°C) = +95.0\ \text{kcal/mol} \qquad (9)$$

W and WO_3 can also be etched spontaneously using various dry etching techniques. Methods for spontaneous tungsten etching utilize plasmas containing various halogens such as fluorine[92-94] or chlorine.[93, 95-96] Tungsten etching occurs through formation of volatile chlorides or fluorides. Tungsten can also be etched by Cl_2 or XeF_2 gases.[95, 97-98] WO_3 can be etched spontaneously with halogen-containing plasmas using NF_3 or SF_6.[99-101] WF_6 is also known to etch WO_3 spontaneously at >180°C from WO_3 ALD studies using WF_6 and H_2O as the reactants.[102-103] This spontaneous etching of WO_3 by WF_6 suggests a pathway for W ALE based on sequential reactions with W oxidation followed by WF_6 exposures to remove WO_3.

W ALE and WO_3 ALE may have applications in a variety of areas. In the semiconductor industry, W is employed as a conductor in contact holes and vias.[104] W is also utilized for fabricating gates in 3D NAND memory devices.[105] Outside the semiconductor industry, W has application in MEMS and NEMS structures.[106-107] WO_3 also is a useful material for water splitting[108] and gas sensing.[109] The atomic layer controlled etching of W and

WO_3 may be needed for device fabrication. The isotropic etching of W may be particularly useful for the lateral etching required to fabricate W gates in 3D NAND flash memory.[105]

4.2 Experimental

4.2.1 W Films

W samples were deposited on Si wafers with a 500 nm thermal oxide layer. The SiO_2 layer improves the sensitivity of the *in situ* spectroscopic ellipsometry (SE) analysis by providing interference enhancement.[110] Al_2O_3 ALD films were first grown on the SiO_2 thermal oxide layer at 130°C using 15 Al_2O_3 ALD cycles. These Al_2O_3 ALD films provided an adhesion layer for W ALD growth.[111] W ALD films with a thickness of 250 Å were then deposited at 130°C with sequential self-limiting reactions of WF_6 and Si_2H_6.[112] These Al_2O_3 ALD and W ALD films were deposited in a separate hot-wall viscous flow reactor. Upon exposure to atmosphere, an oxide thickness of 12-30 Å is formed on the W film as determined by x-ray photoelectron spectroscopy (XPS) and x-ray reflectivity (XRR) analysis.[113-114]

4.2.2 Oxidation

The Si wafer was then diced to produce W coupons with dimensions of 1.6 x 1.6 cm. These W coupons were placed in a reaction chamber that has been described previously.[115] This reaction chamber is similar to other plasma atomic layer deposition (ALD) reactors equipped for *in situ* SE measurements.[67] The chamber walls were coated with ~500 cycles of Al_2O_3 ALD using $Al(CH_3)_3$ and H_2O as the reactants at the chamber wall temperature of 170°C. WO_3 films were prepared by the oxidation of the W ALD films at 280°C using an O_2 plasma at 600 W using an

O_2 pressure of 100 mTorr. The O_2 plasma exposures produced a WO_3 film thickness of 130-150 Å on the W ALD films.

A remote inductively coupled plasma (ICP) provided oxygen radicals for the oxidation of W to WO_3. A quartz tube (6 cm inner diameter x 25 cm long) encircled by a helical copper coil was the ICP source. A 13.56 MHz RF generator (Paramount RF Power Supply, Advanced Energy) and 50 Ω impedance matching network (Navigator Digital Matching Network, Advanced Energy) were used in conjunction to generate the ICP plasma. The distance between the ICP source and the W coupon was ~4 cm.

4.2.3 Spectroscopic Ellipsometry

Etching of the WO_3 and W films was monitored by *in situ* SE using a J.A. Woollam M-2000D ellipsometer. This ellipsometer has a spectral range of 240 to 1700 nm and utilized an incidence angle of 70°. The WO_3 and W films were analyzed to obtain film thicknesses after each reaction cycle or each individual reaction. A schematic showing the film stack and ellipsometer optical beams is shown in Figure 2. Note that the individual layer thicknesses are not to scale. SE has the ability to measure the thicknesses of each individual layer in the film stack. This allows for simultaneous determination of the WO_3 and W film thicknesses.

The WO_3 films were analyzed using the Complete Ease software package from J.A. Woollam. The model employed a Tauc-Lorentz oscillator and a Gaussian oscillator.[43] Only the parameters of the Tauc-Lorentz oscillator model were varied from the starting parameters to increase the accuracy of the model. The metal W layer underneath the WO_3 layer was measured by a B-Spline model.[116] n & k values for bulk W were used as the initial parameters and were varied to fit the experimental data.

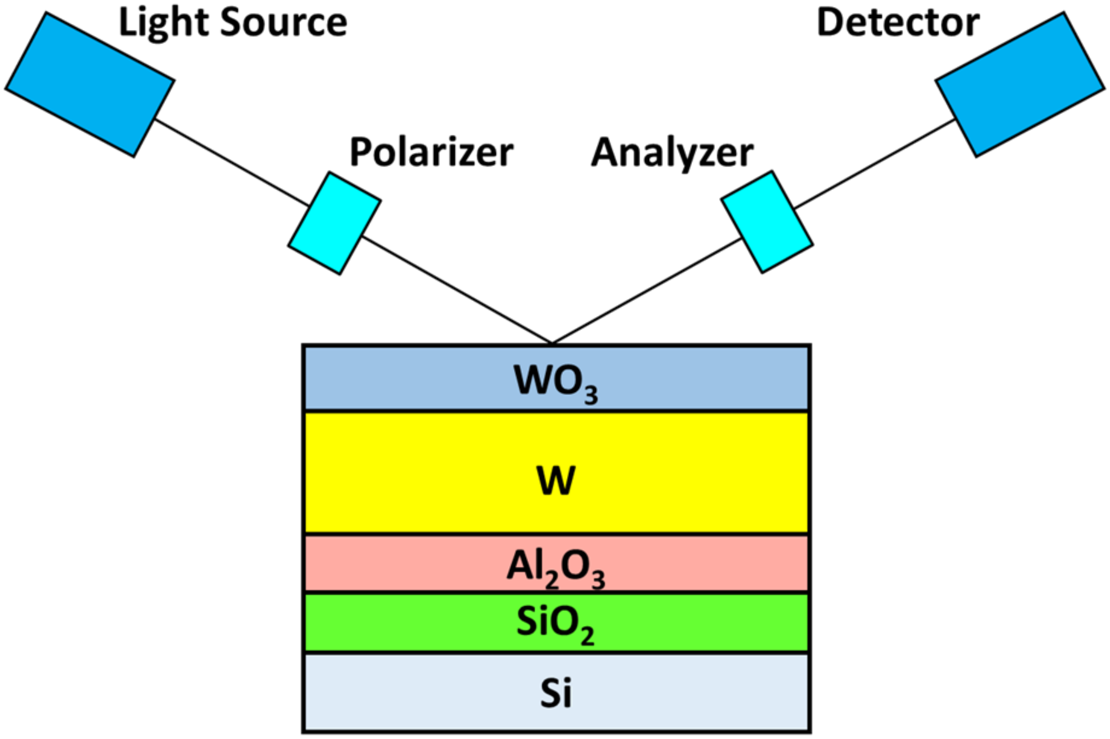

Figure 4-2. Schematic showing ellipsometer beam interacting with film stack comprised of WO_3, W, Al_2O_3 , SiO_2 , and underlying Si substrate.

4.2.4 Precursors and Dosing Parameters

Boron trichloride (99.9%, Synquest Laboratories) and HF-Pyridine (70 wt. % HF, Sigma Aldrich) were used as the reactants. The reactants were separately dosed into the reaction chamber together with a constant stream of ultrahigh purity (UHP) nitrogen. The reactants were introduced using two pneumatic valves (Swagelok-HBVVCR4-C for BCl_3 or Swagelok-6LVV-DPFR4-P-C for HF) on either side of a conductance limiting valve (Swagelok SS-4BMG-VCR). The pneumatic valves were actuated using LabView.

4.2.5 Ozone Generation

In between each reactant exposure, the reaction chamber was purged with UHP nitrogen gas for 130 s at a pressure of 1180 mTorr. The O_3 for the oxidation reaction during W ALE was produced by an O3ONIA ozone generator with oxygen [Airgas, 99.999%]. The gas flow from the ozone generator contained ~10% of O_3 in O_2. The O_2 pressure used for the oxidation reaction was 70 mTorr. Therefore, the O_3 pressure was ~7 mTorr. The HF and BCl_3 purge times were 130 s during W ALE using the O_2/O_3 exposures. The purge time after the O_2/O_3 exposures was 60 s.

Samples were heated on a sample stage inside of the reaction chamber. A constant temperature of 207°C was used for all of the ALE experiments performed to determine the self-limiting conditions. The temperature was initially targeted to be 200°C. A temperature calibration revealed that the temperature was 207°C. The temperature of the sample stage was varied during the studies of WO_3 ALE etch rate versus temperature. The chamber walls were held constant at 170°C. A rotary vane pump (Alcatel 2010) was used to pump the chamber to a base pressure of ~20 mTorr. A capacitance monometer measured the chamber base pressure and pressure transients from each reactant.

4.3 Results and Discussion

4.3.1 WO_3 ALE Using "Conversion Fluorination" with BCl_3 and HF

Figure 3 shows the WO_3 layer thickness measured using *in situ* SE during the etching of the WO_3 layer on the W film. These results were obtained using an AB exposure sequence with BCl_3 and HF as the reactants. Figure 3 displays results for 40 reaction cycles at a substrate temperature at 207°C. The initial WO_3 film thickness is ~150 Å. The WO_3 film thickness decreases linearly until reaching a WO_3 film thickness of ~10 Å. The etching of the WO_3 layer is linear over this range of thicknesses with an etch rate of 4.18 Å/cycle. The SE measurements confirmed that there was no change in the underlying W film thickness during WO_3 etching.

4.3.1.1 WO_3 Etching and W Etch Stop

The WO_3 etch rate is reduced dramatically when the WO_3 layer reaches a thickness of ~10 Å. At this point, the WO_3/W interface is nearby and the WO_3 layer may undergo a transition to WO_x oxides where $x<3$ before reaching the underlying W film. These WO_x oxides may not be amenable to the "conversion-etch" procedure using BCl_3 and HF. As a result, the etch rate slows down when the tungsten oxide layer thickness reaches a thickness of ~5 Å. The underlying W film acts as an etch stop because the W film is not etched by the sequential exposures of BCl_3 and HF.

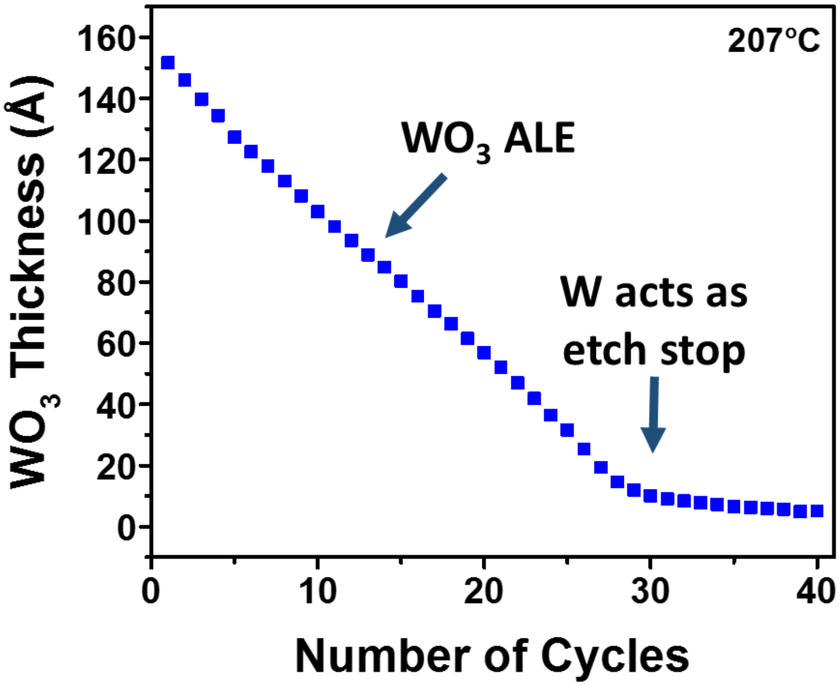

Figure 4-3. WO_3 thickness versus number of cycles showing WO_3 ALE at 207 °C using BCl_3 and HF as reactants. W film under WO_3 layer acts as an etch stop.

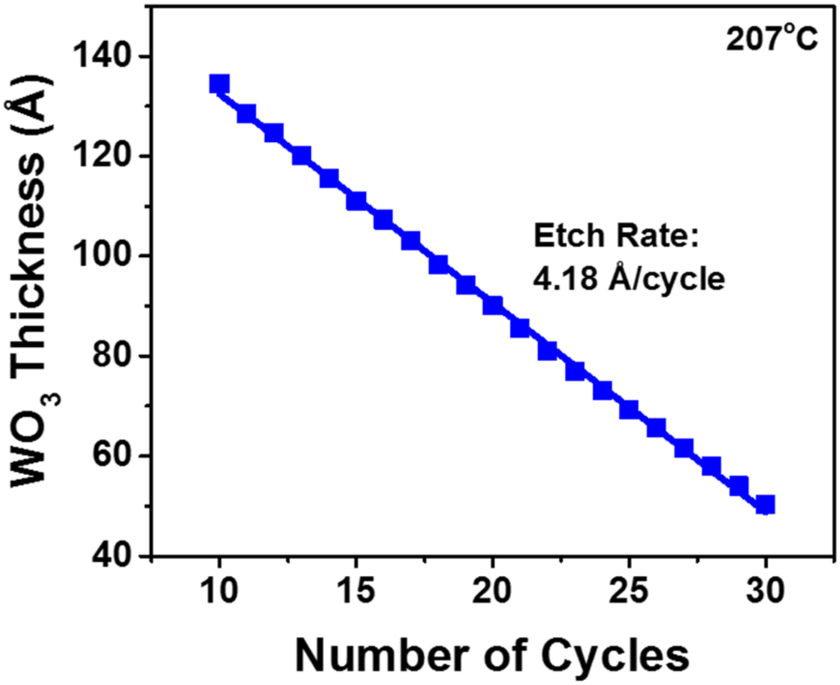

Figure 4-4. WO_3 thickness versus number of cycles showing WO_3 ALE at 207 °C using BCl_3 and HF as reactants. Etch rate during WO_3 ALE is 4.18 Å/cycle.

4.3.1.2 WO_3 Etching Under Self-Limiting Conditions

Figure 4 shows the WO_3 thickness versus number of BCl_3 and HF cycles at 207°C for 20 cycles. The BCl_3 exposures were 325 mTorr s. The maximum BCl_3 pressure during these exposures was ~40 mTorr. The HF exposures were 200 mTorr s. The maximum HF pressure during these exposures was ~60 mTorr. Each dose was followed by an UHP N_2 purge lasting 130 s. The data points in Figure 4 show the individual SE measurements of the WO_3 thickness after each reaction cycle. The etching of WO_3 is linear with an R-squared value of 0.999. The WO_3 etch rate is 4.18 Å/cycle. Multiple measurements of WO_3 ALE at 207°C yielded etch rates that varied from 3.98 – 4.44 Å/cycle. Crystalline WO_3 has a monoclinic structure with cell dimensions a=7.306Å, b=7.540Å, c= 7.692 Å.[117] The WO_3 etch rate is slightly more than one-half of the WO_3 unit cell lengths.

4.3.1.3 B_2O_3 Etching With HF

The etching of WO_3 by BCl_3 and HF occurs by the "conversion-fluorination" mechanism where BCl_3 converts the WO_3 surface layer to a B_2O_3 layer. During the conversion of WO_3 to B_2O_3, the likely reaction product is a volatile WO_xCl_y compound. HF can then spontaneously remove the B_2O_3 layer by forming BF_3 and H_2O as reaction products. The removal of B_2O_3 regenerates the original WO_3 surface and completes one BCl_3/HF reaction cycle. The conversion of WO_3 to B_2O_3 is driven by the higher stability of B_2O_3 compared with WO_3.[91] The etching of B_2O_3 by HF occurs because both BF_3 and H_2O are volatile reaction products.

To prove that B_2O_3 can be spontaneously etched by HF, B_2O_3 films were grown with BCl_3 and H_2O at 20°C. This method was adapted from the previously reported B_2O_3 ALD process with BBr_3 and H_2O as the reactants at 20°C.[118] B_2O_3 films were grown using 600 cycles of BCl_3 and H_2O at 20°C. This B_2O_3 ALD process led to B_2O_3 films with a thickness of ~580 Å. X-ray photoelectron spectroscopy (XPS) analysis of these films was consistent with stoichiometric B_2O_3 films. The B_2O_3 films were then heated to 207°C for the HF exposures.

The B_2O_3 ALD films were exposed to HF pressures of 100 mTorr for 1 s. SE measurements were performed 60 s after the initial HF exposure. The SE measurements were then repeated 12 minutes after the first measurements to verify that no further etching occurred without additional HF exposures. Figure 5 shows the B_2O_3 film thickness versus the number of HF exposures for six HF exposures. Each HF exposure removes ~2 Å of the B_2O_3 film. The second scan recorded after 12 minutes confirms that no additional etching is observed in the absence of HF exposures. These experiments demonstrate that HF can spontaneously etch the B_2O_3 film. The B_2O_3 etching is dependent on the HF pressure and the HF exposure time. The spontaneous B_2O_3 etching will continue for at least 20-30 HF exposures.

4.3.1.4 Self-Limiting Experiments

The self-limiting behavior for the WO_3 etch rate versus the BCl_3 exposure is shown in Figure 6a. The BCl_3 exposures were varied from 0 to 492 mTorr s. The HF exposures were held constant at 200 mTorr s. Increasing the BCl_3 exposure to >225 mTorr s did not produce significantly more WO_3 etching. The BCl_3 reaction with WO_3 is self-limiting at the larger BCl_3 exposures with an etch rate of ~4.2 Å/cycle.

The self-limiting behavior of the HF exposure is shown in Figure 6b. The HF exposure was varied from 0 to 318 mTorr s. BCl_3 exposures were held constant at 327 mTorr s. The WO_3 etch rate increases progressively versus HF exposure. Increasing the HF exposure to >200 mTorr s did not produce significantly more WO_3 etching. The HF reaction with WO_3 is self-limiting at larger HF exposures with a etch rate of ~4.2 Å/cycle.

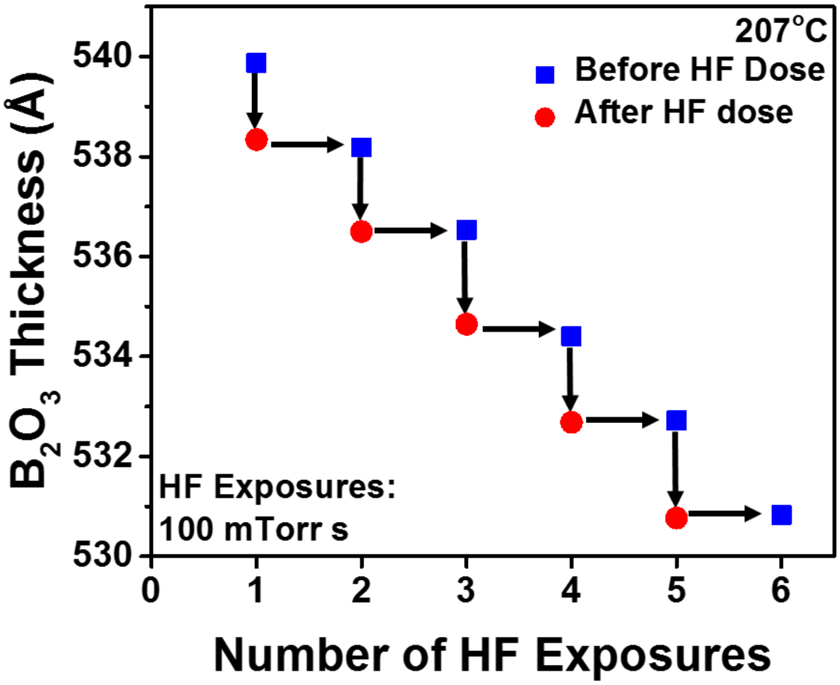

Figure 4-5. B_2O_3 thickness versus number of HF exposures showing spontaneous etching of B_2O_3 film at 207 °C. HF exposure was 100 mTorr s, and B_2O_3 etch rate is ~2 Å per HF exposure.

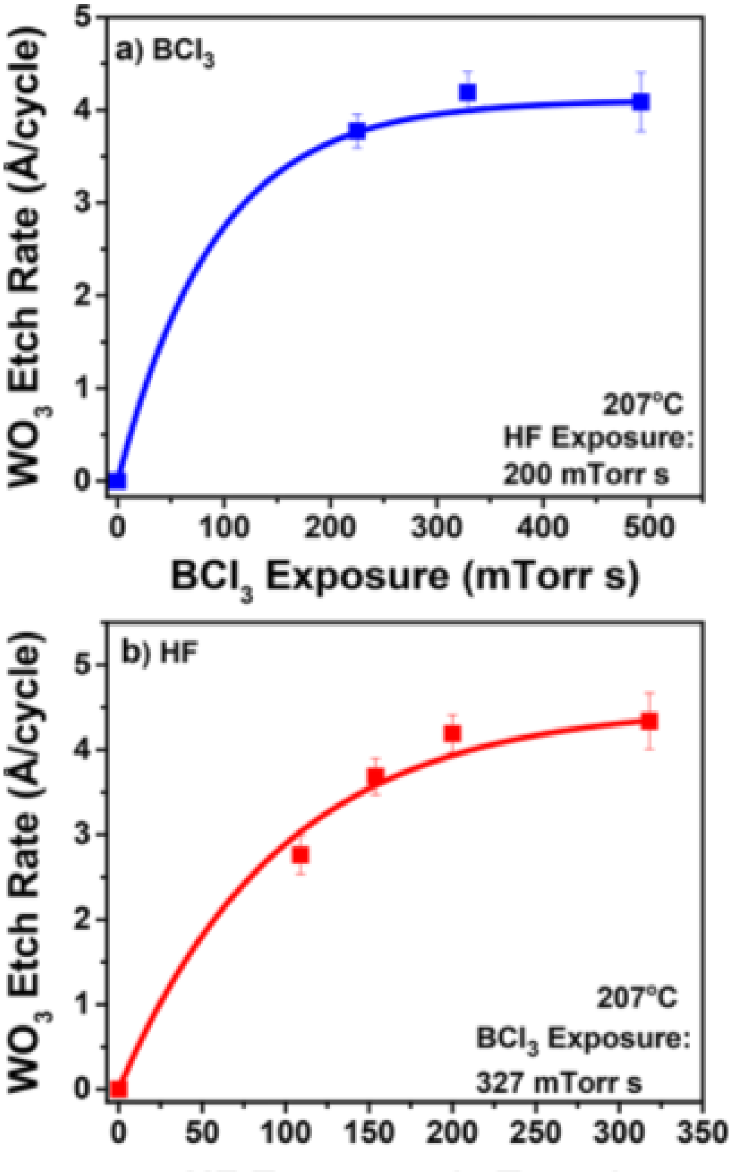

Figure 4-6. WO_3 etch rate versus reactant exposure during WO_3 ALE at 207 °C. (a) BCl_3 exposure was varied with HF exposure held at 200 mTorr s. (b) HF exposure was varied with BCl_3 exposure held at 327 mTorr s.

4.3.1.5 Determination of Etch Pathway

Figure 7 shows SE measurements that were recorded after each BCl_3 and HF exposure during WO_3 ALE at 207°C for 26 half-cycles. The WO_3 thickness decreases linearly with the number of half-cycles. An expansion of the WO_3 thickness versus number of half-cycles for four half-cycles is displayed in Figure 8. The SE model assumed that the entire film was WO_3. Adding a Cauchy layer to account for the B_2O_3 layer on the WO_3 film after the BCl_3 conversion reaction did not improve the SE fitting. Figure 8 indicates that the WO_3 thickness etched in one BCl_3/HF cycle is 4.29 Å. The thickness loss after the BCl_3 exposure is 2.99 Å. The thickness loss after the HF exposure is 1.30 Å.

The WO_3 thickness loss of 4.29 Å during one complete cycle represents 1.32×10^{-9} WO_3 mol/cm^2 based on a WO_3 density of 7.16 g/cm^3 and a WO_3 molar mass of 231.8 g/mol. During the WO_3 etching, WO_3 can be converted to various amounts of B_2O_3 depending on the possible BCl_3 conversion reactions given by Equations 3-5. The thickness loss of 2.99 Å after the BCl_3 exposure leaves a B_2O_3 thickness of 1.30 Å on the surface. The SE modeling assumes that the B_2O_3 thickness can be modelled as indistinguishable from a WO_3 thickness. This B_2O_3 thickness is then removed by the subsequent HF exposure.

The B_2O_3 thickness of 1.30 Å on the surface prior to removal by HF is in agreement with the BCl_3 conversion reaction given by Equation 5. This BCl_3 conversion reaction yields WO_2Cl_2 as the volatile reaction product. Based on Equation 5, the predicted B_2O_3 thickness remaining on the surface after the conversion of 4.29 Å of WO_3 or 1.32×10^{-9} WO_3 mol/cm^2 is 1.25 Å. The predicted B_2O_3 thickness of 1.25 Å agrees well with the measured B_2O_3 thickness of 1.30 Å. Mass spectrometry studies are needed to confirm WO_2Cl_2 as the volatile reaction product.

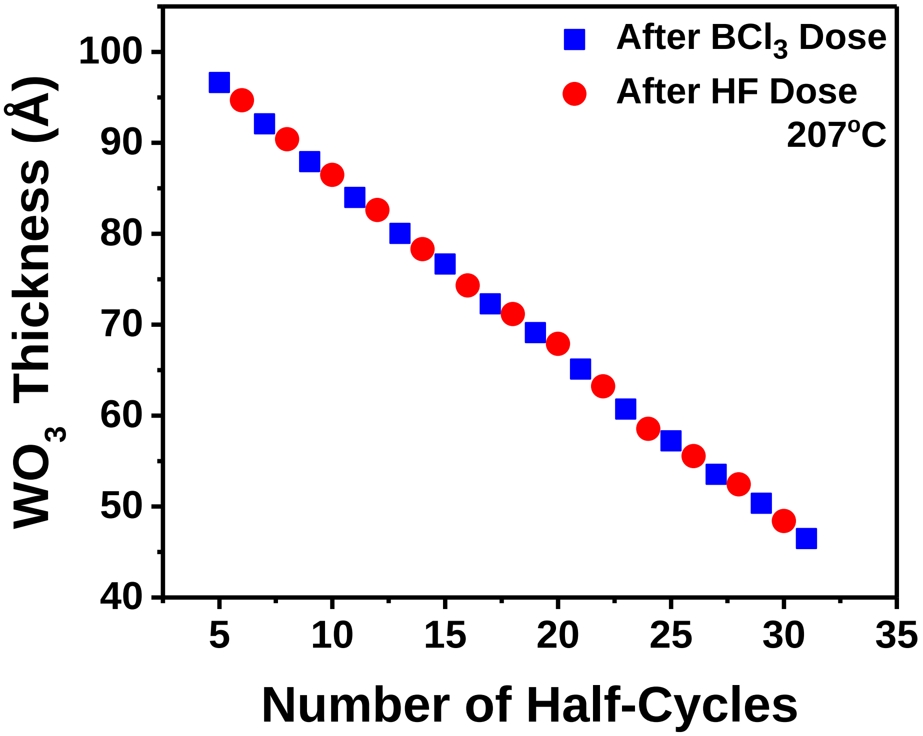

Figure 4-7. WO_3 thickness versus number of half-cycles during WO_3 ALE at 207 °C under self-limiting conditions.

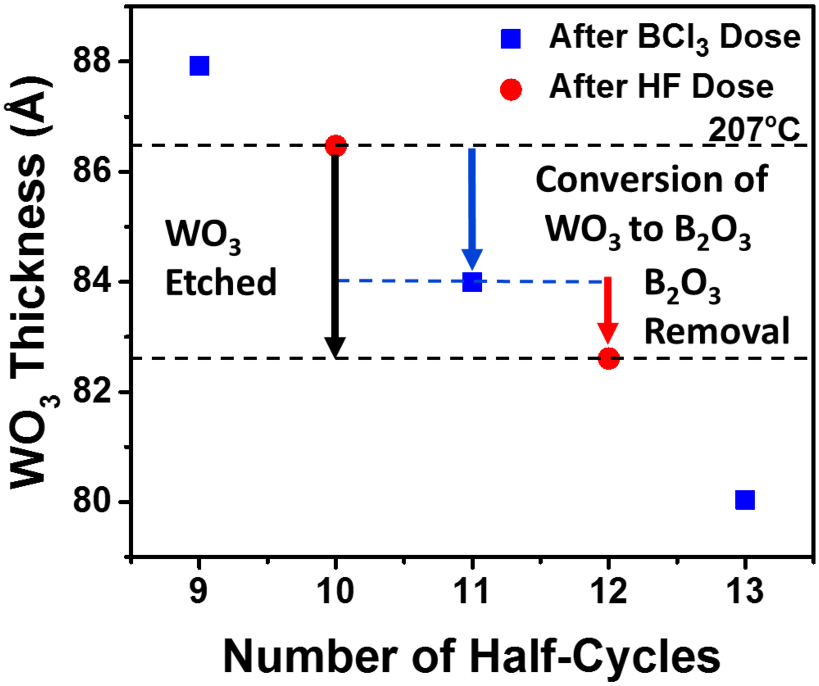

Figure 4-8. Analysis of WO_3 thickness change after BCl_3 exposure and HF exposure during WO_3 ALE at 207 °C.

4.3.1.6 Etch Dependence on Temperature

The WO_3 film thicknesses versus number of BCl_3 and HF reaction cycles at different substrate temperatures are shown in Figure 9. The self-limiting reaction conditions at 207°C were used for all of the various temperatures. The self-limiting conditions were a BCl_3 exposure of 325 mTorr s and a HF exposure of 200 mTorr s. All of the initial WO_3 thicknesses were referenced to a starting value of 140 Å to compare the results at 128, 160, 196, and 207°C. For all of the temperatures, the WO_3 etching is linear with the number of reaction cycles. The etch rate also increases at higher temperatures. The etch rates are 0.55, 2.04, 2.95 and 4.19 Å/cycle at 128, 160, 196, and 207°C, respectively.

4.3.1.7 Arrhenius Plot

Figure 10 shows an Arrhenius plot of all the etch rates at different temperatures acquired from the SE measurements. The approximately linear plot of ln (etch rate) versus 1/T shows that the etch rates are nearly exponentially dependent on temperature. The temperature dependent WO_3 etch rate exhibits an activation energy of 8.6 kcal/mol. The temperature dependence of the WO_3 etch rate provides a means to control the WO_3 etch rate.

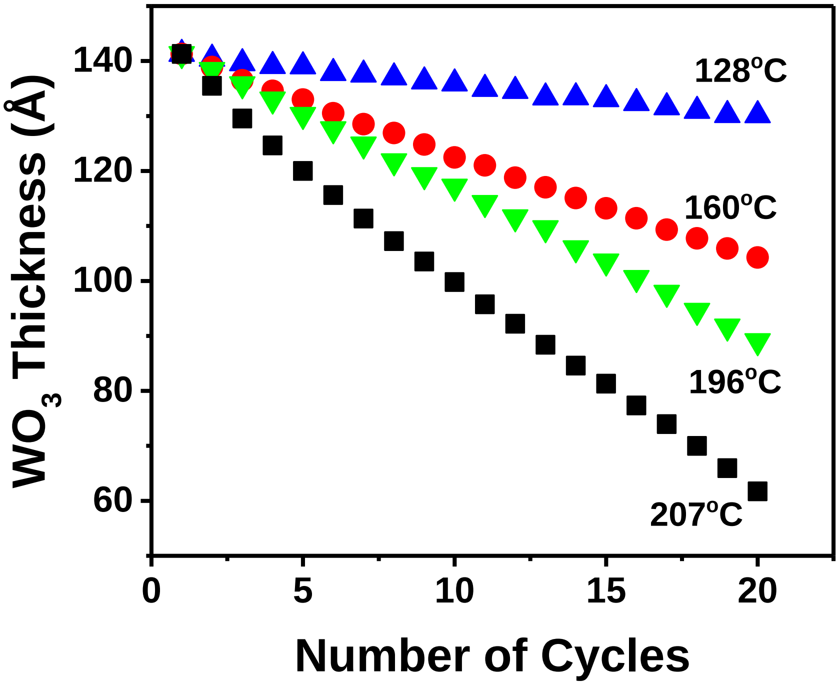

Figure 4-9. WO_3 thickness versus number of cycles for WO_3 ALE at 128, 160, 196, and 207 °C.

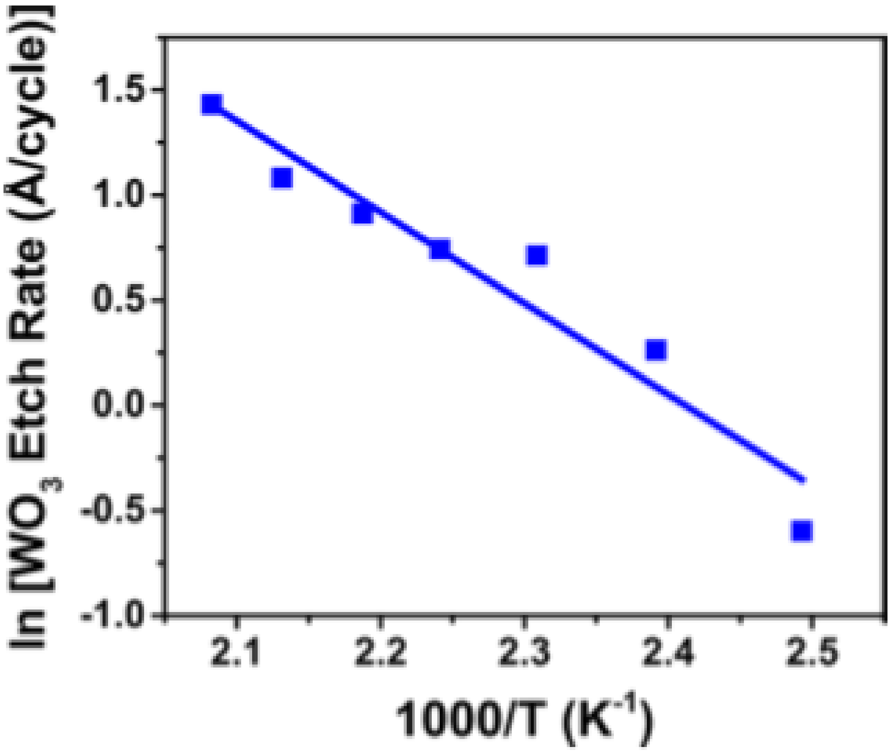

Figure 4-10. Arrhenius plot of temperature-dependent etch rates for WO_3 ALE. Slope of the Arrhenius plot yields an activation barrier of 8.6 kcal/mol.

4.3.2 W ALE Using "Oxidation-Conversion-Fluorination" with O_3, BCl_3 and HF

4.3.2.1 W Etching Under Self-Limiting Conditions

The development of WO_3 ALE opens a pathway to W ALE. Tungsten can first be oxidized to WO_3. Subsequently, WO_3 can be etched using sequential BCl_3 and HF exposures as described above in Section III.A. The oxidation of W to produce WO_3 must be self-limiting to obtain atomic layer control of W etching. This requirement is demanding because oxidation of metals is generally very favorable and often the oxidation can extend deep into the initial metal.

Tungsten oxidation has been studied extensively over a variety of temperatures and oxidation conditions. Many investigations have been reported at high temperatures >500°C where tungsten oxidizes readily to form WO_3 and other tungsten oxides.[119-120] At temperatures >800°C, these oxides can also desorb into the gas phase.[121] At temperatures between 300-400°C, tungsten is oxidized by O_2 to form a WO_3 layer with thicknesses of 10-50 nm.[122-124] The WO_3 layer acts as a diffusion barrier that limits further oxidation.[125]

At lower temperatures <300°C, the tungsten oxidation is limited to thin WO_3 films on the W substrate.[122, 124, 126] Oxide thicknesses of 10-16 Å have been reported after O_2 exposures on polycrystalline W substrates for 1 hour at 23-200°C.[124] Somewhat thicker oxide thicknesses have been measured when using O_2 plasmas to oxidize tungsten at lower temperatures.[127-128] Tungsten oxidation at these lower temperatures is compatible with the temperature for WO_3 ALE and also is self-limiting at thin film thicknesses that are required for an ALE process. Figure 11 shows results for the tungsten thickness versus number of ABC reaction cycles during W ALE at 207°C. In these experiments, the surface of the W film was oxidized to WO_3 using O_2/O_3 pressures of 70 mTorr. The WO_3 layer was then etched using the next BCl_3 and HF exposures. The W ALE was conducted under self-limiting conditions for the O_3, BCl_3, and HF reactions at 207°C as discussed below. The O_2/O_3 exposure was 3150 mTorr s, the BCl_3 exposure was 329 mTorr s and the HF exposure was 2800 mTorr s.

Figure 11 reveals that the tungsten film thickness decreases linearly versus number of cycles. The etch rate is 2.56 Å/cycle and the R-squared value of the linear fit is 0.996. Multiple SE measurements of W ALE at 207°C yielded etch rates that varied from 2.35 – 2.56 Å/cycle. XRR measurements confirmed the SE measurements. The W etch rate at 207°C is slightly less than one unit cell length. W has a body-centered cubic structure with a unit cell length of 3.19 Å.

4.3.2.2 Analysis of WO_3 and W Films During Etching

The WO_3 and W layer thicknesses could be determined simultaneously using SE measurements during W ALE. Figure 12 shows the concurrent SE measurements of the WO_3 and W film thicknesses versus number of half-cycles at 207°C. The half-cycles are the O_2/O_3 oxidation reaction and the BCl_3/HF etching reaction. The O_2/O_3 exposure was 3150 mTorr s, the BCl_3 exposure was 329 mTorr s and the HF exposure was 2800 mTorr s. The ellipsometry measurements were performed after each half-cycle. The SE measurements were able to monitor both the growth and etching of the WO_3 layer and the concurrent removal of the underlying W film.

With an ABC exposure sequence, the WO_3 thickness is increased during W oxidization by O_2/O_3 and then decreased during the BCl_3 and HF etching reactions. The oxidation and etching leads to an oscillatory WO_3 thickness in Figure 12a versus the number of half-cycles. The increase in the WO_3 thickness from oxidation is 7.2 Å/half-cycle averaged over five random half-cycles after 12 half-cycles. The decrease in the WO_3 thickness from the BCl_3/HF etching is 7.7 Å/half-cycle averaged over five random half-cycles after 12 half-cycles.

The WO_3 thickness loss of ~7.7 Å after the BCl_3/HF reactions during W ALE at 207°C is larger than the WO_3 thickness loss of ~4.2 Å/cycle during WO_3 ALE at 207°C. WO_3 ALE is performed with BCl_3 and HF as the reactants. W ALE is performed with O_2/O_3, BCl_3 and HF as the reactants. The addition of the O_2/O_3 exposure may alter the surface species and affect the BCl_3/HF reactions. Additional experiments were conducted where O_2/O_3 was removed from the ABC exposure sequence and WO_3 ALE was performed on WO_3 films produced using O_2/O_3. These experiments observed a WO_3 etch rate of ~4.2 Å/cycle that is the same as the etch rate of ~4.2 Å/cycle for WO_3 films produced using an O_2 plasma. The WO_3 etching is not dependent on the oxidant used to form the WO_3 film.

Figure 12a also observes an increase in the WO_3 thickness from ~30 Å to ~40 Å during the first 10 half-cycles. This increase is followed by a reduction to an oxide thickness of ~20 Å after 60 half-cycles. The change in the WO_3 thickness results from the competition between WO_3 growth during the O_2/O_3 exposures and WO_3 etching during the BCl_3/HF reactions. Higher or lower O_2/O_3 exposures were observed to result in more or less WO_3 growth. The presence of a maximum WO_3 thickness after 10 half-cycles in Figure 12a may be related to nucleation effects combined with the competition between WO_3 growth and WO_3 etching. Concurrent ellipsometry measurements of the W thickness are shown in Figure 12b. While the WO_3 thickness is oscillating during the oxidation and etching half-cycles, the W thickness is reduced linearly versus number of half-cycles. The W etching rate is 2.44 Å/cycle. A small oscillation of the W thickness was observed over the first 30 half-cycles. The decreases in the

W thickness during the half-cycles occur after the O_2/O_3 exposures when W is oxidized to WO_3. This slight oscillation may be an artifact from the ellipsometric modeling.

4.3.2.3 Expansion of WO_3 During "Oxidation-Conversion-Etch"

An expansion of the oscillation in the WO_3 thickness in Figure 12a is shown in Figure 13. The increase of the WO_3 thickness during oxidation and the reduction of the WO_3 thickness during etching for 6 consecutive half-cycles are dramatic. Values of the individual WO_3 thickness increases and decreases are given in Figure 13. In addition, the increase in the WO_3 thickness from oxidation is 7.2 Å/half-cycle averaged over five random half-cycles after 12 half-cycles in Figure 12a. The decrease in the WO_3 thickness from the BCl_3/HF etching is 7.7 Å/half-cycle averaged over five random half-cycles after 12 half-cycles in Figure 12a.

The ratio of the WO_3 thickness gain per half-cycle and the W thickness loss per cycle should be equal to the ratio of the WO_3 and W molar volumes. This expectation is based on conservation of tungsten mass where a W loss must equal a WO_3 gain. The ratio of the WO_3 gain and W loss is 7.2 (Å/half-cycle)/2.44 (Å/cycle) = 2.95. In comparison, the ratio of the molar volumes for WO_3 and W is (32.4 cm^3/mol) / (9.5 cm^3/mol) = 3.4. The ratio of the molar volumes is only slightly higher than the ratio of the etch rates. This reasonable agreement is confirmation that W ALE occurs by conversion of W to WO_3 followed by the etching of WO_3. The slight differences in the ratios may also be explained by some WO_2 in the tungsten oxide layer. Compared with WO_3, WO_2 has a smaller molar volume of 20.0 cm^3/mol. The molar volume of a mixture of WO_3/WO_2 would lower the ratio of the molar volumes for WO_3/WO_2 and W.

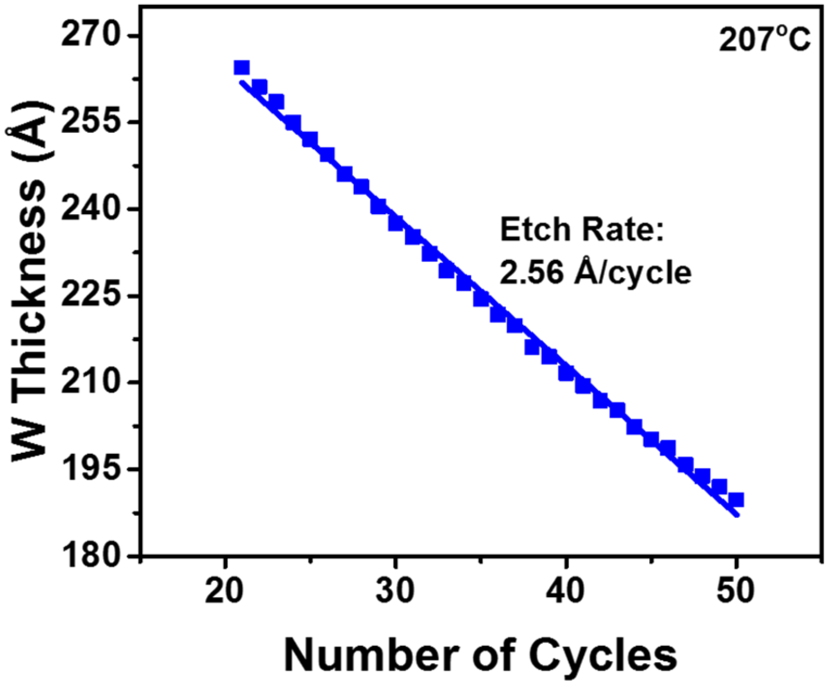

Figure 4-11. W thickness versus number of cycles during W ALE at 207 °C using O_2/O_3, BCl_3, and HF as reactants. Etch rate during W ALE is 2.56 Å/cycle

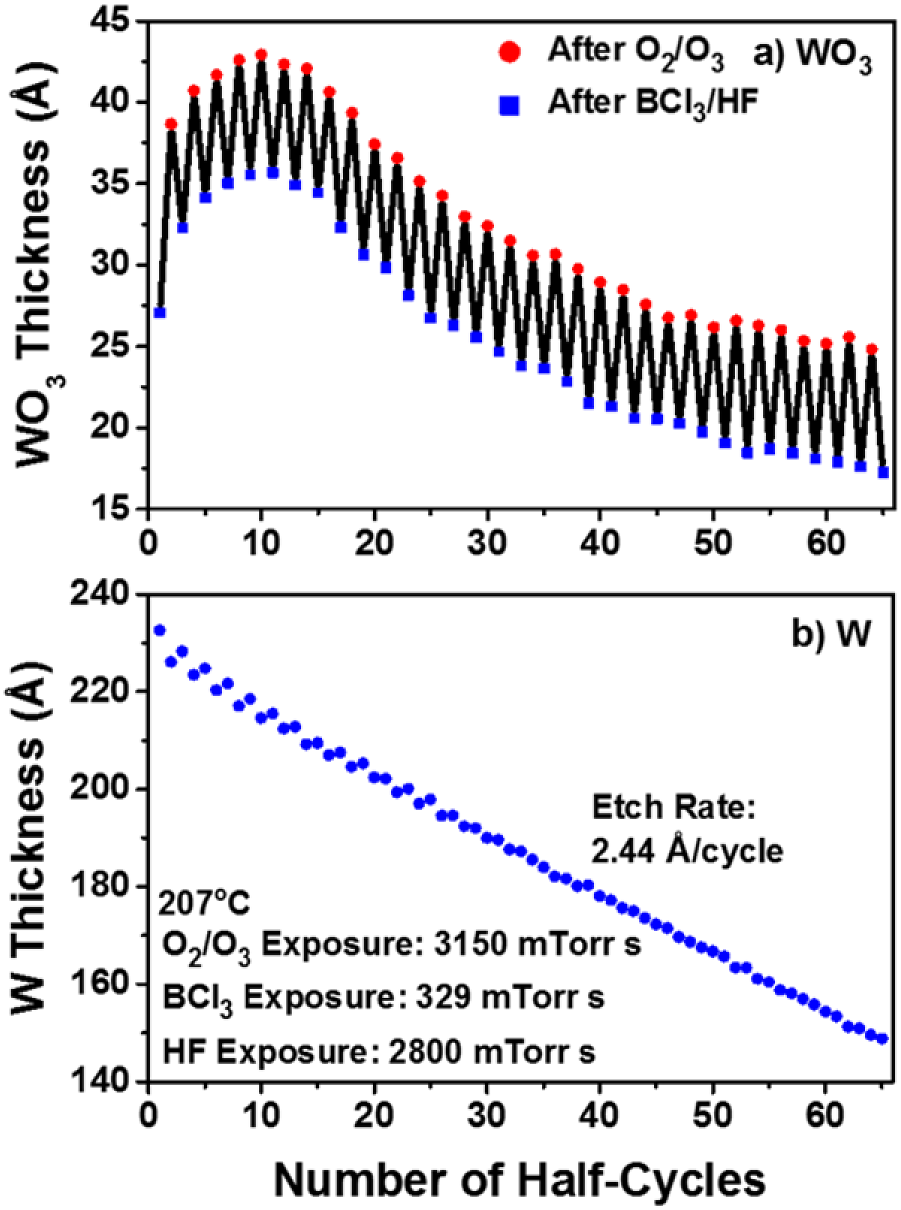

Figure 4-12. WO3 and W thicknesses versus number of half-cycles during W ALE under self-limiting conditions using O_2/O_3, BCl_3, and HF as reactants at 207 °C. (a) WO3 thickness showing oscillation of WO_3 thickness after O_2/O_3 exposure and BCl_3/HF reaction. (b) W thickness showing linear reduction versus number of half-cycles with an etch rate of 2.44 Å/cycle.

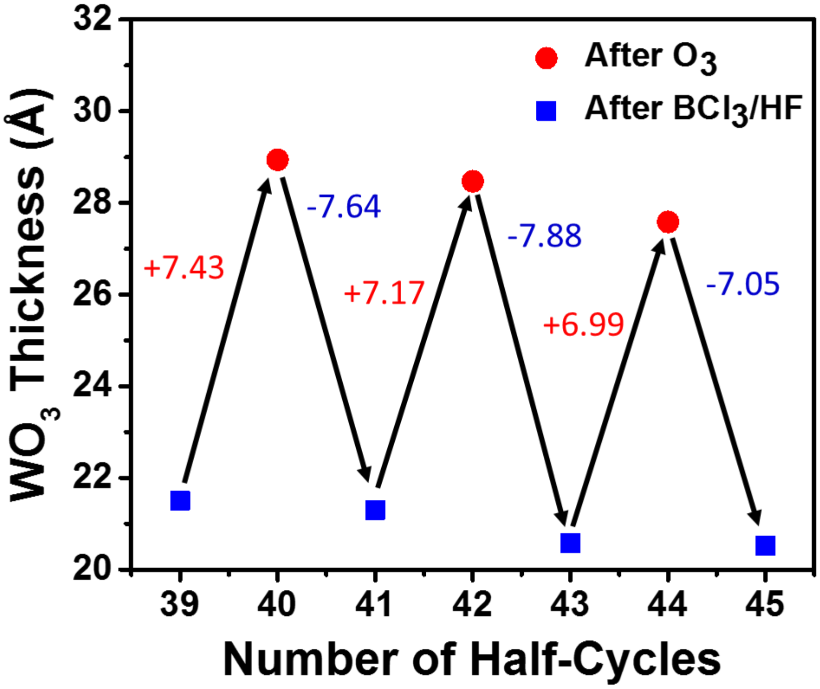

Figure 4-13. Enlargement of WO_3 thickness versus number of halfcycles showing increase and decrease of WO3 thickness after O_2/O_3 exposure and BCl_3/HF reaction.

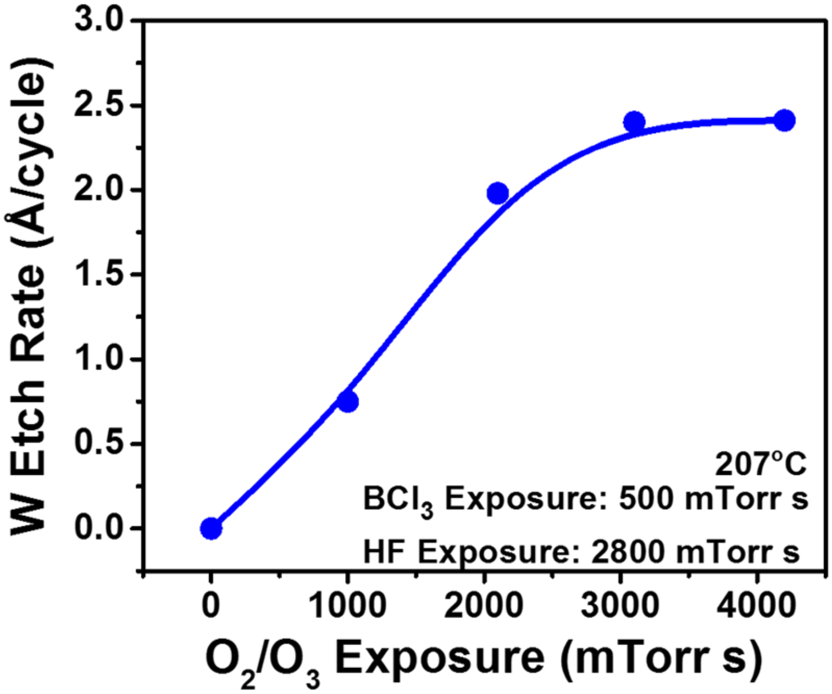

Figure 4-14. W etch rate versus O_2/O_3 exposure during W ALE at 207 °C. BCl_3 and HF exposures were held at 500 and 2800 mTorr s, respectively.

4.3.2.4 Self-Limiting Conditions for W ALE

The self-limiting nature of the O_2/O_3, BCl_3 and HF reactions is critical to establish a W ALE process. Self-limiting BCl_3 and HF reactions have already been established during the characterization of WO_3 ALE as shown in Figure 6. The self-limiting behavior of the O_2/O_3, BCl_3 and HF reactions during W ALE also needs to be verified to confirm a self-limiting procedure for W ALE.

Figure 14 displays the W etch rate versus O_2/O_3 exposure during the ABC reaction sequence at 207°C. The pressure of the O_2/O_3 exposure was 70 mTorr for the different exposure times of 15, 30, 45 and 60 s. HF and BCl_3 exposures were held constant at 2800 mTorr s and 500 mTorr s, respectively. The HF and BCl_3 pressures were 535 and 60 mTorr, respectively, during these exposures. Figure 14 shows that the W etch rate increases with O_2/O_3 exposure and reaches a maximum etch rate of 2.45 Å/cycle at an O_2/O_3 exposure of 3150 mTorr s. The line fitting the data points is meant to guide the eye.

Results for the W etch rate versus BCl_3 or HF exposure during W ALE at 207°C are shown in Figure 15a and 15b, respectively. These measurements were performed by varying one reactant exposure and holding the other two reactant exposures constant. BCl_3 and HF were dosed into a stream of UHP N_2 that was at a pressure of 1180 mTorr. A purge of 130 s was employed after each reactant exposure. The O_2/O_3 exposure was 3150 mTorr s conducted at a O_2/O_3 pressure of 70 mTorr. A purge of 60 s was used after each O_2/O_3 exposure.

Figure 15a shows the results for varying the BCl_3 exposure while holding the HF and O_2/O_3 exposures constant at 2800 mTorr s and 3150 mTorr s, respectively. The BCl_3 exposures were varied from 0 to 500 mTorr s. The BCl_3 exposure converts the WO_3 surface to a B_2O_3 surface layer. The B_2O_3 surface layer is then spontaneously etched by HF. The W etch rate increases rapidly with BCl_3 exposure. With a BCl_3 exposure of 329 mTorr s, the W etch rate reaches the self-limiting W etch rate of 2.45 Å/cycle.

Figure 15b shows the results for varying the HF exposure while holding the BCl_3 and O_2/O_3 exposures constant at 500 mTorr s and 3150 mTorr s, respectively. Higher HF exposures progressively remove the B_2O_3 surface layer as volatile BF_3 and H_2O. With HF exposures of 2800 mTorr s, the W etch rate reaches the self-limiting W etch rate of 2.45 Å/cycle.

4.3.2.5 Oxidation of W by O_2/O_3

Additional experiments examined the oxidation of the W ALD films by successive O_2/O_3 exposures at 207°C. The O_2/O_3 exposures were 3150 mTorr s resulting from O_2/O_3 pressure of 70 mTorr for 45 s. This is the same O_2/O_3 exposure that was employed in the W ALE experiments. The W ALD films had been exposed to atmosphere prior to loading into the reactor. The WO_3 thickness on the W ALD film was then measured by SE after each O_2/O_3 exposure. The WO_3 thicknesses versus number of O_2/O_3 exposures are displayed in Figure 16.

The initial WO_3 thickness in Figure 16 is ~33 Å. This thickness is close to the native oxide thicknesses on tungsten that have been measured earlier with XPS and XRR analysis.[113-114] The WO_3 thickness is nearly constant at ~33 Å after the first three O_2/O_3 exposures. This constant oxide thickness may be related to the O_2/O_3 exposure cleaning residual carbon from the surface. Figure 16 then shows that the WO_3 thickness increases consistently after the 3rd O_2/O_3 exposure. However, the increase is progressively reduced after each O_2/O_3 exposure. This behavior is suggestive of diffusion-limited oxidation when the surface oxide acts as a barrier for oxidation of the underlying W metal. Similar behavior is also observed for the diffusion-limited oxidation of silicon described by the Deal-Grove model.[125] The WO_3

thickness is ~66 Å after 34 O_2/O_3 exposures. XPS analysis of the WO_3 film produced by these O_2/O_3 exposures was consistent with stoichiometric WO_3 with W in the 6+ oxidation state.

The larger WO_3 thicknesses produced by greater number of sequential O_2/O_3 exposures may lead to W etch rates that are higher after larger O_2/O_3 exposures. However, Figure 14 shows that the W etch rate is self-limiting versus O_2/O_3 exposure. This behavior suggests that the W ALE is self-limiting because of the self-limiting BCl_3 and HF reactions. Larger O_2/O_3 exposures may lead to larger WO_3 film thicknesses. However, the WO_3 removal is still limited by the self-limiting BCl_3 and HF reactions. The BCl_3 and HF reactions may only remove a fraction of the WO_3 film. After partial removal of the WO_3 film, the next O_2/O_3 exposure would then reestablish a larger WO_3 film thickness that is consistent with the O_2/O_3 exposure.

Additional experiments were performed at 207°C by varying the O_2/O_3 exposure times with an O_2/O_3 pressure of 70 mTorr under self-limiting conditions for the BCl_3 and HF reactions. O_2/O_3 exposure times of 45 s and 60 s both produced W ALE etch rates of 2.45 Å/cycle. However, the WO_3 film thickness was ~20 Å for the 45 s O_2/O_3 exposures (3150 mTorr s) and ~30 Å for the 60 s O_2/O_3 exposures (4200 mTorr s) after >20 reaction cycles. The consequence of larger O_2/O_3 exposure times at constant O_2/O_3 pressures is thicker WO_3 thicknesses during W ALE. However, the W ALE etch rates remain the same. These results argue that W ALE is self-limiting because of the self-limiting BCl_3 and HF reactions.

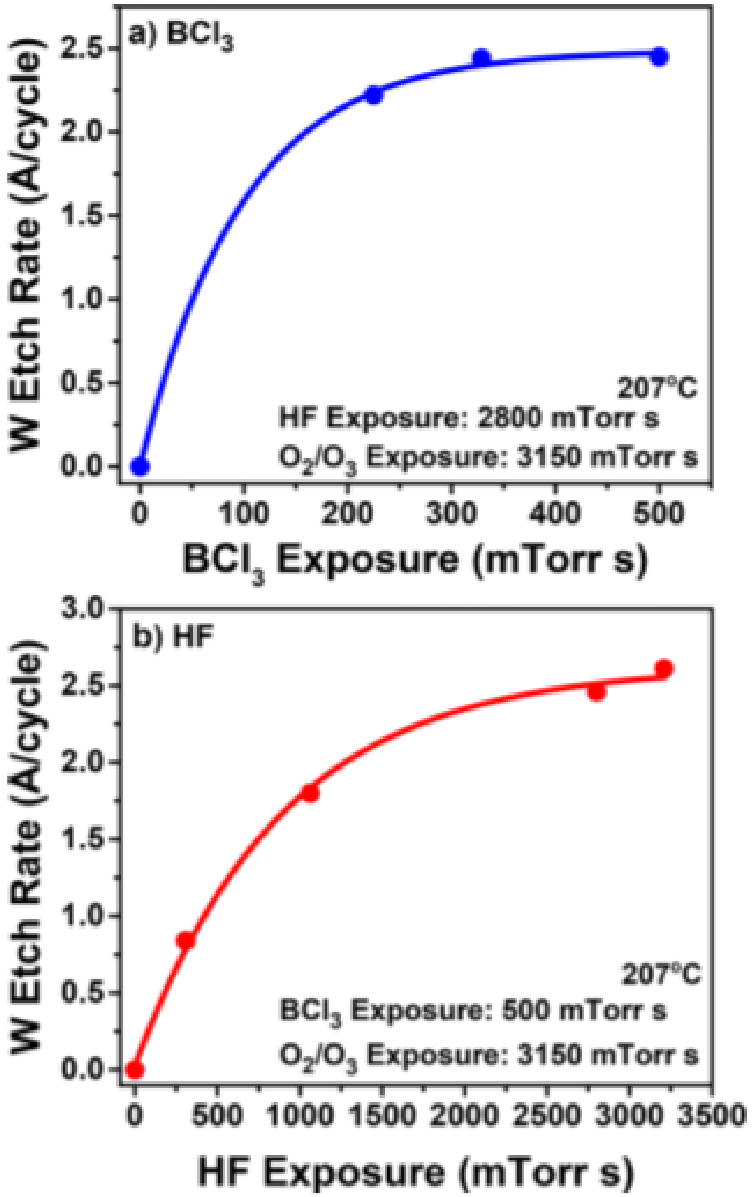

Figure 4-15. W etch rate versus reactant exposure during W ALE. (a) BCl3 exposure was varied with HF and O2/O3 exposures held at 2800 and 3150 mTorr s, respectively. (b) HF exposure was varied with BCl3 and O2/O3 exposures held at 500 and 3150 mTorr s, respectively.

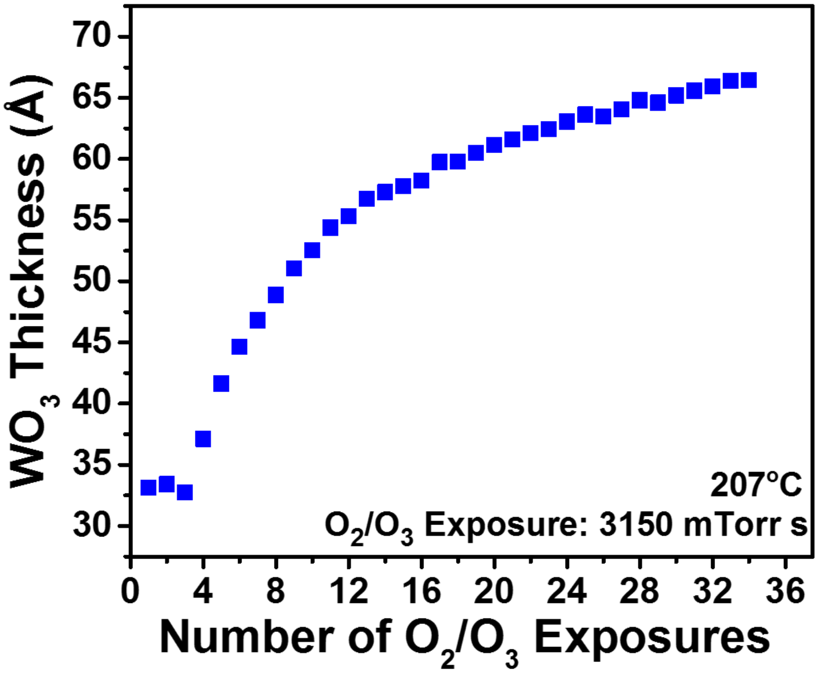

Figure 4-16. WO3 thickness versus number of O_2/O_3 exposures for initial W ALD film. Each O_2/O_3 exposure was 70 mTorr for 45 s.

4.3.2.6 WO_3 Removal After W ALE

Figure 12a shows that the WO_3 thickness is reduced to a thickness of ~20 Å after 60 half-cycles during W ALE with an O_2/O_3 pressure of 70 mTorr and O_2/O_3 exposure time of 45 s under self-limiting conditions for the BCl_3 and HF reactions. Removal of this WO_3 layer on W may be important for applications where no oxide is desired for proper device function. This WO_3 layer can be removed by stopping the O_2/O_3 exposures and utilizing an AB reaction sequence with BCl_3 and HF exposures. Figure 17a displays the removal of the WO_3 layer after W ALE versus the number of BCl_3/HF reaction cycles using the self-limiting reaction conditions for WO_3 ALE at 207°C. The WO_3 layer thickness is reduced in thickness from 20 Å to a limiting thickness of ~3 Å after >12 reaction cycles.

The corresponding W film thickness during the removal of the WO_3 layer is shown in Figure 17b. While the WO_3 layer is removed during the AB reaction sequence, the W film thickness is nearly constant. The initial W film thickness is ~218 Å. The W film thickness reaches 215-216 Å after >12 reaction cycles. These results indicate that the WO_3 layer on W can be removed with almost no effect on the W thickness. There are also alternative methods to remove the WO_3 layer based on hydrogen reduction using H_2 or H_2 plasma exposures.[122, 127, 129]

The self-limiting conditions for the BCl_3 and HF exposures during WO_3 ALE at 207°C were 325 mTorr s and 200 mTorr s, respectively. In comparison, the self-limiting conditions for the O_2/O_3, BCl_3 and HF exposures during W ALE at 207°C were 3150 mTorr s, 325 mTorr s and 2800 mTorr s, respectively. The self-limiting conditions for the HF exposure are very different for WO_3 and W ALE. The inclusion of the O_2/O_3 exposure in the ABC reaction sequence for W ALE leads to a much larger self-limiting HF exposure. The chamber walls are coated with

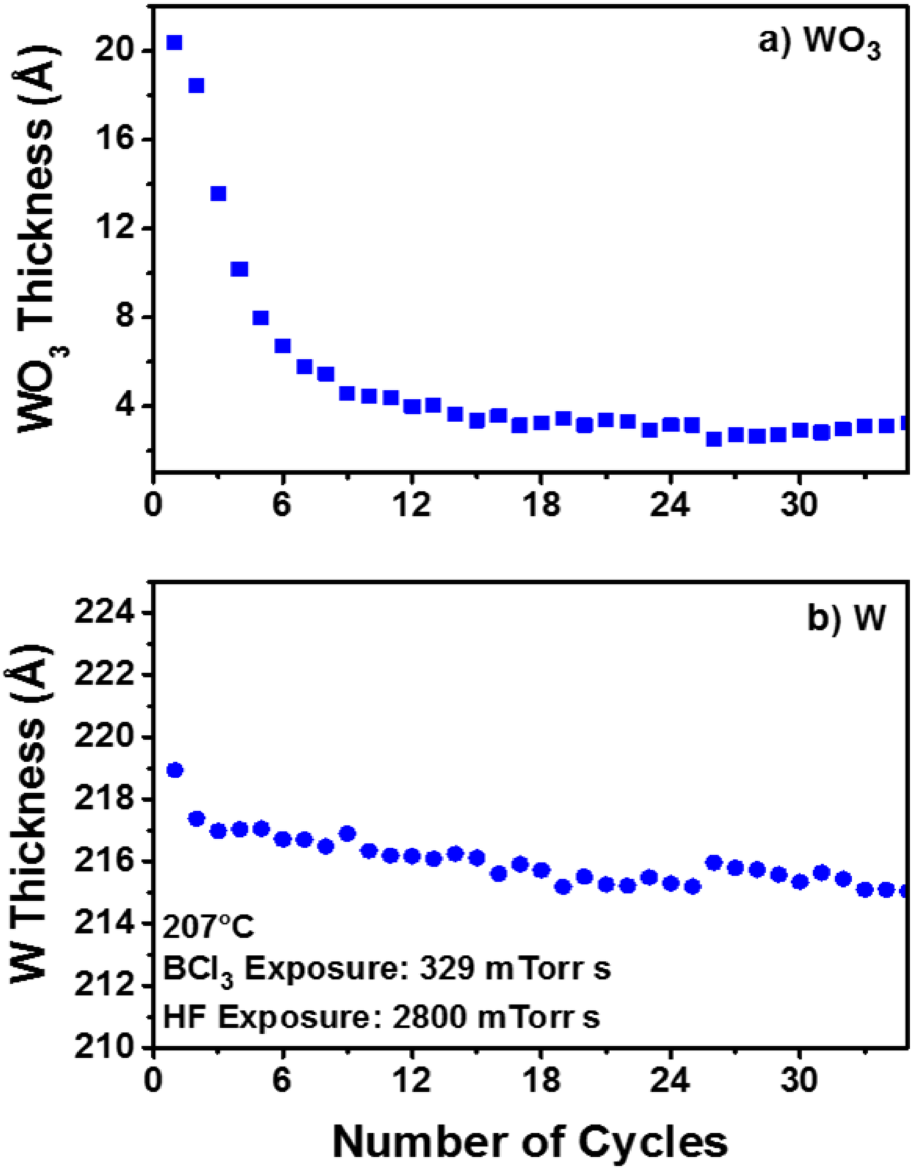

Figure 4-17. WO removal after W ALE using BCl3 and HF as reactants. (a) WO_3 thickness versus number of cycles showing reduction of WO3 thickness to limiting value of ~3 Å. (b) W thickness versus number of cycles showing that W thickness remains nearly constant during WO_3 removal.

Al_2O_3 ALD and HF is known to adsorb on Al_2O_3 at the chamber wall temperature of 170°C.[85] The O_2/O_3 exposure may remove HF from the chamber walls. Larger HF exposures may then be required during the subsequent BCl_3/HF reaction to replace the adsorbed HF and obtain self-limiting behavior.

4.3.3 Extension to additional materials

The “conversion-fluorination” and “oxidation-conversion-fluorination” mechanisms can be useful for the ALE of a variety of additional metal materials. These mechanisms will be valuable because some metal materials cannot be etched using the fluorination and ligand-exchange mechanism.[55-56] Fluorination of many metal materials is not thermodynamically favorable with HF. However, stronger fluorination reactants, like SF_4 and XeF_2, can lead to volatile metal fluorides and spontaneous etching. The highly exothermic reaction of stronger fluorination reagents with metal materials can also lead to fluoride layers too thick for ALE. Some metal materials are also difficult to fluorinate because they do not have stable fluorides in the same oxidation state as the initial metal material. Other metal materials can be fluorinated but do not easily yield volatile products during the ligand-exchange reaction.

4.3.3.1 Conversion Etch with BCl_3

BCl_3 is important for the conversion of many initial metal oxides to B_2O_3 because B_2O_3 is a stable metal oxide and many metals have volatile chlorides or oxychlorides. Metals with volatile chlorides or oxychlorides include W, V, Nb, Ta, Cr, Mo, Fe, Au, Ga, Ge, Sn, As, Sb, Zr and Hf. The spontaneous etching of B_2O_3 by HF also plays a key role in the new conversion etching mechanisms. HF can spontaneously etch B_2O_3. However, HF cannot spontaneously etch many other metal oxides. Consequently, if the initial metal oxide can be converted to B_2O_3, then HF can spontaneously etch B_2O_3 and the underlying initial metal oxide will serve as an etch stop.

Table 1 explores the thermochemistry of a variety of conversion reactions for various metal oxides. Most of these metal oxides will have difficulty achieving self-limiting ALE using fluorination and ligand-exchange reactions. The reasons for the difficulty include: (1) formation of volatile fluorides that lead to spontaneous etching (WO_3, MoO_3, VO_2, V_2O_5, Ta_2O_5, GeO_2, As_2O_3, Au_2O_3, SbO_2, Sb_2O_3, NbO_2); (2) lack of volatile products after ligand-exchange reaction with various metal precursors (Fe_2O_3); and (3) absence of fluoride with the same oxidation state as the initial metal oxide (CrO_3). All of these metal oxides have volatile chlorides or oxychlorides and should be converted to B_2O_3 using BCl_3 based on thermochemical calculations. SnO_2, Ga_2O_3, ZrO_2 and HfO_2 ALE are possible using fluorination and ligand-exchange reactions.[57, 87] These metal oxides are included in Table 1 because they have volatile chlorides or oxychlorides and could be etched using the "conversion-fluorination" mechanism as an alternative.

Table 4-1. Thermochemistry of a Variety of Conversion Reactions for Various Metal Oxides

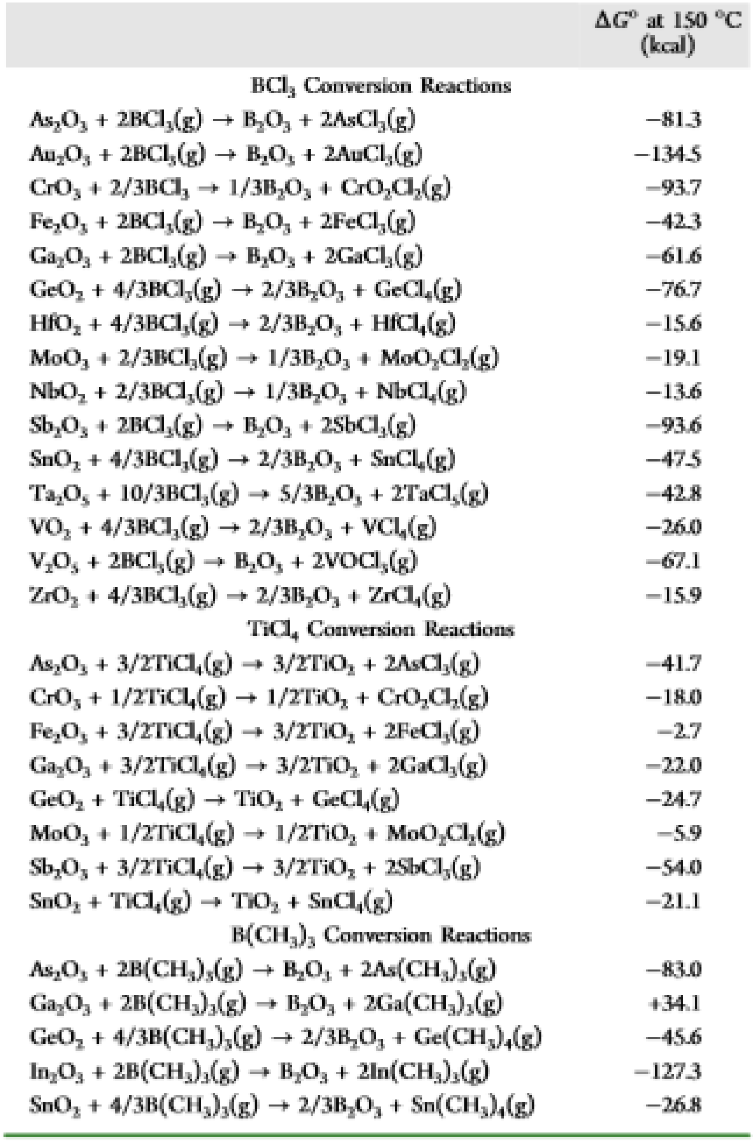

	ΔG° at 150 °C (kcal)
BCl_3 Conversion Reactions	
$As_2O_3 + 2BCl_3(g) \rightarrow B_2O_3 + 2AsCl_3(g)$	−81.3
$Au_2O_3 + 2BCl_3(g) \rightarrow B_2O_3 + 2AuCl_3(g)$	−134.5
$CrO_3 + 2/3BCl_3 \rightarrow 1/3B_2O_3 + CrO_2Cl_2(g)$	−93.7
$Fe_2O_3 + 2BCl_3(g) \rightarrow B_2O_3 + 2FeCl_3(g)$	−42.3
$Ga_2O_3 + 2BCl_3(g) \rightarrow B_2O_3 + 2GaCl_3(g)$	−61.6
$GeO_2 + 4/3BCl_3(g) \rightarrow 2/3B_2O_3 + GeCl_4(g)$	−76.7
$HfO_2 + 4/3BCl_3(g) \rightarrow 2/3B_2O_3 + HfCl_4(g)$	−15.6
$MoO_3 + 2/3BCl_3(g) \rightarrow 1/3B_2O_3 + MoO_2Cl_2(g)$	−19.1
$NbO_2 + 2/3BCl_3(g) \rightarrow 1/3B_2O_3 + NbCl_4(g)$	−13.6
$Sb_2O_3 + 2BCl_3(g) \rightarrow B_2O_3 + 2SbCl_3(g)$	−93.6
$SnO_2 + 4/3BCl_3(g) \rightarrow 2/3B_2O_3 + SnCl_4(g)$	−47.5
$Ta_2O_5 + 10/3BCl_3(g) \rightarrow 5/3B_2O_3 + 2TaCl_5(g)$	−42.8
$VO_2 + 4/3BCl_3(g) \rightarrow 2/3B_2O_3 + VCl_4(g)$	−26.0
$V_2O_5 + 2BCl_3(g) \rightarrow B_2O_3 + 2VOCl_3(g)$	−67.1
$ZrO_2 + 4/3BCl_3(g) \rightarrow 2/3B_2O_3 + ZrCl_4(g)$	−15.9
$TiCl_4$ Conversion Reactions	
$As_2O_3 + 3/2TiCl_4(g) \rightarrow 3/2TiO_2 + 2AsCl_3(g)$	−41.7
$CrO_3 + 1/2TiCl_4(g) \rightarrow 1/2TiO_2 + CrO_2Cl_2(g)$	−18.0
$Fe_2O_3 + 3/2TiCl_4(g) \rightarrow 3/2TiO_2 + 2FeCl_3(g)$	−2.7
$Ga_2O_3 + 3/2TiCl_4(g) \rightarrow 3/2TiO_2 + 2GaCl_3(g)$	−22.0
$GeO_2 + TiCl_4(g) \rightarrow TiO_2 + GeCl_4(g)$	−24.7
$MoO_3 + 1/2TiCl_4(g) \rightarrow 1/2TiO_2 + MoO_2Cl_2(g)$	−5.9
$Sb_2O_3 + 3/2TiCl_4(g) \rightarrow 3/2TiO_2 + 2SbCl_3(g)$	−54.0
$SnO_2 + TiCl_4(g) \rightarrow TiO_2 + SnCl_4(g)$	−21.1
$B(CH_3)_3$ Conversion Reactions	
$As_2O_3 + 2B(CH_3)_3(g) \rightarrow B_2O_3 + 2As(CH_3)_3(g)$	−83.0
$Ga_2O_3 + 2B(CH_3)_3(g) \rightarrow B_2O_3 + 2Ga(CH_3)_3(g)$	+34.1
$GeO_2 + 4/3B(CH_3)_3(g) \rightarrow 2/3B_2O_3 + Ge(CH_3)_4(g)$	−45.6
$In_2O_3 + 2B(CH_3)_3(g) \rightarrow B_2O_3 + 2In(CH_3)_3(g)$	−127.3
$SnO_2 + 4/3B(CH_3)_3(g) \rightarrow 2/3B_2O_3 + Sn(CH_3)_4(g)$	−26.8

4.3.3.2 Conversion Etch with $TiCl_4$

The conversion of metal oxides to other metal oxides besides B_2O_3 is also possible. One possibility is the conversion of metal oxides to TiO_2 using $TiCl_4$. Fluorination of TiO_2 using HF exposures would then spontaneously etch TiO_2 by producing volatile TiF_4 and H_2O reaction products.[130] $TiCl_4$ may not be as useful as BCl_3 for conversion etch. The thermochemistry of conversion of metal oxides to TiO_2 using $TiCl_4$ is not as favorable as the thermochemistry of conversion of metal oxides to B_2O_3 using BCl_3. However, the conversion of the surface of a metal oxide to a TiO_2 surface layer may be useful for device applications to avoid a TiO_2 ALD processing step.

4.3.3.3 Conversion Etch Ligand Effects and Selectivity

The thermochemistry of most of these reactions in Table 1 is favorable as measured by the standard free energy changes. The examples in Table 1 use either BCl_3 or $B(CH_3)_3$ for the conversion reaction to form B_2O_3. The choice of BCl_3 or $B(CH_3)_3$ depends on the volatility of the reaction products. In addition, the ligand on the boron center can also lead to selective ALE.[87] The thermochemical calculations reveal that Ga_2O_3 cannot be converted to B_2O_3 using $B(CH_3)_3$. Consequently, $B(CH_3)_3$ could be used to etch In_2O_3, GeO_2, As_2O_3 and SnO_2 without etching Ga_2O_3.

4.4 Conclusions

The thermal ALE of WO_3 and W were demonstrated with new etching procedures using “conversion-fluorination” and “oxidation-conversion-fluorination” mechanisms. These procedures are important because earlier thermal ALE processes have utilized fluorination and ligand-exchange reactions that require the formation of a stable metal fluoride. In contrast, the new mechanisms are applicable for metal materials with volatile metal fluorides. Some elemental metals also require initial oxidation reactions because fluorination is very robust and leads to fluoride layers too thick for ALE.

The "conversion-fluorination" mechanism using an AB exposure sequence with BCl_3 and HF as the reactants was employed for WO_3 ALE. BCl_3 converts the WO_3 surface to a B_2O_3 layer and is believed to form volatile WO_2Cl_2 as a reaction product. The B_2O_3 layer is then spontaneously etched by HF to produce volatile BF_3 and H_2O. The BCl_3 and HF reactions were both self-limiting versus exposure. The WO_3 ALE etch rates were temperature dependent and increased from 0.55 Å/cycle at 128°C to 4.19 Å/cycle at 207°C. The W film acted as an etch stop because BCl_3 and HF could not etch the underlying W film.

The "oxidation-conversion-fluorination" mechanism using an ABC exposure sequence with O_2/O_3, BCl_3 and HF as the reactants was employed for W ALE. O_2/O_3 first oxidizes the W surface to a WO_3 layer. The WO_3 layer is then etched with BCl_3 and HF. The SE measurements could monitor simultaneously the W and WO_3 thicknesses during W ALE. The WO_3 thickness is oscillatory and increases during W oxidation and decreases during WO_3 etching. Concurrently, the W film thickness decreased linearly with number of ABC reaction cycles. W ALE was self-limiting with respect to each reaction in the ABC process. The etch rate for W ALE was ~2.5 Å/cycle at 207°C. The residual WO_3 thickness of ~20 Å after W ALE could be removed with BCl_3 and HF reaction cycles without affecting the W layer.

These new etching mechanisms based on "conversion-fluorination" and "oxidation-conversion-fluorination" should be useful for the thermal ALE of a variety of materials. The conversion and fluorination reactions using BCl_3 and HF can be applied to many metal oxide materials including the oxides of W, V, Nb, Ta, Cr, Mo, Fe, Au, Ga, Ge, Sn, As, Sb, Zr and Hf. The metals in these metal oxides can be converted to B_2O_3 by BCl_3 and have metal chlorides and metal oxychlorides that are volatile. The new "conversion-fluorination" and "oxidation-conversion-fluorination" mechanisms will be particularly valuable for providing ALE pathways for metals and metal oxides that have volatile metal fluorides.

4.5 Aknowledgements

This research was funded by the Semiconductor Research Corporation. The authors thank Jonas Gertsch for depositing the initial W ALD films on the silicon wafers. The authors also acknowledge Advanced Energy in Fort Collins, Colorado, for the RF power supply and the impedance matching network for the ICP plasma source. In addition, the authors are grateful to Dr. Satyarth Suri of Intel Corporation for many useful discussions.

Chapter 5

Thermal Atomic Layer Etching of Ta2O5 and TaN by "Conversion-Etch" and "Oxidation-Conversion-Etch

5.1 Introduction

The concept of Moore's law has been a result of the drive to continue to increase the number of transistors per unit area.[9] The increase of transistors per unit area has relied on etching techniques to precisely remove material at dimensions that are becoming increasingly smaller with more complicated 3D geometries.[11, 14, 17, 55] Devices that are now approaching 5 and 7 nm nodes require precision in the removal of material for proper device function.[55]

Thermal Atomic layer etching (ALE) is a new method based upon sequential thermal reactions for precise removal of material at the atomic scale. The future of semiconductor manufacturing needs ALE to help with the miniaturization of devices.[11, 55] The concept of ALE has, in general, been thought of as a plasma process only. Literature searches of ALE give plasma etching of compounds such as SiO_2[131], W[132], Ge, GaAs[133], graphene[134] and InP[81] . Though very useful for etching in the semiconductor manufacturing, plasmas have issues with high aspect ratio structures , and can lead to surface damage[135].

Thermal ALE is a relatively new field of isotropic etching. This type of ALE proceeds first by a surface modification to an appropriate oxidation state followed by a reactant that removes the modified surface. Thermal ALE has been demonstrated this way by two different methods: Ligand-exchange and conversion etch. Ligand-exchange ALE has been demonstrated with HF and Sn(acac) 2 on AlN[136], Al_2O_3[35] , HfO_2[38] , and AlF_3[37] . The conversion etch method is useful where the initial modification of the surface to the correct oxidation state creates volatile compounds, however this is not always necessary. Conversion etch has been shown by HF and TMA on ZnO_2[137], SiO_2[138] and BCl_3 on W[139] and WO_3[139].

Tantalum oxide stacks in a memory cell were shown to be excellent candidates in high-density and high-speed non-volatile memory due to its charge trapping abilities.[140] HfO_2-Ta_2O_5-HfO_2 stacks were shown to outperform conventional Oxide-nitride-oxide memory stacks[141]. Amorphous Ta_2O_5 is used as a copper diffusion barrier.[142-143] Ta_2O_5 can be used as a dielectric material for organic thin film transistors[144] TaN is a conductive nitride which is used as a gate metal in NMOS devices[145] and memory devices[141]. TaN is an excellent diffusion barrier between copper and silicon.[146]

Etching techniques for Ta_2O_5 and TaN have been widely demonstrated in literature. Unwanted etching of tantalum oxide was seen by halogenated TaX_5 compounds and water at high temperatures, alluding to other ALE methods of Ta_2O_5 using metal halogen complexes.[147-148] Halogen containing plasmas such as NF_3, CF_4 and mixtures of SF_6 and Cl_2 can be used to etch Ta_2O_5 and Ta_2N.[149-152]Other carbon halogen plasmas such as CF_3Cl, CHF_3 can be used to etch Ta_2O_5[153-154]. TaN_x compounds can be etched from a gas mixtures of $SiCl_4$-NF_3[155], Cl_2-HBr[156] and Cl_2-SF_6-Ar[157]. BCl_3 plasmas were aslo used to etch TaN compounds.[158-160]

This work demonstrates thermal ALE utilizing conversion-etch reactions and oxidation-etch reactions. Gaseous BCl_3 was used as the conversion reactant. BCl_3 can be used convert many oxides to its stable B_2O_3.[139] Ta_2O_5 is thermodynamically favorable to be converted to B_2O_3 while forming volatile $TaCl_5$ as shown in equation 1.

(1) $Ta_2O_5 + 10/3\ BCl_3(g) \rightarrow 5/3\ B_2O_3 + 2TaCl_5(g)$ ΔG at 250°C: -37.18 kcal

B_2O_3 can then be removed spontaneously by formation of its volatile fluoride BF_3 through interaction with HF as shown in previous work[139]. The thermodynamics of the reaction is shown in reaction 2.

(2) $B_2O_3 + 6HF(g) \rightarrow 2BF_3(g) + 3H_2O(g)$ ΔG at 250: -16.87 kcal

HF from a HF-Pyridine solution was the fluorination source and spontaneous etch reactant. Ta_2O_5 ALE is demonstrated and investigations into the pathway using BCl_3 and HF are conducted in this paper. TaN ALE is shown through an oxidation-etch process, where TaN is oxidized and the oxide is then removed by BCl_3 and HF.

5.2 Experimental

5.2.1 Ta_2O_5 and TaN Films

Ta_2O_5 samples were grown by ALD on Si wafers with a native oxide. Ta_2O_5 films were grown at 190 ^oC by tert-butylimido-tris-ethylmethylamido-tantalum (TBTEMAT, Strem 99.99%) and H_2O. Thicknesses of Ta_2O_5 films were 340 Å for all experiments except XRR analysis where the film was 700 Å. TaN films were deposited on Si wafers with a 500 nm thermal oxide. TaN films were grown at 200 ^oC in a separate hot walled viscous reactor with tert-butylimido-tris-ethylamido-tantalum (TBTEAT Strem, 99.99%) and N_2H_4 (Rasirc) to a thickness of 250Å. TaN films were then exposed to air after cooling down room temperature.

5.2.2 Samples, Precursors and Dosing Parameters

A native oxide thickness of 10-16 Å formed on TaN samples when exposed to atmosphere upon transfer between reactors. Si wafers with Ta_2O_5 and TaN were diced into squares with dimensions of 16 x 16 mm. The square coupons were then set onto a 304 stainless steel sample holder and placed into a reaction chamber that has been described previously.[161] Samples were heated on the sample stage to a temperature of 250 ^oC. The reactor walls were heated to 170 ^oC and were coated with 500 cycles Alumina ALD using trimethyl aluminum and H_2O. HF-pyridine (70 wt. % HF, Sigma Aldrich) and BCl_3 (99.9%, Synquest Laboratories) were used as the reactants. Reactants were separately dosed into the reaction chamber into 120 mTorr of ultra high purity (UHP) N_2. Reactants were introduced by a pneumatic and needle valve setup described previously[139]. Between reactants exposures, the chamber was purged with 1270 mTorr of UHP N_2. For repeated exposures of BCl_3 a purge time of 30 seconds was used between doses, followed by a 70 second purge time before HF exposures. HF purge times were constant at 70 seconds. LabView was the program used for dosing and purging parameters.

5.2.3 Spectroscopic Ellipsometry

An *in-situ* M-2000 Ellipsometer with a 239.2-1687.2 nm spectral range was used for analysis of Ta_2O_5 and TaN films during ALE. Psi and Delta data was analyzed by Complete Ease software from J.A. Woollam. A Tauc-Lorentz model was used as the optical model for Ta_2O_5 films. Tauc-Lorentz parameters were fit to the Ta_2O_5 films and held constant for ALE experiments as the films exhibited bulk properties in the thickness range etched.

5.2.4 Ozone Generation

20% O_3 in O_2 by weight was the oxidizing source for TaN. Ozone cleaning was also conducted for Ta_2O_5 samples exposed to atmosphere for XRR analysis. O3ONIA ozone generator produced 20% O_2/O_3 from UHP oxygen (Airgas 99.999%). For TaN oxidation, an O_2/O_3 pressure of 120 mTorr was used. A temperature of 250 ^{o}C was used for all ozone experiments.

5.2.5 X-Ray Reflectivity

XRR analysis was performed ex-situ by a high resolution X-Ray diffractometer (Bede DI, Jordan Valley Semiconductors). Cu Kα radiation produced the X-rays(λ=1.540Å). In the X-ray tube, filament current was held at 35 mA with a voltage of 40 kV. A step size of 10 arcsec with an acquisition time of 10 seconds were conditions used for all XRR scans. XRR scans were fit with the Bede Refs analysis software (Jordan Vally Semiconductors) in order to determine thickness, density and surface roughness.

5.3 Results and Discussion

5.3.1 Ta_2O_5 ALE using BCl_3 and HF

5.3.1.1 Ta_2O_5 ALD

Ta_2O_5 films were grown by TBTEMAT and H_2O at 190 ^{o}C in an AB reactant sequence. The change in Ta_2O_5 thickness for 385 ALD cycles is shown in figure 1. Data points are shown every 10 cycles for clarity, except for the last point which is 5 cycles from the previous. There is nucleation period for this ALD process which agrees with literature.[162] Growth is linear with an etch rate of 1.0 Å/cycle. These ALD films are amorphous

5.3.1.2 Ta_2O_5 ALE with BCl_3/HF at 250ºC

In Situ SE measurements of the Ta_2O_5 film thickness during etching cycles are shown in figure 2. Figure 2 exhibits etching of a Ta_2O_5 film at 250ºC for 100 cycles. SE measurements were obtained through an AB exposure sequence with BCl_3 and HF as the reactants. Data points are shown every 5 cycles for clarity. Linear etching is observed with an R^2 value of 0.99 and an etch rate is 1.05 Å/cycle. Etch rates for Ta_2O_5 ALE at 250 ºC varied from 0.96 to 1.09 Å/cycle. Conditions used were 3 consecutive 30 second static exposures of 130 mTorr BCl_3 followed by a viscous 0.25 second HF dose of 120 mTorr. After each reactant dose, the chamber was purged in UHP N_2.

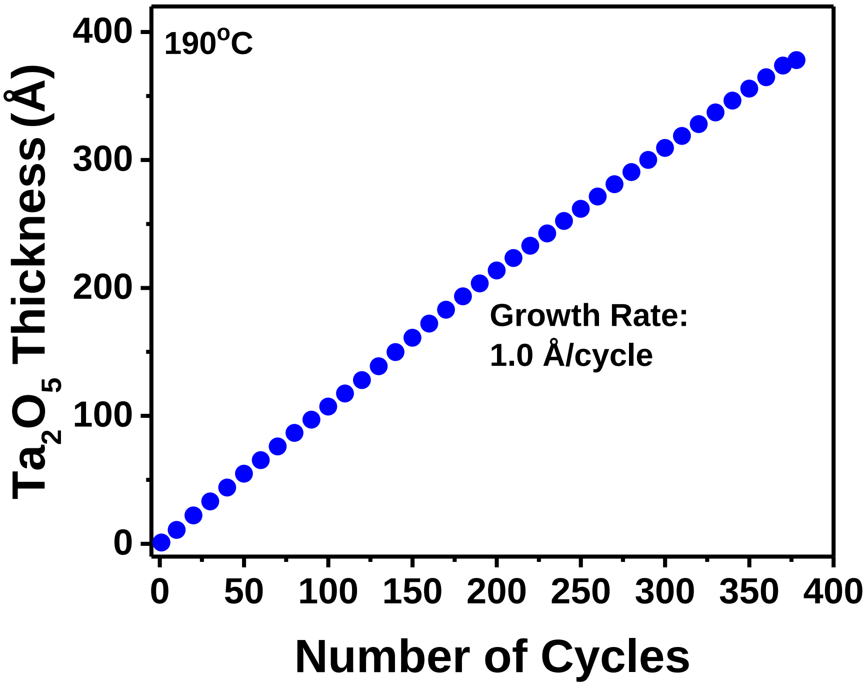

Figure 5-1. Ta_2O_5 thickness versus number of ALD cycles using TBTEMAT and H_2O at 190 °C. Ta_2O_5 ALD has a growth rate of 1.0 Å/cycle

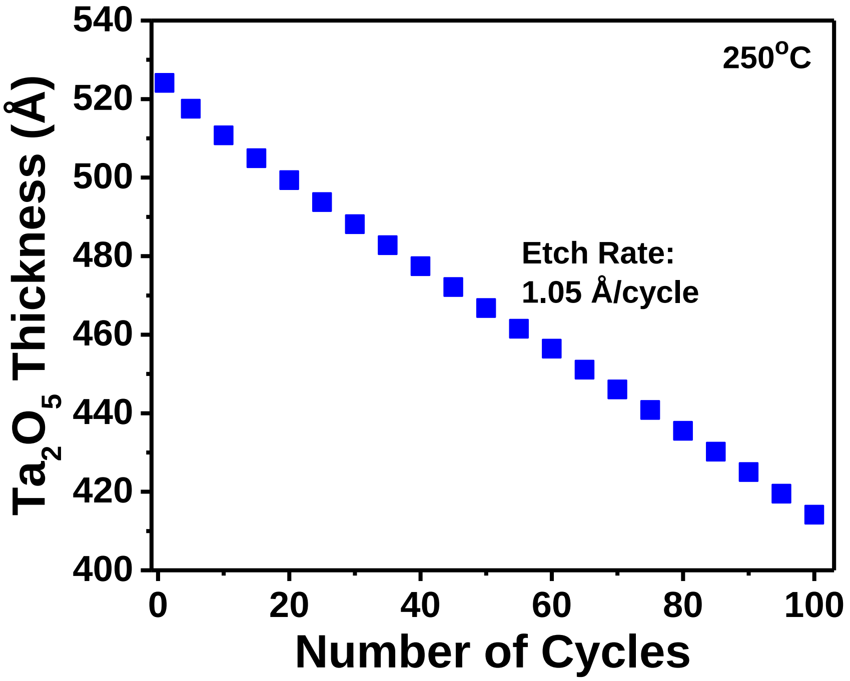

Figure 5-2. Ta_2O_5 thickness versus number of cycles during Ta_2O_5 ALE with BCl_3 and HF at 250 ^oC. Etch rate during Ta_2O_5 ALE is 1.05 Å/cycle.

XRR measurements were collected ex situ to corroborate thickness measurements for SE. Figure 3 shows Ta_2O_5 thickness vs number of ALE cycles. SE measurements were carried out *in situ* through all 400 ALE cycles. XRR measurements were taken ex situ for initial thickness and thickness measurements after 100, 200 and 400 ALE cycles. After each exposure to atmosphere, samples were cleaned at 250 ^{o}C with O_2/O_3. There is good thickness agreement between XRR and SE. Thickness measurements for XRR after 0, 100, 200, 400 ALE cycles were 691.3, 593.6, 493.0 and 288.5 Å. SE measurements after 0, 100, 200, 400 ALE cycles were 707.6, 612.7, 515.04, and 319.6 Å, respectively.

5.3.1.3 Self-Limiting Conditions

Figure 4. examines the self-limiting nature of BCl_3 and HF reactions on Ta_2O_5 ALE. ALE rates were determined by holding one reactant exposure constant and varying the other. Between HF and BCl_3 reactant exposures, the chamber was purged with UHP nitrogen at a background pressure of 1260 mTorr. Figure 3a. analyzes the effect of BCl_3 reactant exposure on the Ta_2O_5 etch rate at 250^{o}C. Consecutive BCl_3 exposures were held statically for 30 seconds with pressure transients of 130 mTorr. Viscous HF doses were held at a dosing time of 0.25 seconds with pressure transients of 120 mTorr. Unlike an ALD process, the etch rate has no self-limiting BCl_3 exposure. Etch rate vs exposure follows a diffusion like curve similar to Deal-Grove Kinetics for oxidation[125]. This diffusion like condition is likely a result of boron and/or chlorine intercalation into the film. An increase in exposure results in a larger modified layer thickness that can be spontaneously removed through exposure to HF.

Figure 4b depicts the effect of varying HF exposures on the Ta_2O_5 etch rate. BCl_3 was held at 3 consecutive 30 second static doses at 130 mTorr. One exposure of HF at 120 mTorr reaches saturation and produces an average etch rate of 1.03 Å. Under these conditions etch rates ranged from 0.95 to 1.09. Consecutive HF exposures do not increase the etch rate of Ta_2O_5 ALE. HF is self-limiting because the etch is constrained to the thickness of the modified Ta_2O_5 layer. This is a result from no etching occurring during interaction of Ta_2O_5 with HF alone.

5.3.1.4 Roughness Measurements During Ta_2O_5 ALE

XRR was employed to see if roughening or smoothening of the surface occurred during Ta_2O_5 ALE. XRR scans of the initial film and 100, 200, and 400 ALE cycles are shown in figure 5. 3 consecutive 30 second BCl_3 doses at 130 mTorr and a 0.25 second 120 mTorr viscous HF dose were the conditions used. Initial Ta_2O_5 films had a roughness of 8.68Å. Roughness of the films were decreased with increasing number of ALE cycles. Roughness of 0, 100, 200, and 400 ALE cycles were 8.68, 8.41, 8.16 and 7.26Å, respectively. The decrease of roughness for Ta_2O_5 is consistent with Thermal ALE of TiN[163], Al_2O_3[35] and HfO_2[38].

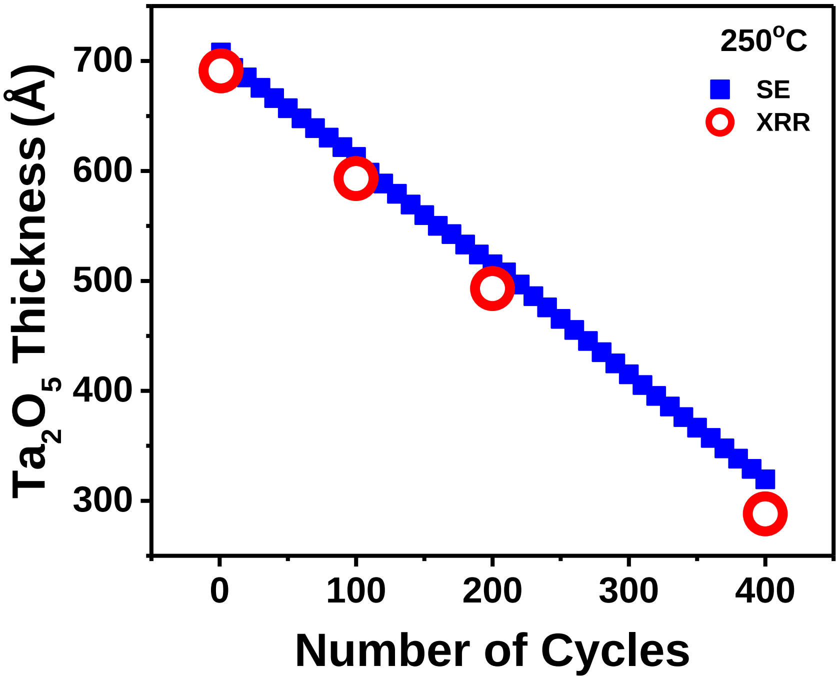

Figure 5-3. Spectroscopic ellipsometry and X-ray reflectivity measurements of Ta_2O_5 film thickness versus number of ALE cycles. SE measurements are shown every 10 cycles for clarity. XRR measurements are after 0, 100, 200, and 400 ALE cycles.

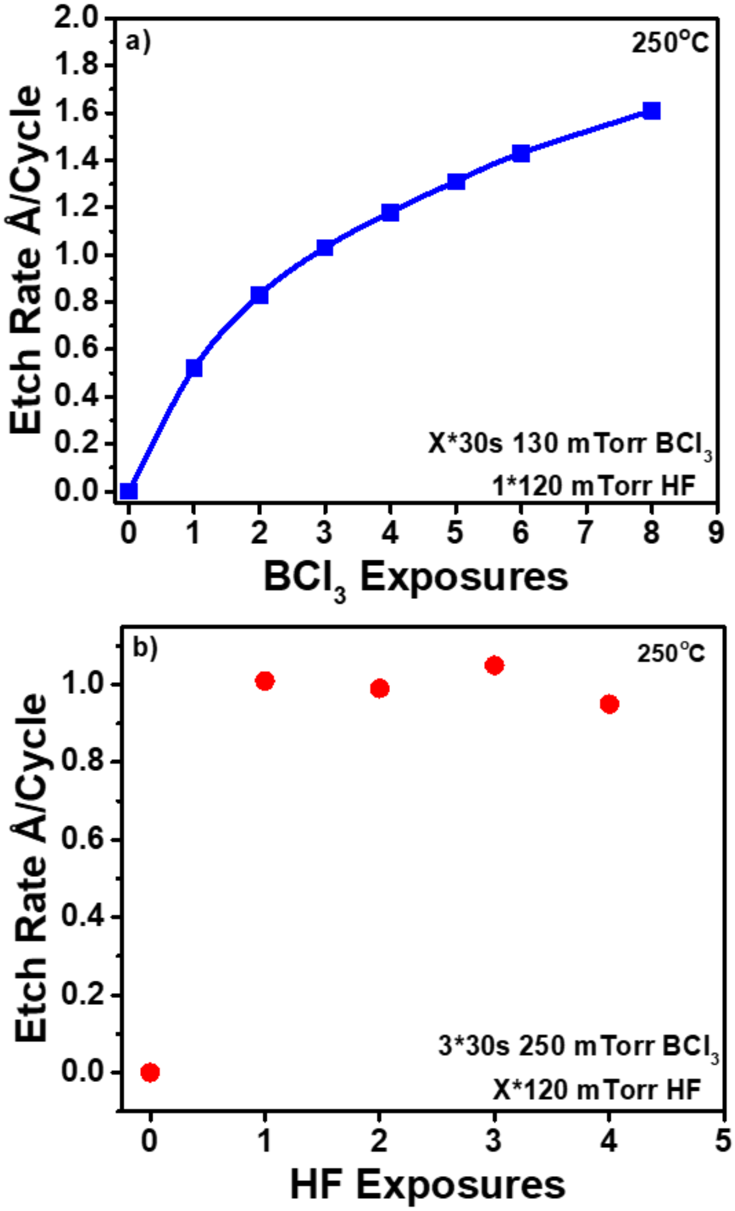

Figure 5-4. Ta_2O_5 etch rate versus reactant exposure during Ta_2O_5 ALE at 250 °C. (a) BCl_3 exposure were varied while HF dosing was held constant at 120 mTorr for 0.25 seconds. (b) HF exposures were varied while BCl_3 exposures were held constant at 3 consecutive 30 seconds 130 mTorr doses.

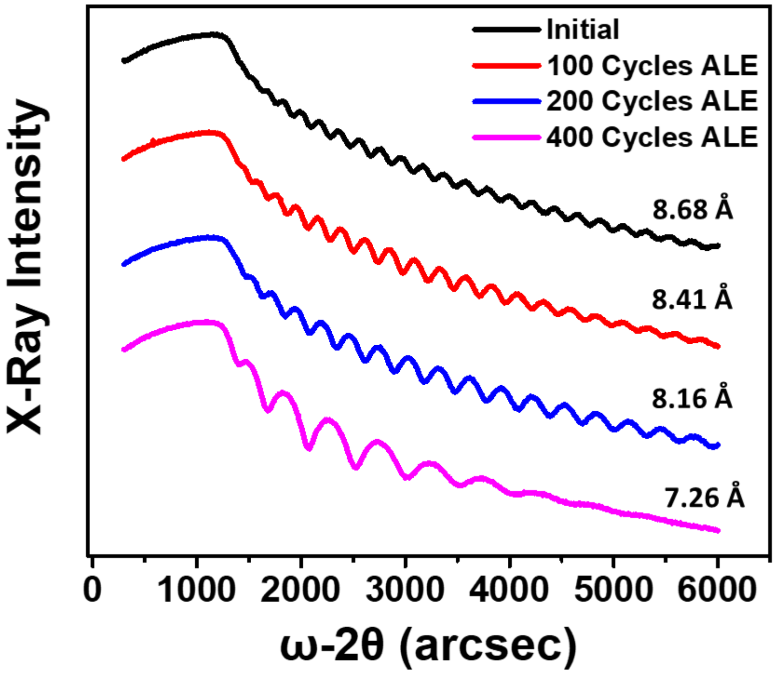

Figure 5-5. XRR spectra of Ta_2O_5 films before and after ALE. (a) The initial Ta_2O_5 films thickness of 700 Å. Ta_2O_5 films were etch for (b) 100 cycles (c) 200 cycles and (d) 400 ALE cycles. Roughness measurements were (a) 8.68 Å, (b) 8.41 Å, (c) 8.16 Å and (d) 7.26 Å showing film smoothening during ALE.

5.3.1.5 Temperature Dependence of Ta_2O_5 ALE

The Ta_2O_5 thickness versus cycle number for a variety of temperatures is shown in figure 6. 3 consecutive 30 second BCl_3 doses at 120 mTorr with one viscous 0.25 second 120 mTorr HF dose were the conditions used for each temperature. All temperatures initial thickness was normalized to 340 Å to show the difference of temperature on the etch rate. The etching of Ta_2O_5 is linear throughout the temperature range. Etching increases with increasing temperature. The etch rates of 0.36, 0.65, 1.08, 1.30, and 1.96 Å/cycle are for 200, 225, 250, 275, and 295 ^{o}C, respectively.

5.3.1.6 Arrhenius Plot of Temperature Dependence

An Arrhenius plot of the natural log of the Ta_2O_5 etch rate versus 1000/T is shown in figure 7. The linear graph of the ln(etch rate) versus 1000/T shows that the etch rate is exponentially dependent on the temperature. The activation energy for Ta_2O_5 ALE is 8.7 kcal/mol. The etch rate can be controlled by a temperature change for Ta_2O_5 ALE

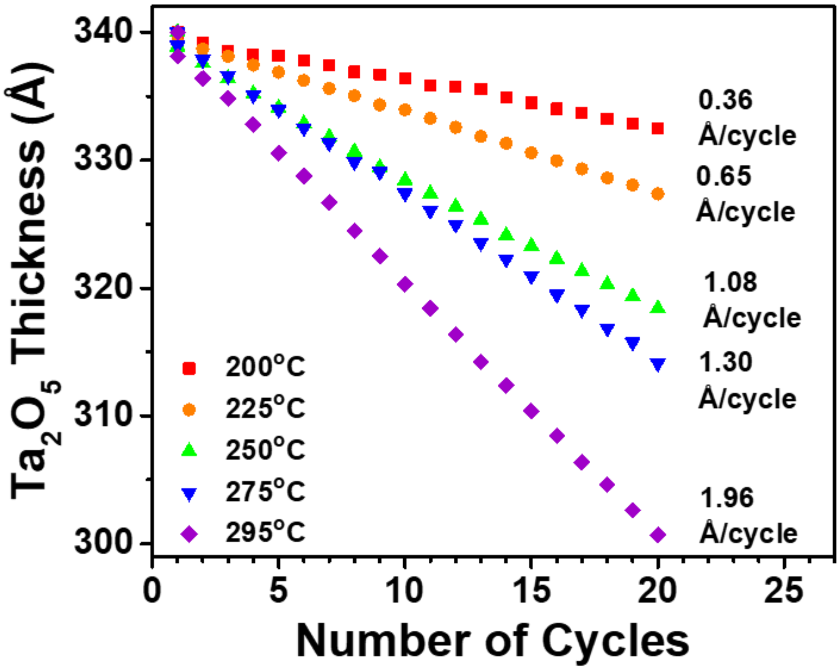

Figure 5-6. Ta_2O_5 thickness versus number of ALE cycles at 200, 225, 250, 275, and 295 °C.

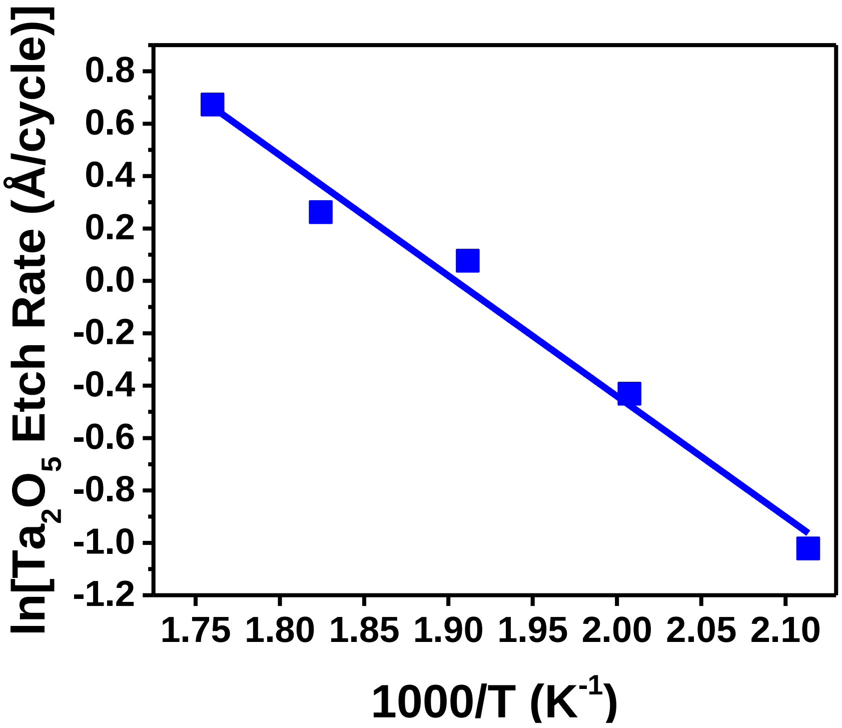

Figure 5-7. Arrhenius plot of the etch rates temperature dependence for Ta_2O_5 ALE. Slope of the Arrhenius plot yields and activation energy of 8.7 kcal/mol.

5.3.2 Pressure Dependence of Ta_2O_5 ALE

5.3.2.1 BCl_3 Pressure Dependence

Results from the investigation of BCl_3 exposure on the etch rate led to the conclusion that the BCl_3 effect on Ta_2O_5 ALE is exposure dependent. Therefore, increasing pressures should result in an etch rate increase. The result of varying BCl_3 pressures on the etch rate versus number of cycles is shown in figure 8. A single 30 second BCl_3 dose with varying BCl_3 pressure transients along with one visous 0.25 second 120 mTorr viscous HF dose, were the conditions used. Linear etching is observed regardless of BCl_3 pressure chosen. An increase in BCl_3 pressure results in an increase in the etch rate, alluding to a diffusion barrier on the etch rate. Similar experiments increasing HF pressure showed no pressure dependence on the etch rate for that reaction. With pressures of 130, 250, 500 and 1000 mTorr pressures, etch rates of 0.48, 0.56, 0.86, and 1.46 Å/cycle were observed. The pressure dependence allows for much higher etch rates to be achieved.

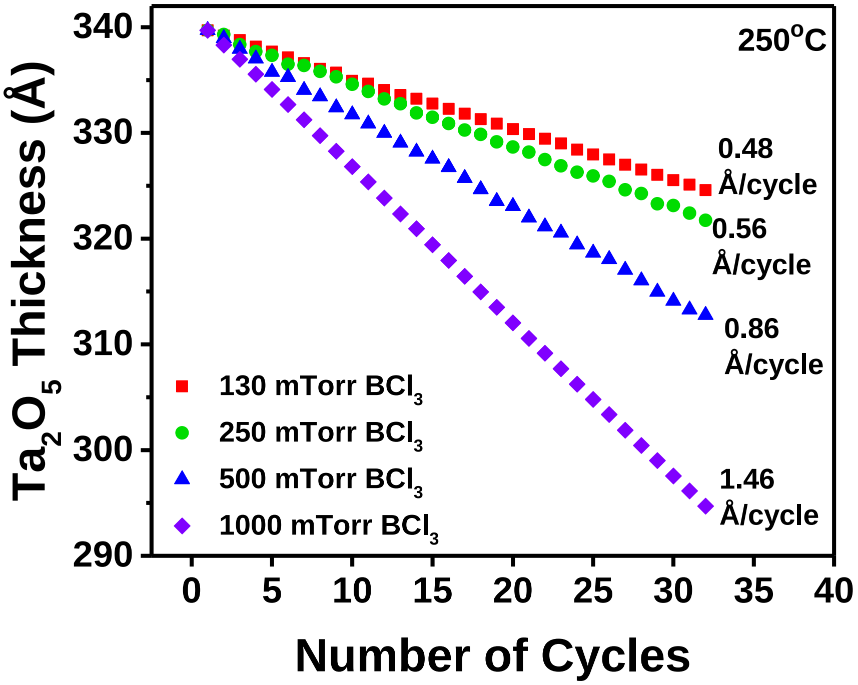

Figure 5-8. Thickness change of Ta_2O_5 versus number of ALE cycles for varying BCl_3 pressures of 130, 250, 500, and 1000 mTorr BCl_3. HF doses were held constant throughout all pressure experiments.

5.3.2.2 Pressure Dependent Self-Limiting Studies

Figure 9 investigates the self-limiting nature using different BCl_3 pressures at 250 ^oC with HF conditions from figure 6b. Figure 9a shows the comparison of 130 and 250 mTorr consecutive BCl_3 exposures on the etch rate. As expected, the increase in BCl_3 pressure results in a higher etch rate. The higher BCl_3 pressures result in a difference exposure dependence curve. 3 consecutive 30 second doses of 250 mTorr BCl_3 resulted in an etch rate of 1.59 Å/cycle as opposed to 1.03 Å/cycle with 130 mTorr BCl_3. 2 HF doses at 120 mTorr were used for all higher BCl_3 pressure studies to ensure removal of the modified Ta_2O_5 surface. The increase of etch rate allows for conditionally dependent etch rates. Figure 9b shows the self-limiting nature of HF exposures with varying BCl_3 pressures using 3 consecutive 30 second static exposures. As with lower pressures of BCl_3, HF is self-limiting, however, it takes 2 120 mTorr doses to reach complete removal of the modified surface on Ta_2O_5.

5.3.2.3 Ta_2O_5 ALE at 250^{o}C using 250 mTorr BCl_3

Figure 10 shows the change of Ta_2O_5 thickness versus cycle number for BCl_3 pressures of 250 mTorr at 250 ^oC. 3 consecutive 30 second static 250 mTorr BCl_3 exposures with 2 consecutive 0.25 second 120 mTorr HF doses were the reaction conditions. The etching is linear with an R^2 value of 0.99 as with figure 10, however, the etch rate is higher at 1.59Å/cycle. Regardless of the pressure used, the etching is linear. This allows for the user to pick the conditions and concurrently the rate that Ta_2O_5 will etch. This diffusion dependence should be applicable to other conversion etch systems.

5.3.2.4 Pathway Determination

The anticipated interaction of BCl_3 with Ta_2O_5 should form a volatile $TaCl_5$ complex and a non-volatile B_2O_3 layer. This is similar to WO_3 etching with BCl_3 and HF. The reaction pathways that Ta_2O_5 may undertake to form $TaCl_5$ is shown in equations 1 respective Gibbs energy. A thickness loss of 1.05Å per cycle for Ta_2O_5 produces $1.91E^{-10}$ mol/cm^2 of Ta_2O_5 set by a Ta_2O_5 density of 8.2 g/cm^3 and a molar mass of 441.89 g/mol. Based on equations 1 and the etch rate in moles, the formation of B_2O_3 should have a thickness of 0.90 Å using a B_2O_3 density of 2.46 g/cm^3 and a molar mass of 69.61 g.mol. Ellipsometry can be used to measure the thickness changes after each reaction cycle.

Ellipsometry measurements that were taken after each BCl_3 and HF reactions are shown in figure 11. With a Ta_2O_5 etch rate of 1.05Å, and a predicted B_2O_3 thickness of 0.90 Å after Ta_2O_5 removal, there must be a thickness decrease for Ta_2O_5 ALE to proceed through eq 1. Figure 3 shows an increase in thickness after BCl_3 reacts with the Ta_2O_5 surface. This information shows that Ta_2O_5 ALE does not proceed through eq 1. The thickness increase is likely a result of boron and chlorine intercalation into the film. Although the pathway for etching is not as anticipated, the interaction of the modified surface with HF results in etching. The volatile species removed from the surface is unknown but could be a $TaO_wCl_xF_yB_z$ complex. Future mass spectrometry experiments will deduce the volatile compounds

Using the information from figure 11, the Ta_2O_5 ALE process is shown in figure 12. Upon initial interaction of the Ta_2O_5 surface, Boron and chlorine intercalate into the film resulting in a thickness expansion. This forms a $TaO_xCl_yB_z$ complex. This complex can then be etched spontaneously by HF forming an unknown compound. Conversion of Ta_2O_5 is needed as Ta_2O_5 is not etched by HF alone and stronger fluorination sources result in spontaneous etching.

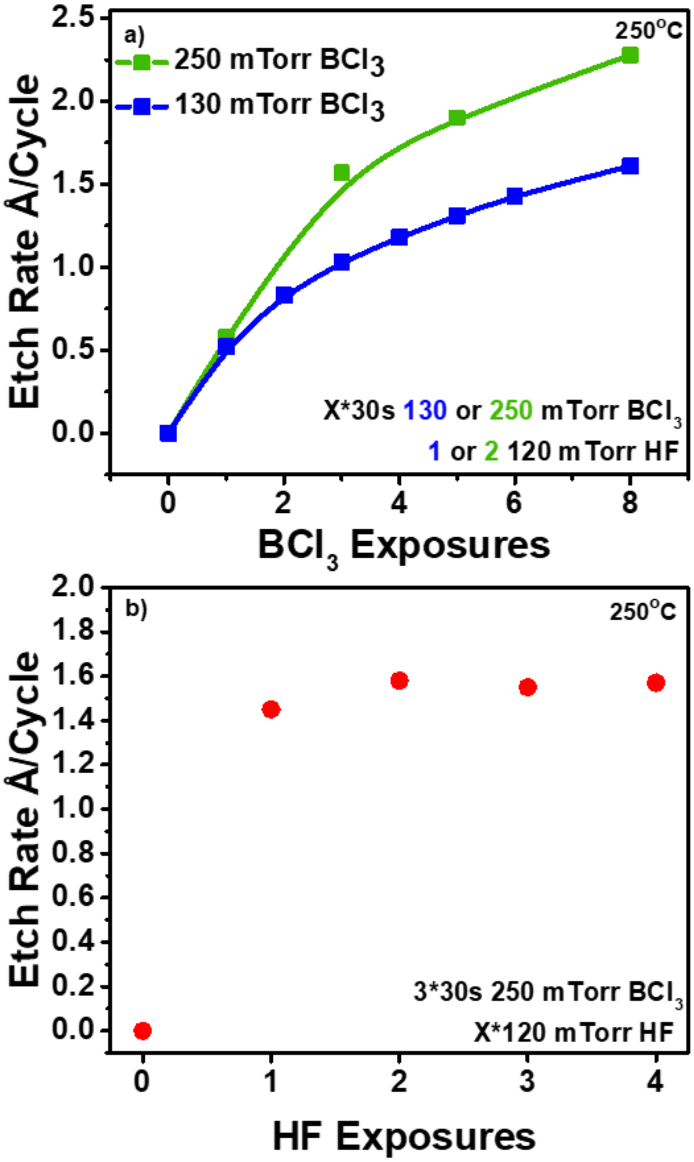

Figure 5-9. Pressure dependent self-limiting curves of Ta_2O_5 ALE. (a) Comparison of BCl_3 curves using 130 mTorr (blue) and 250 mTorr (green) while HF dosing was held constant at 0.25 s and 120 mTorr (b) HF exposure was varied while BCl_3 exposures were held constant at 3 consecutive 30 second 250 mTorr doses.

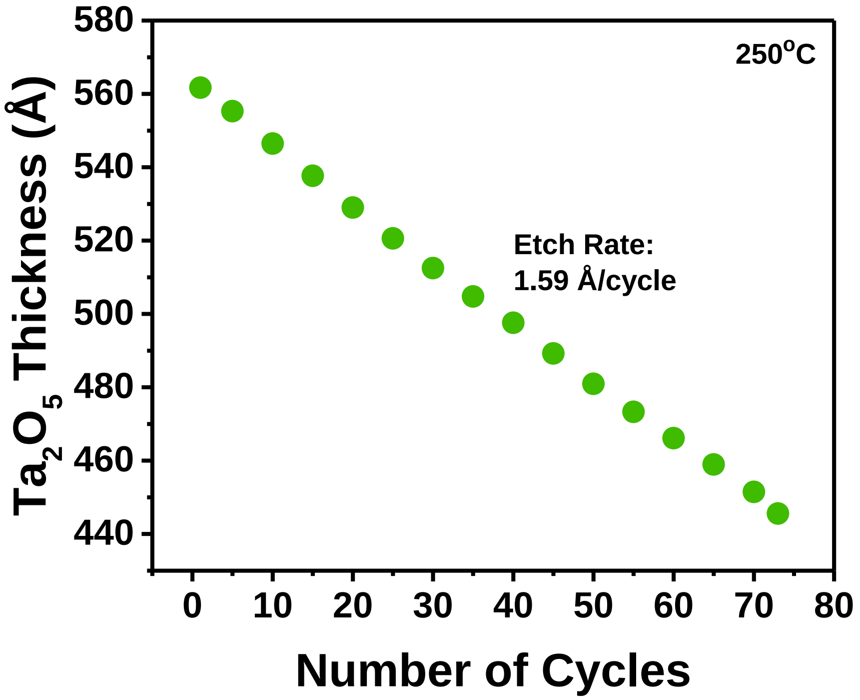

Figure 5-10. Ta_2O_5 thickness change versus number of ALE cycles using 3 consecutive 30 second BCl_3 exposures at 250 mTorr and HF at 2 consecutive 0.25 second 120 mTorr doses. Etch rate during Ta_2O_5 ALE with higher BCl_3 pressures is 1.59 Å/cycle.

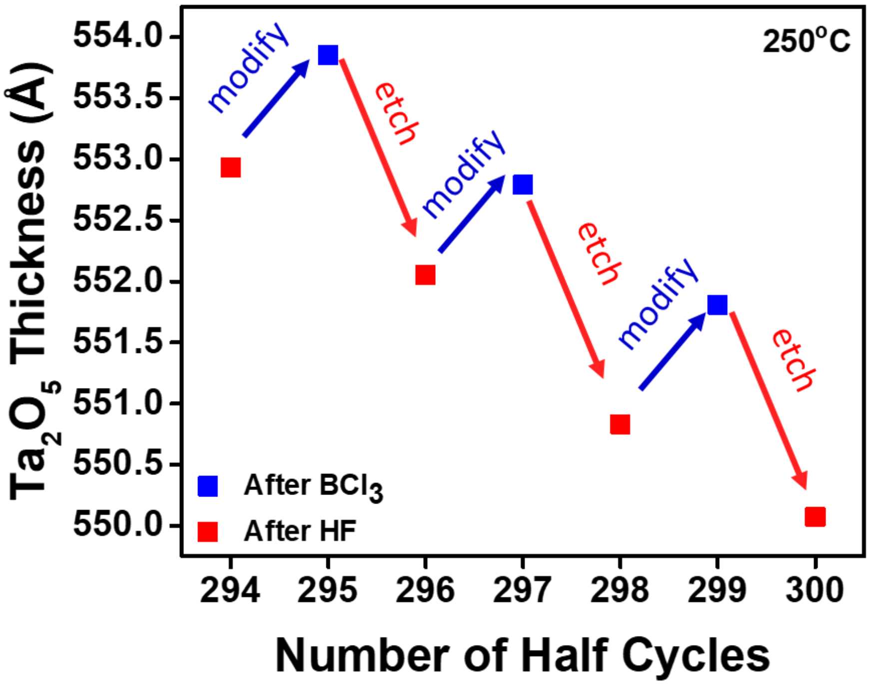

Figure 5-11. Ta_2O_5 thickness versus number of half-cycles during Ta_2O_5 ALE at 250 °C under self-limiting conditions.

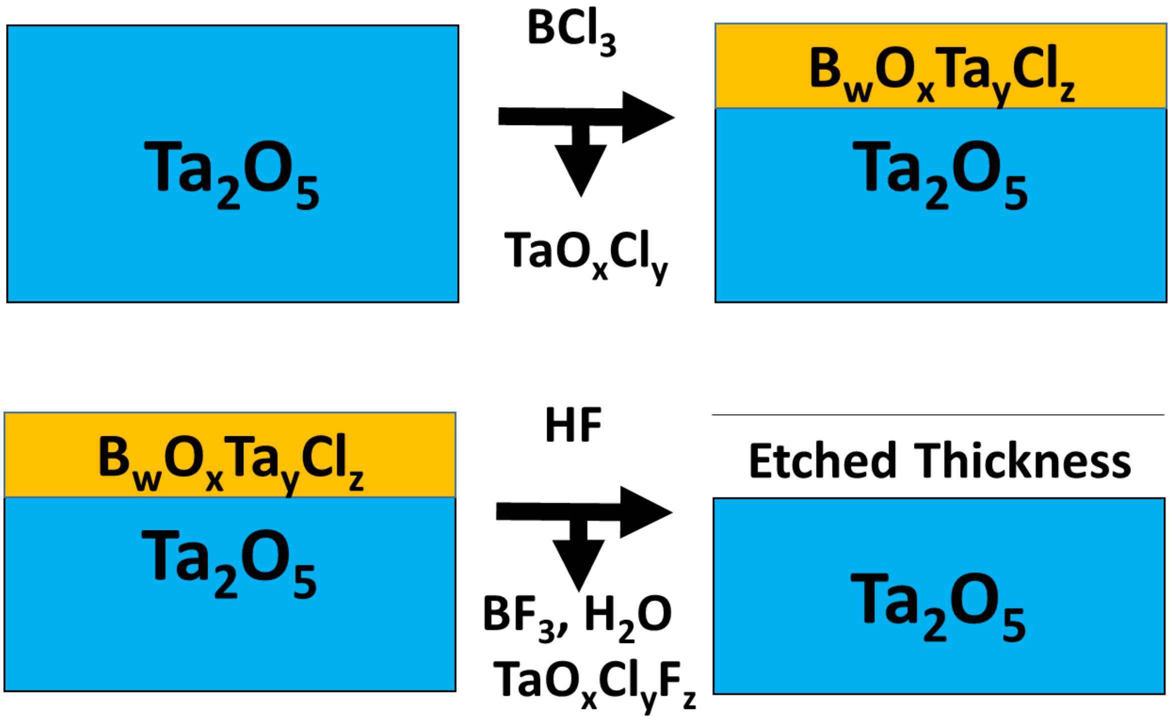

Figure 5-12. Conversion and fluorination reactions during Ta_2O_5 ALE. (a) Conversion of Ta_2O_5 to a $B_wO_xTa_yCl_z$ complex; (b) fluorination of the $B_wO_xTa_yCl_z$ surface layer by HF to BF_3, H_2O and $TaO_xCl_yF_z$.

5.3.3 TaN etching with O_3, BCl_3 and HF

5.3.3.1 TaN Oxidation

Another heavily used tantalum complex other than tantalum oxide is tantalum nitride. The conversion etch process of Ta_2O_5 can be extended to TaN. TaN can first be oxidized to Ta_2O_5. This process will be diffusion limited but can be controlled to a specific thickness. Once the TaN is oxidized to the determined thickness, the Ta_2O_5 can then be removed by BCl_3 and HF. The TaN film will then act as an etch stop. This process is similar to W etching with O_2/O_3, BCl_3 and HF.[139]

Tantalum nitride oxidation has been studied over a broad temperature range. TaN oxidized under a dry atmosphere oxidized at 600 ^oC. The TaN films completely converted into Ta_2O_5 with little nitrogen impurities.[164] Ta_2N films heated in air at 300 ^oC showed parabolic oxidation with an Ta_2O_5 oxide thickness of 80Å after a 4 hour exposure time.[165] TaN sputtered films oxidized in air at 350 ^oC showed a 24 Å reduction of the TaN film thickness to form the oxide.[166] No study was found for the oxidation of TaN_x ALD films using ozone, or using an oxygen plasma above room temperature.

Oxidation of TaN ALD films consecutive cycles of O_2/O_3 at 250 ^oC is shown in figure 13. A native oxide of 1-1.6 nm on the TaN films was seen via XRR. No native oxide thicknesses were found in literature for ALD TaN films, however, sputtered TaN films had a native oxide of 3 to 10Å. The oxidation conditions were a 20 seconds exposure at a O_2/O_3 pressure of 120 mTorr. The oxidation of TaN with O_2/O_3 shown in figure 13 follows oxidation with an oxide film growing rapidly, followed by a linear increase in the overall oxide thickness vs number of exposures. 6 cycles of O_2/O_3 resulted in a 46.1 Å thick Ta_2O_5 film on the TaN surface. TaN films were determined to have a film density of 60-65 % , and the Ta_2O_5 surface oxide had a film density of 95-100% as determined by XRR.

5.3.3.2 TaN ALE and Roughness Measurements by X-Ray Reflectivity

Figure 14 shows XRR measurements before and after etching through an oxidation etch process. 6 cycles of 120 mTorr O_2/O_3 were the conditions used to oxidize the TaN films. To remove the oxide, 60 AB etch cycles of 1000 mTorr 30 second static BCl_3 exposures, followed by 120 mTorr HF were the conditions used. Samples were removed from the chamber at 110 ^{o}C. A control showed no increase in oxidation thickness when TaN samples were removed at 110 ^{o}C. Samples had a native oxide of 10-16 Å. TaN thicknesses are 254.5, 205.8, 168.8, 134.8 and 101.3 Å, respectively. Roughness measurements were 8.38, 8.4, 8.9 and 9.8 Å showing that the film roughness may slightly roughen with consecutive etching supercycles.

The TaN thickness changer vs number of supercycles at 250 ^{o}C is shown in figure 15. The data in figure 15 is the same as figure 14. The etching is relatively linear with an R^2 value of 0.99. The amount of TaN lost per each supercycle is 37.74 Å. Different oxidation conditions would result in difference etch rates per supercycle.

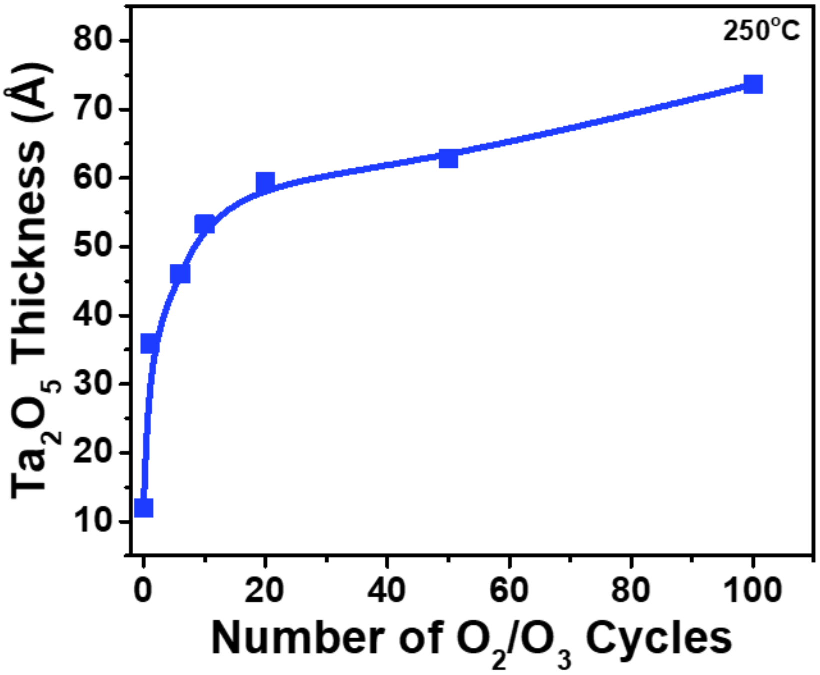

Figure 5-13. Ta_2O_5 thickness versus number of O_2/O_3 cycles. Oxidation is consistent with Deal-Grove kinetics.

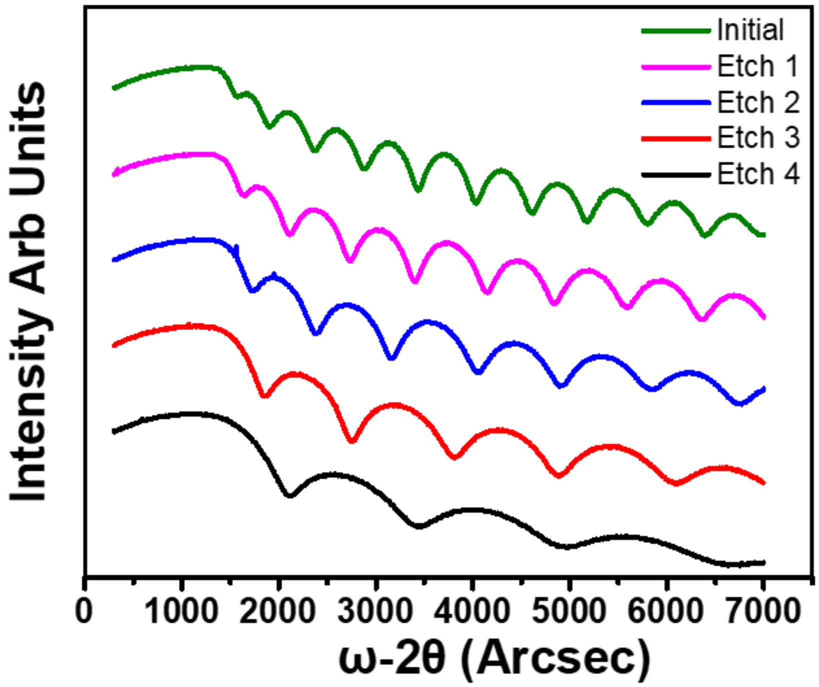

Figure 5-14: XRR spectra for TaN after 0, 1, 2, 3, and 4 supercycles.

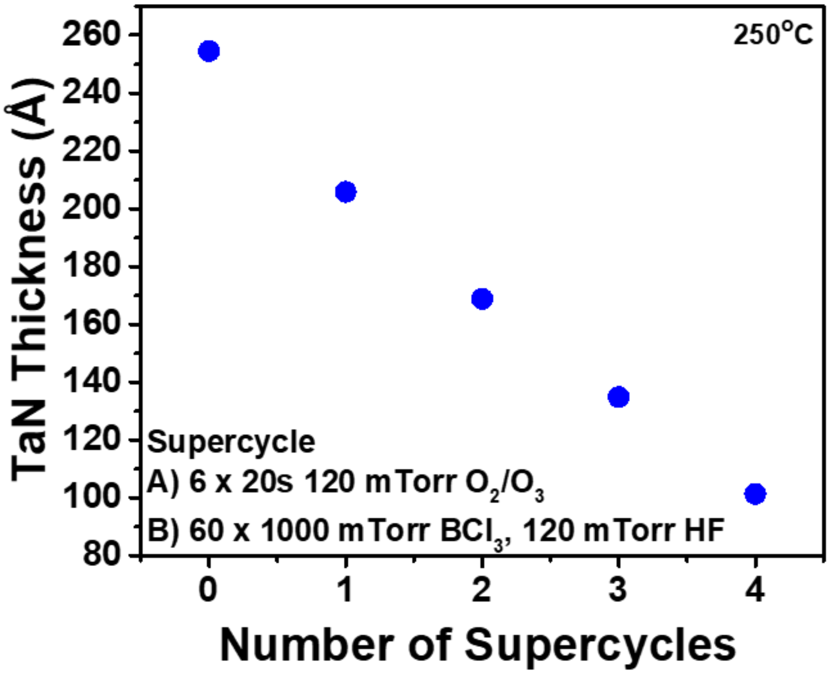

Figure 5-15. TaN thickness vs number of supercycles. Etching is relatively linear with an etch rate of 38 Å/supercycle.

5.4 Conclusion

Thermal ALE of Ta_2O_5 was demonstrated with BCl_3 and HF. Investigations into the reaction pathway showed that BCl_3 results in a thickness increase of the Ta_2O_5 film. The thickness increase is likely a result of boron and chlorine intercalation or reaction of the Ta_2O_5 surface. The modified surface is then removed by interaction with HF. HF reactions were self-limiting vs exposure however, BCl_3 exhibited an exposure dependence of the etch rate. Using conditions of 3 consecutive 30 s BCl_3 exposures at 130 mTorr and a viscous 0.25 s 120 mTorr HF exposure, the Ta_2O_5 etch rate varied from 0.95-1.09 Å/cycle. Ta_2O_5 ALE did demonstrate temperature dependence having an etch rate of 0.36 Å at 200 ^{o}C and an etch rate of 1.96 Å at 295 ^{o}C. Most notably, there was a pressure dependence of the Ta_2O_5 etch rate with BCl_3. Keeping HF exposures constant, a BCl_3 pressure of 130 mTorr resulted in an etch rate of 0.48 Å/cycle, whereas, a BCl_3 pressure of 1000 mTorr resulted in an etch rate of 1.46 Å/cycle. With the pressure dependence of BCl_3, it was shown that different self-limiting curves were dependent upon pressure. Lastly, films were shown via XRR to smoothen as more Ta_2O_5 ALE cycles were conducted.

TaN ALE was shown to be possible through and “oxidation-conversion-etch” by first oxidizing TaN films with O_2/O_3 and then removing the oxide layer with BCl_3 and HF. The TaN films were shown to be etched linearly through this process with an etch rate of 38 Å/supercycle. The TaN film roughness did increase slightly from 8.4 to 9.8 Å over 5 supercycles.

5.5 Acknowledgments

This research was funded through the Semiconductor Research Corporation. We are also grateful for Dr. Scott Clendenning of Intel for useful discussions and insight.

Chapter 6

Thermal Atomic Layer Etching of MOCVD GaN by Fluorination and Ligand-Exchange Pathways with BCl_3 and Fluorination Sources

6.1 Introduction

Atomic layer etching processes that only use heat to drive reactions is a relatively new field of etching techniques. ALE processes are based upon sequential self-limiting or pseudo-self-limiting reactions. Thermal ALE processes can remove material on the atomic scale with repeatable control. It is the reverse of ALD. Thermal ALE techniques are in need for the Semiconductor industry to assist with line edge roughness, gate all around structures and more.[14]

ALE process are in two categories: Plasma and Thermal. Regardless of the category chosen, ALE processes proceed through two steps: surface modification followed by the removal of the modified surface. For plasma ALE, a halogen or halocarbon film is adsorbed onto the surface changing the bond strength of the material just below the adsorbed surface.[14] After adsorption, ions are accelerated toward the surface at a specific energy which results in etching of the adsorbed surface, but not the underlying bulk material. Plasma based techniques following this process have etched Si[24], metal oxides[29, 131, 135], carbon materials[134, 167-168], and compound semiconductors such as GaAs[133] and InP[169].

Thermal based ALE techniques were shown to be based upon a variety of pathways. The early work of thermal ALE employs fluorination as the modification step followed by a ligand transfer as the removal step. This process was demonstrated to work for Al_2O_3, ZrO_2, HfO_2, AlF_3 and AlN using $Sn(acac)_2$, $Al(CH_3)_3$, $AlCl(CH_3)_2$ and $SiCl_4$[37-39, 170-171]. The second pathway for thermal ALE is called conversion etch. This process converts the initial surface to a new surface which can be etched away by fluorination or fluorination and ligand exchange reactions. This pathway demonstrated etching for WO_3[139], ZnO_2[172], TiN[163] and SiO_2[173]. Oxidation can be combined with conversion to etch materials such as, Si, Si_3N_4, and W[139]. Oxidizing the film changes the oxidation state of the initial surface to one that can be etched. Oxidizing metal film and then removing the metal oxide with organic reactants has etched Co, Pt, Pd, and Fe[174]. Other W and TiO_2 etching are based upon the formation of metal oxyfluorides or metal oxychlorides[175-176].

Multiple different dry etch techniques are employed to etch GaN. GaN etching uses chlorine containing plasma to produce volatile $GaCl_3$.[177] Chlorine gas along with with HBr, Ar, or BCl_3 plasmas can also be used to etch GaN[177-180]. $SiCl_4$ has been used with SF_6 and N_2 to etch GaN.[181] GaN can be etched spontaneously in a hydrogen environment at temperatures upwards of 800 °C[182] GaN ALE has recently been published by chlorination of the surface followed by low energy argion ions to remove the $GaCl_3$.[183-184] To date there exists no strict wet-etch chemistry for MOCVD GaN.[185], nor is there a thermal ALE approach for GaN.

GaN is an important direct semiconductor used in optoelectronics such as lasers and light-emitting diodes.[186-188] In addition to its optoelectronic properties, GaN has a high thermal stability, is chemically inert, with a high piezoelectric constant, and high electron mobility, making it very useful for high temperature and high power electronics.[189-190] GaN nanowire GAA transistor devices have exhibited better properties than Si or GaAs based devices[191] Thermal etching techniques can be useful for GaN devices, especially nanowire devices as it is difficult to etch the nanowire structure without damage[191]. In addition very thin films of GaN exhibit large amounts of dislocations which affect material properties.[192] Growth of larger films with an etch back may be useful. Lastly, as there is no isotropic etch for GaN below 800 ^{o}C, therefore, new device structures could be constructed with GaN ALE, or ALE could be used to remove surface impurities.

This work investigates thermal ALE of MOCVD GaN with XeF_2 and BCl_3. SF_4, HF, and a NF_3 plasma were also used with BCl_3 to investigate other fluorine sources for GaN ALE. *In situ* spectroscopic ellipsometry (SE) was used to determine etch rates and self-limiting conditions for GaN ALE. Pressure studies were conducted to help determine the reactions pathway.

BCl_3 has been shown to etch in a conversion-etch pathway with WO_3[139]. We reported earlier that BCl_3 interacts with the WO_3 surface transferring chlorine for oxygen. This forms a B_2O_3 layer on the surface while forming gaseous WO_2Cl_2. The remaining B_2O_3 surface is then etched by HF forming BF_3, and H_2O. This paper investigates whether a metal nitride could go through a conversion etch process, similar to WO_3 etching with BCl_3. The conversion of GaN with BCl_3 to solid BN and forming gaseous $GaCl_3$ is thermodynamically favorable and shown in eq 1.

(1) $GaN + BCl_3 \rightarrow GaCl_3(g) + BN$ ΔG at 200: -42.89 kcal/mol

After BN is formed, it could be spontaneously etched by HF, SF_4, XeF_2 and an NF_3 plasma shown in the equations below. NF_3 is shown as a fluorine radical.

(2) $BN + 3HF(g) \rightarrow BF_3(g) + NH_3(g)$ ΔG at 200: -16.40 kcal/mol

(3) $BN + SF_4(g) \rightarrow BF_3(g) + NSF(g)$ ΔG at 200: -57.83 kcal/mol

(4) $BN + 3XeF_2(g) \rightarrow BF_3(g) + NF_3(g) + 3Xe(g)$ ΔG at 200: -192.27 kcal/mol

(5) $BN + 6F(g) \rightarrow BF_3(g) + NF_3(g)$ ΔG at 200: -305.34 kcal/mol

With BN removed, the newly formed GaN surface then could interact with the residual fluorine source which may fluorinate the surface to GaF_3. HF, SF_4, XeF_2 and NF_3 plasmas are thermodynamically favorable to convert GaN to GaF_3 as shown in the equations below. GaN fluorination with XeF_2 has been demonstrated experimentally.[193]

(6) $GaN + HF(g) \rightarrow GaF_3 + NH_3(g)$ ΔG at 200: -39.99 kcal/mol

(7) $GaN + SF_4(g) \rightarrow GaF_3 + NSF(g)$ ΔG at 200: -81.41kcal/mol

(8) $GaN + 3XeF_2(g) \rightarrow GaF_3(g) + NF_3(g) + 3Xe(g)$ ΔG at 200: -215.86kcal/mol

(9) $GaN + 6F(g) \rightarrow GaF_3 + NF_3(g)$ ΔG at 200: -328.94kcal/mol

. The newly formed GaF_3 surface is then etched spontaneously by BCl_3 as shown in the equation below

(10) $GaF_3 + BCl_3 \rightarrow GaCl_3(g) + BF_3(g)$ ΔG at 200: -19.30 kcal/mol

Residual BCl_3 will further convert the newly formed GaN surface to BN. This process is repeated for GaN etching. Investigations into the actual reaction pathway are presented in the paper.

6.2 Experimental

6.2.1 GaN Samples and Reactor

3000Å thick MOCVD GaN films on sapphire were provided by NRL. Samples were cut into 1/2” square coupons and cleaned by a hot (85 ^{o}C) HCl bath to remove oxide followed by sonication for 10 minutes in acetone, then ethanol, and lastly isopropanol. Samples were then added to the reactor and heated on a sample stage in a reactor described previously.[161] The reactor walls were coated with 1500 cycles of Al_2O_3 ALD using trimethyl aluminum $Al(CH_3)_3$ and H_2O followed by 100 cycles of AlF_3 ALD with $Al(CH_3)_3$ and HF. The reactor walls were heated to 170 ^{o}C, whereas the sample stage temperature was varied for experiments.

6.2.2 Spectroscopic Ellipsometry

Etching experiments were analyzed by SE using an *in-situ* M-2000D ellipsometer from J.A. Woollam. The incident angle for all experiments was 70^{o} with a spectral range of 239.2-1687.2 nm. GaN film thicknesses were measured after each full cycle or each reaction. Changes in GaN film thickness was analyzed by the complete ease software from J.A. Woollam. A GaN oscillator model provided by the Complete Ease software consisting of a PSemi-MO, two PSemi-Tri, and a Gaussian oscillator was used for thickness determination. Due to the large thickness of the GaN films, exhibiting bulk characteristics, no parameters were changed during ALE as there was no increase in lowering modelling error.

6.2.3 Precursors and Dosing Parameters

Boron trichloride (99.9%, Synquest Laboratories), Xenon difluoride (99.5%, Strem Chemicals), HF-pyridine (70 wt% HF Sigma-Aldrich), SF_4 (94% Synquest Laboratories) and NF_3 (99.9% Airgas) were used as the reactants. Reactants were dosed separately into the reaction chamber under a stream of Argon (Pre-Purified), unless held statically for a defined amount of time. The reactants were dosed using two pneumatic valves (Swagelok-HBVVCR4-C for NF_3, BCL_3, and XeF_2 or Swagelok-6LVV-DPFR4-P-C for HF) on either side of a conductance limiting valve (Swagelok SS-4BMG-VCR). LabView was used for pneumatic actuation.

Between reactant doses, a stream of argon (pre-purified) was used to flush out excess reactant at a pressure of 1270 mTorr. For repeated exposures of XeF_2, a purge time of 60 seconds was used between doses. SF_4, NF_3, and BCl_3 purge times were 60 seconds regardless of viscous or static dosing. HF purge times were larger at 70 seconds due to its long residence time in the chamber. The chamber was pumped by a dual rotary Alcatel Adixen Pascal 2015 SD pump.

6.3 Atomic Layer Etching of MOCVD GaN with BCl_3 and XeF_2

6.3.1 MOCVD GaN Etching Using BCl_3 and XeF_2

Figure 1. shows GaN thickness measured by in situ SE during etching. The resulting etching was an AB exposure sequence using BCl_3 and XeF_2 as the reactants. Figure 1 shows the change of GaN thickness during GaN ALE for 30 cycles at 195 ^{o}C. The AB reaction sequence was 40 mTorr of XeF_2 held statically for 20 seconds followed by a 0.5 second viscous BCl_3 at

50 mTorr. Between each reactant exposure, the chamber was purged by PP argon for 60 seconds. Each data point in figure 1 represents a thickness measurement after one complete etch cycle. GaN etching is linear with an R^2 value of 0.999. The etch rate for GaN ALE at 195 ^oC is 0.55 Å/cycle. The etch rate at 195 ^oC under these conditions varied from 0.50 to 0.59 Å/cycle. Crystalline GaN grown on sapphire have lattice constants a=3.18 Å and c=5.18 Å.[194] The GaN ALE etch rate at 195 ^oC is roughly a ninth of a monolayer per cycle.

6.3.2 Self-Limiting Studies with BCl_3 and XeF_2 at 195^{o}C

Both BCl_3 and XeF_2 were required for etching to occur. No changes in thickness or optical properties were seen with repeated BCl_3 exposures. XeF_2 alone did not etch GaN, rather it fluorinated it. Figure 2 examines the self-limiting reaction of BCl_3 during GaN ALE at 195 ^oC. XeF_2 was held constant at 40 mTorr static doses with the number of consecutive BCl_3 doses varied to determine the etch rate. Between each reactant dose, the chamber was purged with 1260 mTorr PP Ar for 60 seconds. The first dose of BCl_3 corresponded to an etch rate of 0.55 Å/cycle. More consecutive BCl_3 doses does not result in a higher etch rate. At 195 ^oC, the etch rate varied from 0.50 to 0.59 Å/cycle. The lack of an exposure dependence of BCl_3 argues for a ligand-exchange based reaction.

XeF_2 fluorinates materials by adsorption on to the surface followed by dissociation into Xenon gas and fluorine radicals.[193] The formed GaF_3 surface is stable until 550 ^oC.[193] Fluorine radicals that oxidize the surface resulting in a GaF_3 film should be observable by SE at 195 ^oC. The thickness of formed GaF_3 from one XeF_2 exposure is below the detection limit of the ellipsometer as no change in psi and delta were observed. 60 repeated XeF_2 exposures of 40 mTorr for 20 seconds did not result in a GaF_3 layer detected by ellipsometry, or any observable change in psi and delta. Therefore, the fluorination of GaN with XeF_2 at 195 ^oC is surface limited.

Figure 3 displays the self-limiting behavior of the XeF_2 reaction for GaN ALE at 195 ^oC. BCl_3 exposures were held constant at a 0.5 second viscous doses of 50 mTorr. The number of consecutive XeF_2 doses was varied, however, exposures were 40 mTorr held statically for 20 seconds. Figure 3 shows that there is not a self-limiting exposure for XeF_2. However, the XeF_2 reaction exhibits diffusion like characteristics. This is a result of the fluorination of GaN by XeF_2. XeF_2 dissociates on the GaN surface and then fluorinates by diffusing through the GaN surface. The increase in etch rate is a result of a thicker GaF_3 formed due to increased time for diffusion to occur. One XeF_2 exposure resulted in an etch rate of 0.55 Å/cycle whereas, 6 consecutive XeF_2 exposures had an etch rate of 1.03 Å/cycle. These results show the etch rate is dependent upon XeF_2 exposure and that the BCl_3 reaction only removes the GaF_3 surface that is formed. The right of Figure 3. is the average GaF_3 thickness as determined by the etch rate assuming only ligand-exchange occurs. After 6 exposures of XeF_2 an average fluoride thickness of 2Å is formed which is below the model error when assuming a surface fluoride is formed.

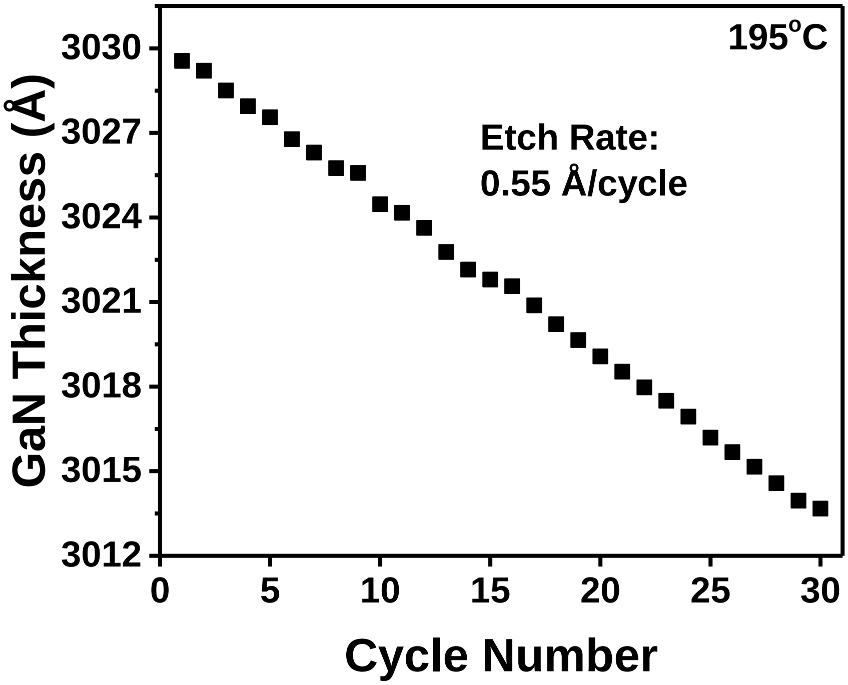

Figure 6-1: GaN thickness versus number of GaN ALE cycles at 195 °C. At 195 °C the etch rate is 0.55 Å/cycle

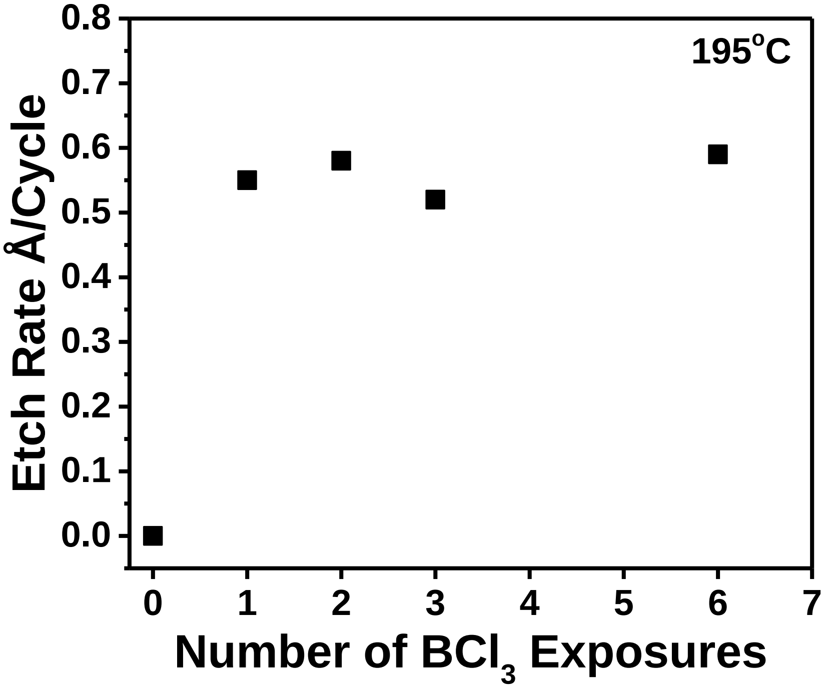

Figure 6-2: GaN etch rate versus number of BCl_3 exposures. Saturation is reached after 1 BCl_3 exposure.

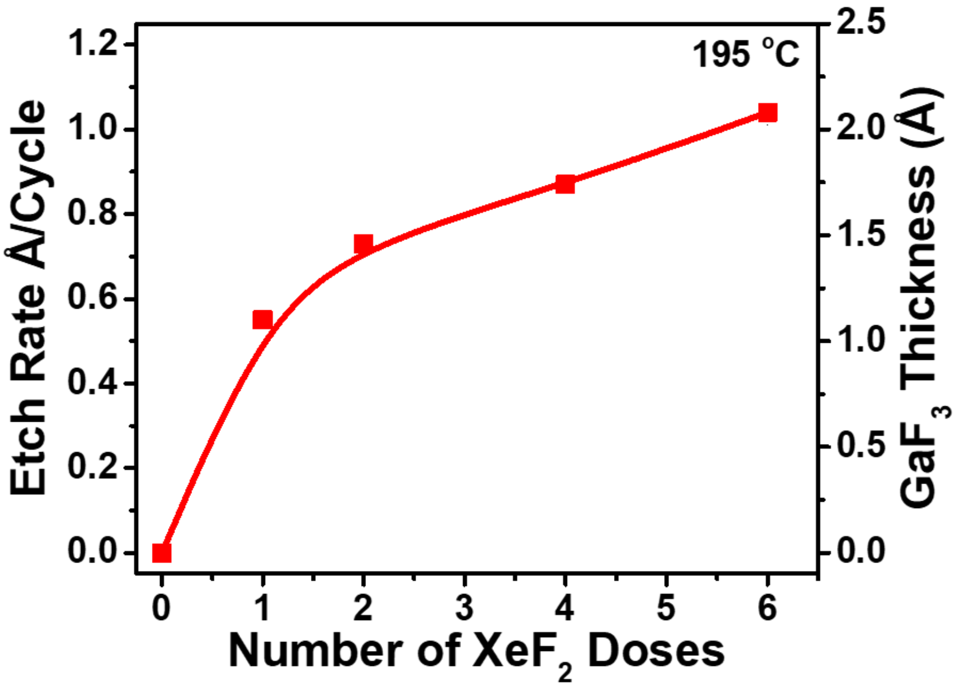

Figure 6-3: GaN etch rate vs number of XeF_2 exposures. GaN etch rate increases with increasing XeF_2 exposures due to larger GaF_3 thickness. Expected GaF_3 thickness as determined by the GaN etch rate at 195 °C

6.3.3 Temperature Dependence of MOCVD GaN ALE

The change in GaN thickness vs number of reaction cycles at varying temperatures is shown in Figure 4. One 20 second 40 mTorr XeF_2 static exposure and one 0.5 second viscous 50 mTorr BCl_3 were the conditions used for all temperatures. All thicknesses were normalized to the same thickness of 3093 Å to show variations in etching at 170, 182.5, 195, 250 and 300 ^{o}C. Etching is linear at all temperatures for 30 reaction cycles. For the temperatures of 170, 182.5, 195, 250, and 300, the etch rates are 0.17, 0.31, 0.55, 0.63, and 0.71 Å/cycle, respectively. The increase in etch rate is a result of a thicker GaF_3/GaN_xF_y surface layer formed by interaction with XeF_2, which is then removed spontaneously by BCl_3.

6.3.4 MOCVD GaN ALE at 250 ^{o}C

GaN ALE was also studied at 250 ^{o}C. Figure 5 depicts the change of GaN thickness vs number of cycles at 250 ^{o}C. The same conditions used at 195 ^{o}C were used at 250^{o}C. the etching is linear with an R^2 value of 0.999. The etch rate at 250 ^{o}C is 0.67 Å/cycle. The etch rate is roughly one eighth of a full GaN atomic layer.

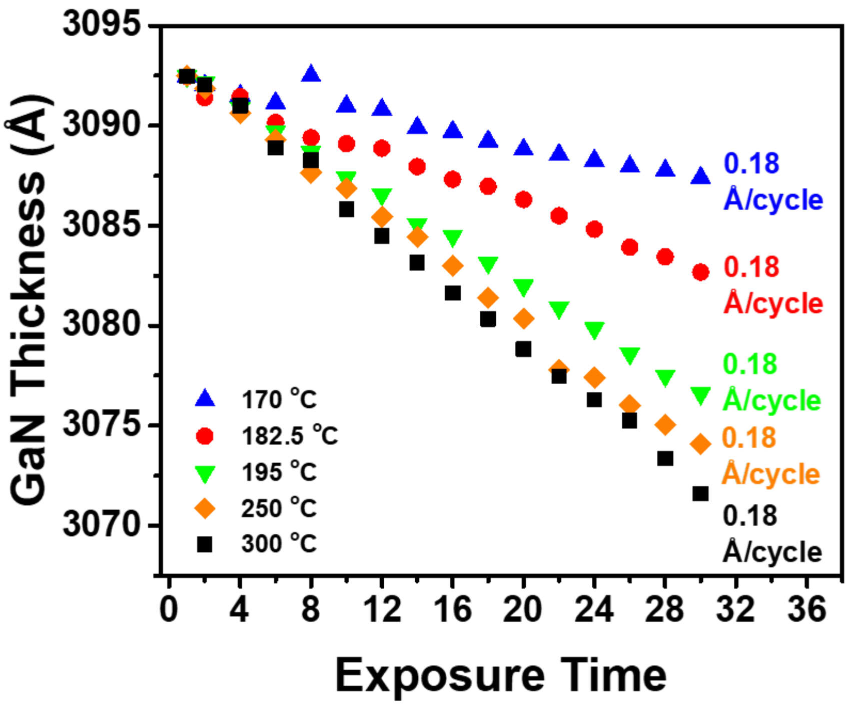

Figure 6-4. GaN thickness versus number of cycles at temperatures of 170, 182.5, 195, 250 and 300 ^{o}C. Data points are shown every 2 cycles for clarity.

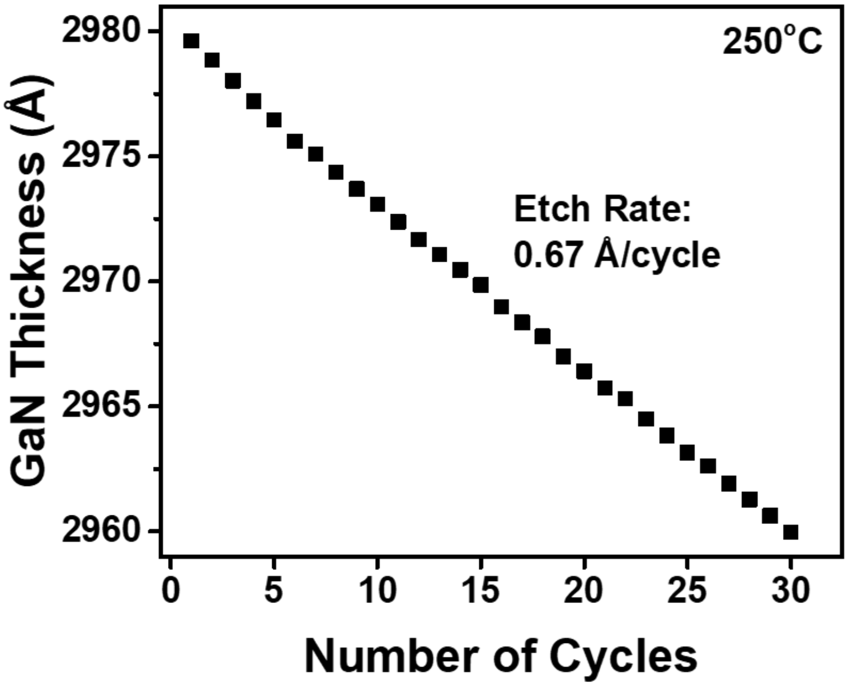

Figure 6-5. GaN thickness versus number of cycles for GaN ALE at 250. Etching is linear with an etch rate of 0.64 Å/cycle.

6.3.5 Self-Limiting Studies at 250 ^{o}C

The self-limiting nature of the BCl_3 reaction was investigated at 250 ^{o}C. Figure 6 shows the change in etch rate per cycle vs number of BCl_3 exposures. The number of BCl_3 exposures was varied while XeF_2 was held constant at a 20 s exposure of 40 mTorr. The BCl_3 exposure was the same here as at 195 ^{o}C. One exposure of BCl_3 resulted in an etch rate of 0.63 Å. An increase in the number of consecutive BCl_3 exposures did not result in a change in the etch rate, arguing for a ligand-exchange pathway. At 250 ^{o}C the etch rate using one BCl_3 and XeF_2 exposure varied from 0.63-0.67 Å/cycle.

The fluorination of GaN with XeF_2 was studied with SE at 250 ^{o}C. However, no model was able to de-couple the optical properties of GaN and GaF_3. A thickness increase was seen with SE, however, due to the optical coupling, no accurate thickness measurement could be made. Psi and Delta did change with repeated exposures of XeF_2. The change showed that a film of large thickness was being formed with repeated XeF_2 exposures. This is the result of a non-passivating GaF_3/GaN_xF_y layer being formed at high temperatures.

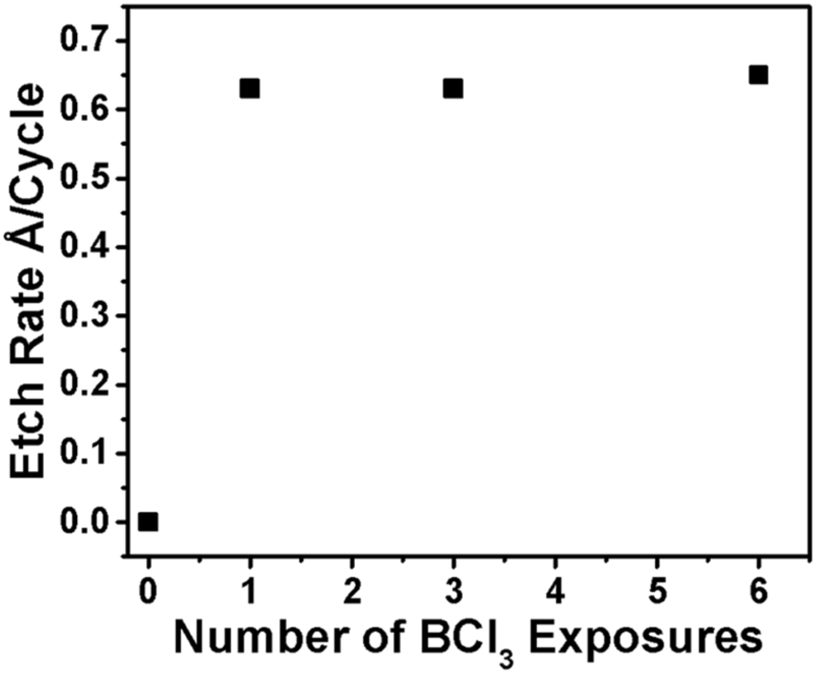

Figure 6-6. GaN etch rate vs number of BCl_3 exposures at 250 ^{o}C. Saturation is reached with one BCl_3 exposure showing that regardless of temperature, the BCl_3 reaction is self-limiting.

6.3.6 BCl_3 Pressure Dependence on The Etch Rate

ALE of Ta_2O_5 with BCl_3 and HF showed higher pressures of BCl_3 resulted in larger etch rates. This was a result of greater conversion of the Ta_2O_5 surface. Figure 7 investigates the pressure dependence of BCl_3 on the etch rate for GaN ALE at pressures of 250, 500 and 1000 mTorr held statically for 5 seconds. XeF_2 conditions were held at 40 mTorr for 20 seconds. At 195 ^{o}C etch rates were 0.56, 0.57, 0.62 Å/cycle for 250, 500, 1000 mTorr which is in good agreement of the range of 0.5-0.6 Å/cycle. At 250 ^{o}C etch rates were 0.63, 0.68, and 0.63 Å/cycle for 250, 500, and 1000 mTorr respectively.

At both 195 ^{o}C and 250 ^{o}C the etch rates show no dependence on pressure. Etch rate increases were only observed with changing XeF_2 conditions. Based upon this evidence, BCl_3 does not convert the surface of GaN to BN while forming $GaCl_3$. If conversion were to occur, there should be a pressure dependence on the etch rate. It is likely that the mechanism follows through ligand exchange. Rather than conversion to BN from BCl_3, XeF_2 fluorinates the GaN to GaF_3 which is then spontaneously etched by BCl_3 (eq 10).

6.3.7 Reaction Pathway Determination

Figure 8 shows the GaN thickness change as determined by SE after each BCl_3 and HF exposure amidst GaN ALE at 250 ^{o}C for 9 half-cycles. The film was assumed to be GaN by SE modelling as adding a Cauchy layer for the dielectric GaF_3 increased modelling error. The thickness for GaN decreases over the number of half-cycles; however, a thickness increase occurs after interaction with BCl_3, along with a thickness decrease after each XeF_2 exposure.

The GaN thickness loss of 0.63 Å during a full ALE cycle represents 4.4 X 10^{-10} mol/cm^2 based on a GaN density of 6.15 g/cm^3 and a molar mass of 83.73 g/mol. With a thickness gain of 0.79 Å per half cycle, or 1.42 Å for the overall cycle, the BN layer would have a density of 0.76 g/cm^2 assuming a BN molar mass of 24.8 g/mol. This density is much less than either wurtzite BN at 2.1 g/cm^2 or cubic BN at 3.45 g/cm^2. It is highly unlikely a film of BN with such a low-density exists on the surface, rather the thickness increase is likely from residual chlorine on the surface. The diameter of chlorine is ~ 1.75 Å which is close to the 1.42 Å increase after each BCl_3 dose. This evidence argues for ligand-exchange, not conversion-etch.

Based upon presented evidence, it is likely that GaN ALE proceeds through a ligand exchange process rather than a conversion etch. The proposed reaction pathway is shown in figure 9. In the first reaction, XeF_2 fluorinated the GaN surface, removing the nitrogen as NF_3. In step B, the GaF_3 is removed spontaneously by BCl_3 forming volatile $GaCl_3$ and BF_3. The process can be repeated for removal of GaN.

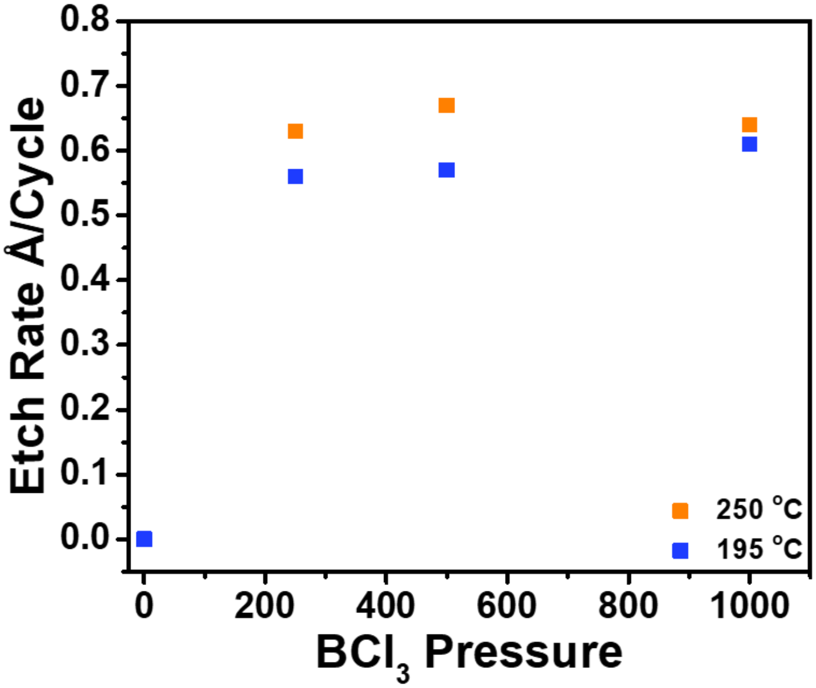

Figure 6-7. GaN etch rate versus BCl_3 pressure at 195 and 250 °C. At 195 °C, the etch rate is independent of BCl_3 pressure at ~0.57 Å/cycle; at 250 °C the etch rate is again independent of BCl_3 pressure at ~0.65 Å/cycle.

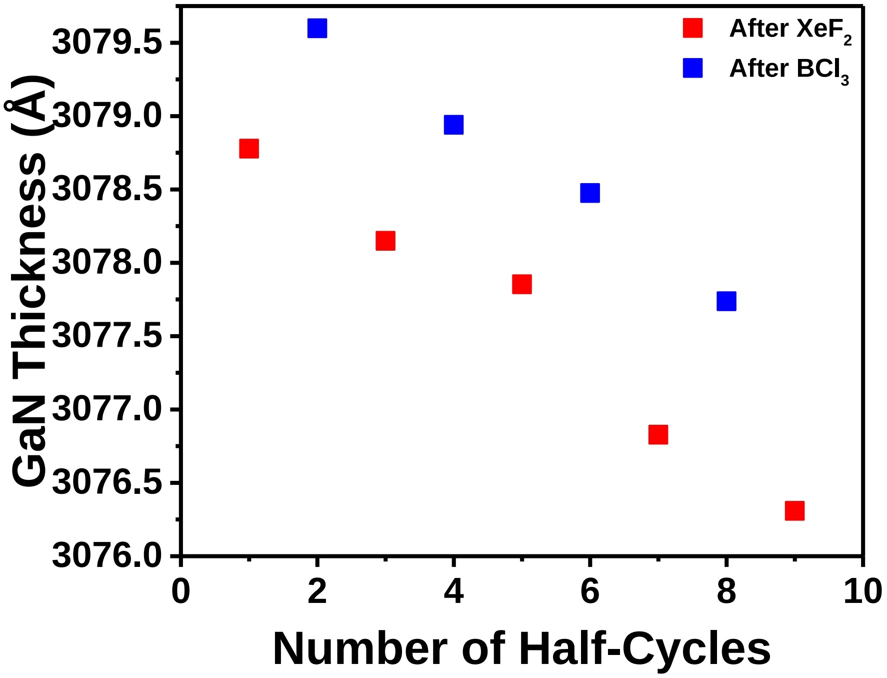

Figure 6-8. GaN thickness versus number of half-cycles during GaN ALE at 250 ºC under self-limiting conditions

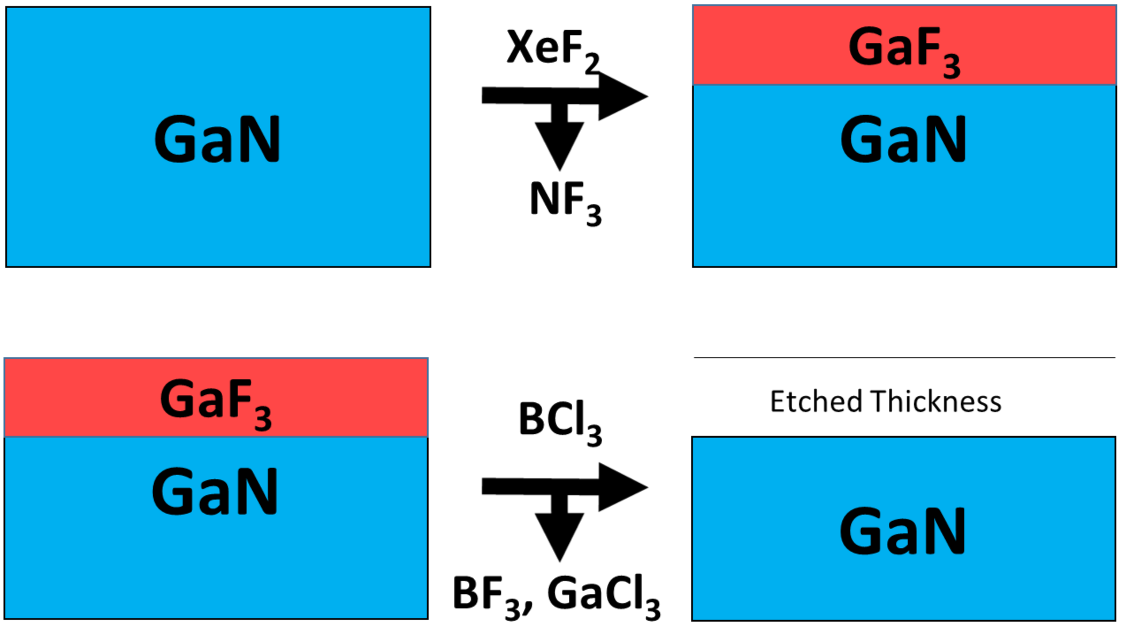

Figure 6-9. Fluorination and ligand exchange reactions. (A) Fluorination of GaN to GaF_3 by XeF_2; (B) removal of the GaF_3 surface layer by BCl_3 forming volatile $GaCl_3$ and BF_3.

6.4 MOCVD GAN Etching with SF_4, HF, NF_3 Plasma

6.4.1 MOCVD GaN Etching with HF/SF_4

Figure 10 and 11 shows the thickness change of MOCVD GaN vs number of ALE cycles with BCl_3 and HF or SF_4 at 250 ^oC. BCl_3 pressures transients were 50 mTorr for a 0.5 second viscous dose. HF or SF_4 doses were held statically for 20 seconds at 300 or 500 mTorr pressures. There is no thickness change over the 20 cycles of GaN ALE with BCl_3 and HF or BCl_3 and SF_4. Although HF and SF_4 are thermodynamically predicted to fluorinate GaN to GaF_3 (eq 2,3), this does not occur. MOCVD GaN has been shown to be chemically resistant a variety of hot acids[185], and it is likely to be chemically resistant. This may explain its resistant ability to certain fluorination sources. This likely could change for films that are amorphous or polycrystalline.

6.4.2 MOCVD GaN Etching with NF_3 Plasma

The GaN thickness vs number of ALE cycles using a NF_3 plasma as the fluorination source is shown in figure 12. BCl_3 was dosed viscously into the chamber for 0.5 seconds at a pressure of 50 mTorr. NF_3 was dosed into the chamber at a pressure of 40 mTorr for 25 seconds. The plasma was arced after 5 seconds at a power of 75 watts for the remaining 20 seconds. Over the 20 cycles, the etch rate is 2.85 Å/cycle. The etching linear with an R^2 value of 0.999. The use of an NF_3 plasma would allow for isotropic etching of GaN devices.

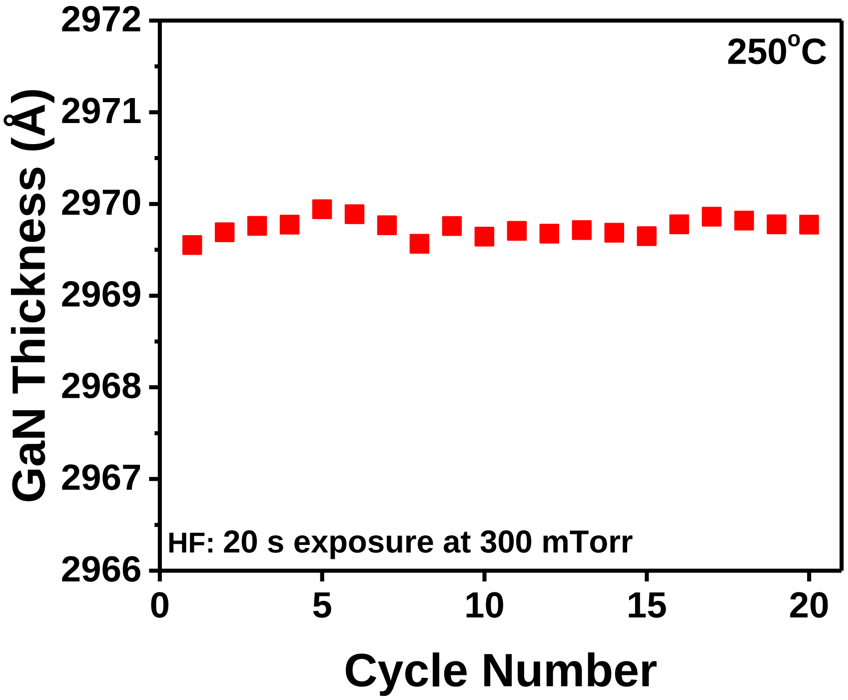

Figure 6-10. GaN thickness vs number of cycles for GaN ALE at 250 °C using BCl_3 and HF. No etching is observed using HF as the fluorinating agent.

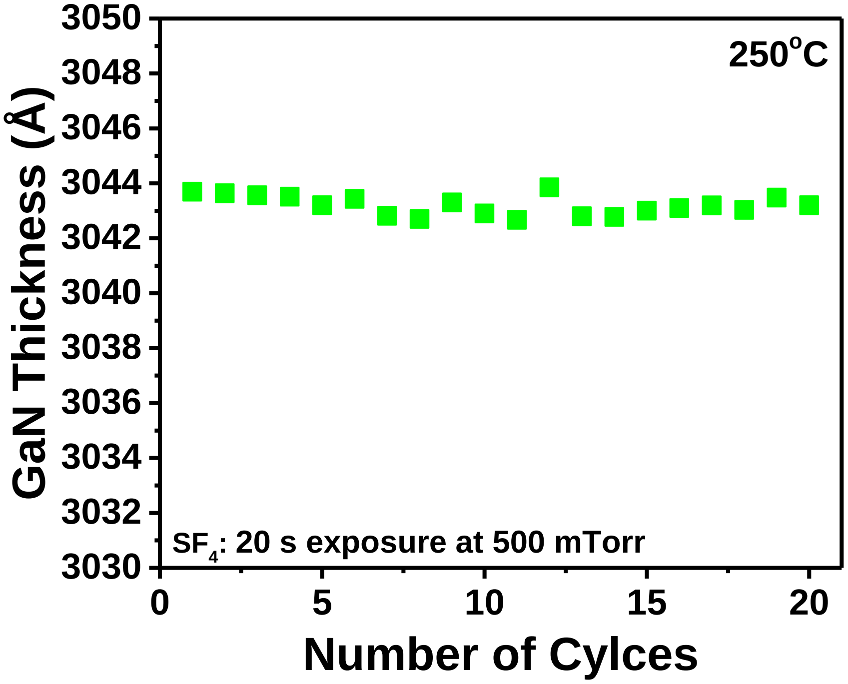

Figure 6-11. GaN thickness versus number of cycles during GaN ALE at 250 °C using BCl_3 and SF_4. No etching is observed when using SF_4 as the fluorination source

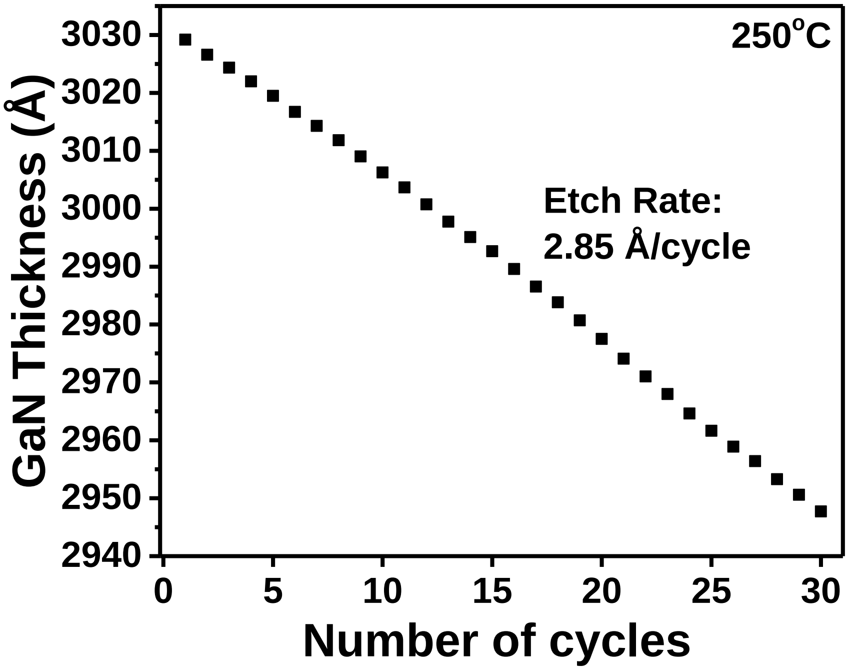

Figure 6-12: GaN thickness versus number of cycles for GaN ALE at 250 °C using BCl_3 and a NF_3 plasma. With a NF_3 plasma as the fluorinating agent, the etch rate is 2.85 Å/cycle

6.5 Extension of Ligand Exchange to Various Fluorides with BCl_3, $B(CH_3)_3$

The ligand-exchange process, or spontaneous etch of a metal fluoride through interaction with BCl_3 can be useful for other materials. Many semiconductor relevant materials are in the form of metal phosphides, sulfides, arsenides, carbides, selenides, and tellurides. Each compound semiconductor can be fluorinated to non-volatile fluoride and etched spontaneously with boron compounds. Metals with volatile chlorides or methylated complexes include Fe, Sb, Te, Sn, Zr, Hf, Pb, Ti, and In. Table 1. contains the ΔG values for a variety of ligand exchange reactions of metal fluorides with BCl_3 and $B(CH_3)_3$. Materials such as InP GaAsP, or SnS would first be fluorinated by using a fluorination source such as HF, SF_4, XeF_2 or a fluorine containing plasma. The metal fluoride will then undergo a ligand transfer with BF_3 or $B(CH_3)_3$. The ligand transfer reactions with BCl_3 and $B(CH_3)_3$ are important as the byproduct, BF_3 is a gas. No unwanted depositions will occur if the walls are at a lower temperature than the sample. The metal chlorides and methyl metals are all volatile at 200 ^oC. The exception is Titanium which is shown at 100 ^oC due to TiF_4 being a gas at 150 ^oC and above.

We reported earlier that selectivity could occur with the selection of different ligands. In the case of Ga vs In, BCl_3 could etch Ga complexes, but not In complexes as $InCl_3$ is not volatile. With $B(CH_3)_3$, formation of $Ga(CH_3)_3$ is thermodynamically unfavorable to undergo a conversion-etch or ligand transfer, but $In(CH_3)_3$ formation is thermodynamically favorable. A complex such as InGaN or $InGaO_3$ could be etched with a with a bi-ligand complex such as $B(CH_3)_2Cl$. The methyl ligands will etch In and the Cl will etch Ga.

Table 6-1. Thermodynamic data of various fluorides interaction with BCl_3 or $B(CH_3)_3$

$BCl_3(g) + FeF_3 \rightarrow BF_3(g) + FeCl_3\ (g)$	ΔG at 200: -20.26 kcal/mol
$BCl_3(g) + SbF_3 \rightarrow BF_3(g) + SbCl_3\ (g)$	ΔG at 200: -50.64 kcal/mol
$BCl_3(g) + ¾\ TiF_4 \rightarrow BF_3(g) + ¾\ TiCl_4\ (g)$	ΔG at 100: -27.89 kcal/mol
$BCl_3(g) + ¾\ TeF_4 \rightarrow BF_3(g) + ¾\ TeCl_4\ (g)$	ΔG at 200: -70.13 kcal/mol
$BCl_3(g) + ¾\ SnF_4 \rightarrow BF_3(g) + ¾\ SnCl_4\ (g)$	ΔG at 200: -65.02 kcal/mol
$BCl_3(g) + ¾\ ZrF_4 \rightarrow BF_3(g) + ¾\ ZrCl_4\ (g)$	ΔG at 200: -5.72 kcal/mol
$BCl_3(g) + ¾\ HfF_4 \rightarrow BF_3(g) + ¾\ HfCl_4\ (g)$	ΔG at 200: -6.52 kcal/mol
$BCl_3(g) + ¾\ PbF_4 \rightarrow BF_3(g) + ¾\ PbCl_4\ (g)$	ΔG at 200: -82.64 kcal/mol
$B(CH_3)_3(g) + ¾\ SnF_4 \rightarrow ¾\ Sn(CH_3)_4(g) + BF_3(g)$	ΔG at 200: -49.69 kcal/mol
$B(CH_3)_3(g) + InF_3 \rightarrow In(CH_3)_3(g) + BF_3(g)$	ΔG at 200: -28.20 kcal/mol
$B(CH_3)_3(g) + ¾\ PbF_4 \rightarrow ¾\ Pb(CH_3)_4(g) + BF_3(g)$	ΔG at 200: -66.92 kcal/mol

6.6 Conclusions

Thermal ALE of GaN with BCl_3 and multiple fluorination sources were investigated. The ALE of GaN used an AB sequence of XeF_2 and BCl_3. Etch rates at 195 and 250 ^{o}C were on average 0.55 and 0.65 Å/cycle. GaN ALE proceeds through a ligand-exchange pathway, where GaN is fluorinated to GaF_3. The GaF_3 is then spontaneously removed by BCl_3 likely forming GaF_xCl_y and BF_xCl_x. BCl_3 was shown to have no pressure or exposure dependence on the etch rate, whereas, varying XeF_2 exposures resulted in different etch rates. GaN ALE was conducted over a temperature range of 170 to 300. At 170, GaN etch rates were 0.18 Å/cycle, and at 300 ^{o}C etch rates were 0.75 Å/cycle. HF, SF_4 and an NF_3 plasma were employed as alternative fluorinating sources for GaN ALE. HF and SF_4 did not result in ALE of GaN, likely as they do not fluorinate MOCVD GaN. At 250 ^{o}C, an NF_3 plasma had an etch rate of 2.43 Å/cycle, allowing for anisotropic etching of GaN to occur. The ligand exchange process using with BCl_3 and $B(CH_3)_3$ with a variety of metal fluorides was shown to be thermodynamically favorable allowing for many metal derivatives with stable fluorides but volatile chlorides to be etched.

6.7 Aknowledgements

This work was funded in full by the Semiconductor Research Corporation. The authors would like to that Dr. Scott Clendenning and his team for their input and thoughtful conversations.

Chapter 7

Thermal Atomic Layer Etching of Ga_2O_3 with BCl_3 and HF

7.1 Introduction

Thermal atomic layer etching (ALE) is a new field of isotropic etching using heat and surface reactions as the reactive driving force. This method is similar to atomic layer deposition in that it is based upon sequential, self-limiting reactions in an AB sequence. In general ALE proceeds through modification of the initial surface to a surface that can be etched by an incoming gas that creates two volatile species. Several different pathways of thermal ALE have been documented in literature. Thermal ALE has been demonstrated by fluorination of HfO_2, ZrO_2, AlN, ZnO_2, followed by a ligand exchange reaction with $Sn(acac)_2$, $Al(CH_3)_3$, $AlCl(CH_3)_2$ and $SiCl_4$.[35-39, 170, 195-196] Thermal ALE has also been demonstrated through a conversion etch pathway as well. In this pathway, the initial surface is converted to a different metal oxide which can then be etched away by fluorination or ligand-exchange reactions. WO_3[139], ZnO_2[172], TiN[163] and SiO_2[173] etching has been shown to etch with this pathway. Oxidation in combination with conversion to etch Si, Si_3N_4 and W[139].

The thermal etching of Ga_2O_3 may be important for future high electron mobility devices (HEMT) devices. Ga_2O_3 is of high interest for electronic device applications due to it high breakdown voltage[197] and large bandgap of 4.5-4.9 eV[198]. The breakdown voltage is two time greater than SiC and GaN[199] allowing for more than triple the power performance.[198] The saturation velocity of Ga_2O_3 is estimated to be 2E-7[200], which is double that of Si.[201] Physical devices with Ga_2O_3 are being reported. Vertical FETs comprised of Ga_2O_3 were shown to be suitable for high power and voltage applications.[202] Ga_2O_3 MOSFETs were constructed having stable device performance up to 300 ^{o}C, with large on/off ratios larger than ten orders of magnitude.[203] Recently, ALD grown Ga_2O_3 films were used as the gate dielectric showing gate leakage two orders of magnitude lower than normal HEMTs, and had an efficiency enhancement of 9%.[204]

This work presents the thermal atomic layer etching of Ga_2O_3 with BCl_3 and HF through "conversion-etch" and/or ligand-exchange reactions. BCl_3 has been shown to etch through conversion etch[139] and is thermodynamically expected to etch certain metal fluorides. The steps based upon "conversion-etch" and ligand exchange are all thermodynamically favorable for Ga_2O_3[205]. The expected interaction of Ga_2O_3 with Ga_2O_3 makes B_2O_3 and volatile $GaCl_3$. The standard free energy change and reaction of BCl_3 and Ga_2O_3 at 200 ^oC are shown in eq 1.

(1) $Ga_2O_3 + 2BCl_3(g) \rightarrow B_2O_3 + 2$ ΔG at 200 ^oC = -62.00 Kcal
$GaCl_3(g)$

The B_2O_3 layer is spontaneous removed by HF and was shown previously[139]. Residual fluorine will react with the Ga_2O_3 surface forming GaF_3 and H_2O . The standard free energy change at 200 ^oC of HF interaction with Ga_2O_3 are shown in eq 2.

(2) $Ga_2O_3 + 6HF(g) \rightarrow 2GaF_3 + 3H_2O(g)$ ΔG at 200 ^oC = -40.73 Kcal

Once GaF_3 is formed, it can be spontaneously etched by BCl_3 as shown in eq 3.

(3) $GaF_3 + BCl_3(g) \rightarrow BF_3(g) + GaCl_3(g)$ ΔG at 200 ^oC = -19.30 Kcal

Residual BCl_3 will then convert the Ga_2O_3 surface to B_2O_3. These steps are repeated for Ga_2O_3 etching. Investigations into the reaction pathway are presented in this paper.

7.2 Experimental

7.2.1 Ga_2O_3 ALD Reaction Conditions

Ga_2O_3 samples were grown onto a 5000 Å thick thermal oxide on silicon. Ga_2O_3 films were grown with trimethylgallium (Sigma-Aldrich 99.9999%) and an O_2 (Airgas UHP) plasma at 200 ^oC. Ga_2O_3 films were grown in a reaction chamber that has been described previously[161]. The chamber was pumped with an Alcatel Adixen Pascal 2015 SD pump. A capacitance manometer was used for pressure measurements.

7.2.2 ICP Plasma Generation

An ICP plasma source created the oxygen radicals used for Ga_2O_3 ALE. The ICP source was a helical copper coil with a quartz tube of dimensions 6 cm inner diameter by 25 cm long as the ICP source. A 50 Ω impedance matching network (Navigator Digital Matching Network, Advanced Energy) and a 13.56 MHz RF generation (Paramount RF Power Supply, Advanced Energy) we used together to generate the plasma.

7.2.3 Ga_2O_3 ALE Reaction Conditions

Ga_2O_3 films were set upon a heated sample stage inside the reactor chamber. The samples were then heated to the desired temperature. The chamber walls of the reactor were heated to 170 ^oC for all experiments. BCl_3 (Synquest Laboratories, 99.9%), and HF-Pyridine (Sigma-Aldrich 70 wt. % HF) were used as the reactants for etching. Each reactant was dosed separately and statically into the chamber with a background Argon pressure of 1220 mTorr. After BCl_3, the chamber was purged for 60 seconds with; after HF the chamber was purged for 70 seconds due to its long residence time in the reactor. Each reactant was purged with Argon at a base pressure of 1270 mTorr.

7.2.4 Spectroscopic Ellipsometry

Etching was analyzed by an *in situ* M-2000D spectroscopic ellipsometer provided by JA Woollamm. The incident angle for all SE experiments was 70°. The ellipsometer had a spectral range from 239.2-1687.2 nm. The Ga_2O_3 films were analyzed with the Compleate Ease software from JA Woollam. A Cauchy dispersion model was used for film thickness measurements as Ga_2O_5 has a large bandgap of ~4.5-4.9 eV. All parameters of the Cauchy model were varied for accurate film measurements. The index of refraction for the films remained ~1.85-1.86 throughout etching.

7.3 Results and Discussion

7.3.1 Ga_2O_3 ALD

The growth of Ga_2O_3 as measured by SE at 200 °C is shown in figure 1. The ALD of Ga_2O_3 was done through an AB sequence of Trimethylgallium (TMGa) and an O_2 plasma. TMGa was dosed statically in the chamber for 5 seconds at a pressure of 120 mTorr. O_2 was dosed into the chamber for 25 seconds. The plasma at 400 watts was arced after 5 seconds for the remaining 20 seconds. The growth rate is linear with an R^2 value of 0.999 and a growth rate of 0.75 /cycle. This growth rate is slightly higher but in good agreement with literature values of 0.53

Å/cycle.[206] Ga_2O_3 films had an index of refraction of ~1.85-1.87 which is close to β-Ga_2O_3 at 1.89.[207]

7.3.2 Ga_2O_3 ALE

Figure 2 shows the change of Ga_2O_3 ALD films versus number of ALE cycles. An AB exposure sequence of BCl_3 and HF was used for etching. An 8 second static dose of 500 mTorr BCl_3 and a 0.75 second static dose of HF at 400 mTorr were the conditions used. The etching is linear with an R^2 value of 0.999. At 200 °C, the etch rate is 1.38 Å/cycle. The etch rate at 200 °C and these conditions varied from 1.34-1.44 Å/cycle. β-Ga_2O_3 has a monoclinic crystal structure with lattice constants a=12.23 Å, b=3.04 Å and c=5.80 Å.[208] Ga_2O_3 under these conditions is roughly an fourth of a monolayer

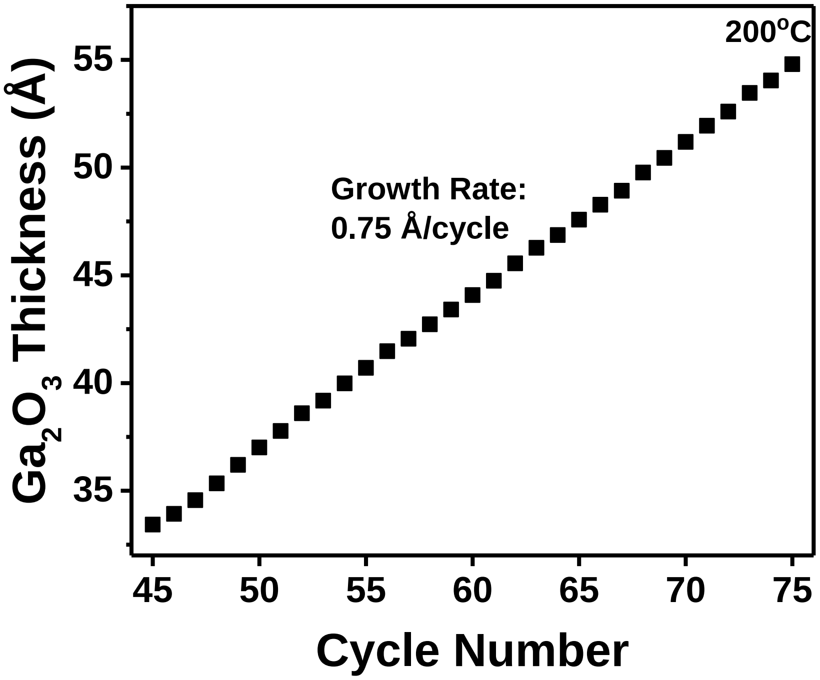

Figure 7-1. Ga_2O_3 thickness versus number of ALD cycles using TMGa and an O_2 plasma at 200 ºC. Ga_2O_3 ALD at 200 ºC has a growth rate of 0.75 Å/cycle

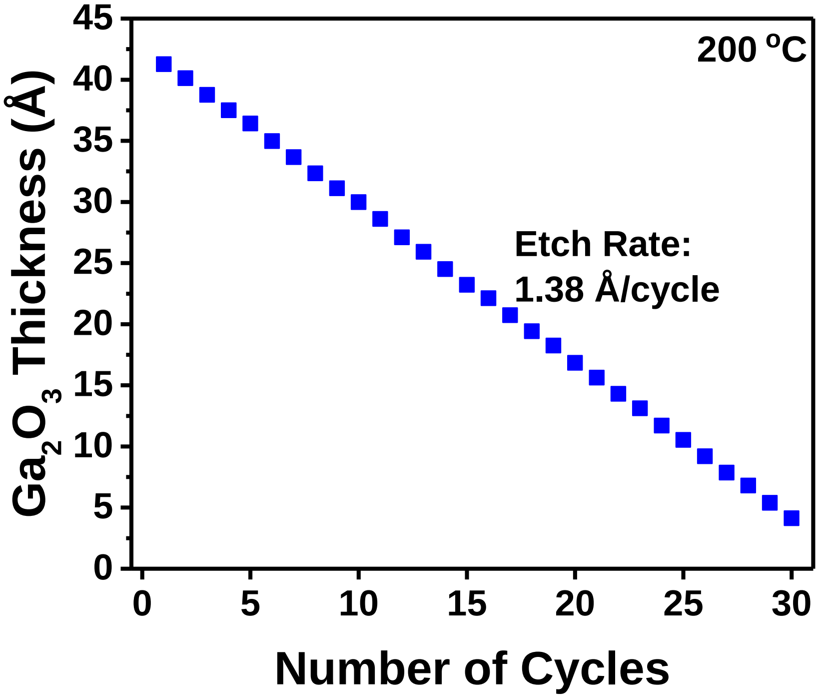

Figure 7-2. Ga_2O_3 thickness versus number of ALE cycles using BCl_3 and HF at 200 ^oC. At 200 ^oC, Ga_2O_3 has an etch rate of 1.38 Å/cycle.

7.3.3 Ga_2O_3 Self-Limiting Studies

The self-limiting behavior for Ga_2O_3 ALE were investigated using BCl_3 and HF as the reactants. Figure 3a shows the change in the etch rate for Ga_2O_3 vs BCl_3 pressure. BCl_3 pressures were varied from 140 mTorr to 1000 mTorr with constant static times of 8 seconds. HF conditions were 120 mTorr pressure for 0.75 seconds. The etch rate per cycle increases slightly as BCl_3 pressure is increased until 500 mTorr. After 500 mTorr no noticeable increase in the etch rate is seen with increasing BCl_3 pressure. The BCl_3 reaction for Ga_2O_3 ALE is self-limiting at 0.99 Å/cycle.

The self-limiting behavior for the HF half reaction is shown in figure 3b. BCl_3 was held constant at 500 mTorr held statically for 8 seconds. HF pressure was varied from 120 mTorr to 750 mTorr held statically for 0.75 seconds. Higher HF pressures result in a large increase in the etch rate until 300 mTorr. After this a slight increase in the etch rate is seen. The fast increase in the etch rate followed by a very slow increase is similar to Deal-Grove oxidation[209]. At 300 mTorr the etch rate is 1.38 Å/cycle but at 750 mTorr, the etch rate is 1.50 Å/cycle.

The self-limiting nature of BCl_3 alludes to no conversion of the surface. We reported earlier that an increase in BCl_3 pressure results in an increased etch rate for Ta_2O_5. However, with that system, no truncation of the etch rate was observed as it proceeded through a conversion etch pathway. The saturation of the BCl_3 etch rate is a result of fluorination to GaF_3 and then removal of GaF_3 forming BF_3 and $GaCl_3$ gases. In addition, we showed earlier that 100 mTorr of HF will spontaneously etch B_2O_3 at an etch rate of ~2 Å/cycle. The maximum etch rate assuming 2 Å of B_2O_3 formed would be 2.40 Å/cycle for Ga_2O_3. As the etch rate truncates, and the etch rate is much lower than the expected maximum, the pathway for Ga_2O_3 ALE with BCl_3 and HF is fluorination and ligand exchange.

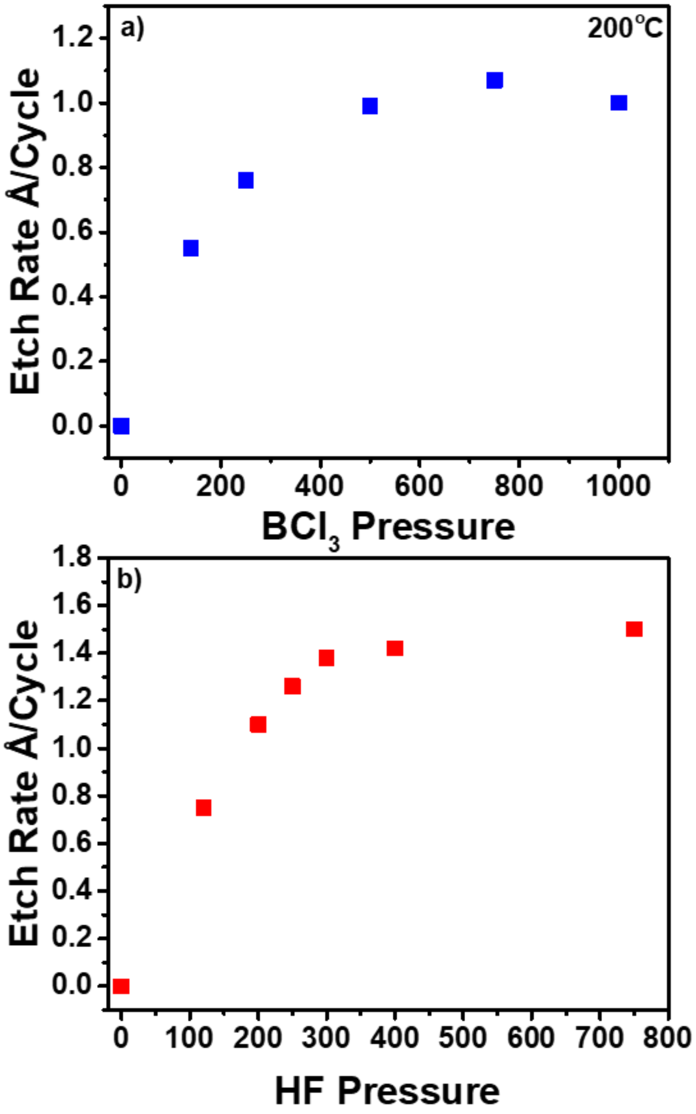

Figure 7-3. Ga_2O_3 etch rate versus reactant pressure during Ga_2O_3 ALE at 200 °C. (a) BCl_3 pressures were varied while HF conditions were held constant at 120 mTorr held statically for 0.75 seconds. (b) HF pressures were varied while BCl_3 conditions were 500 mTorr held statically for 8 seconds.

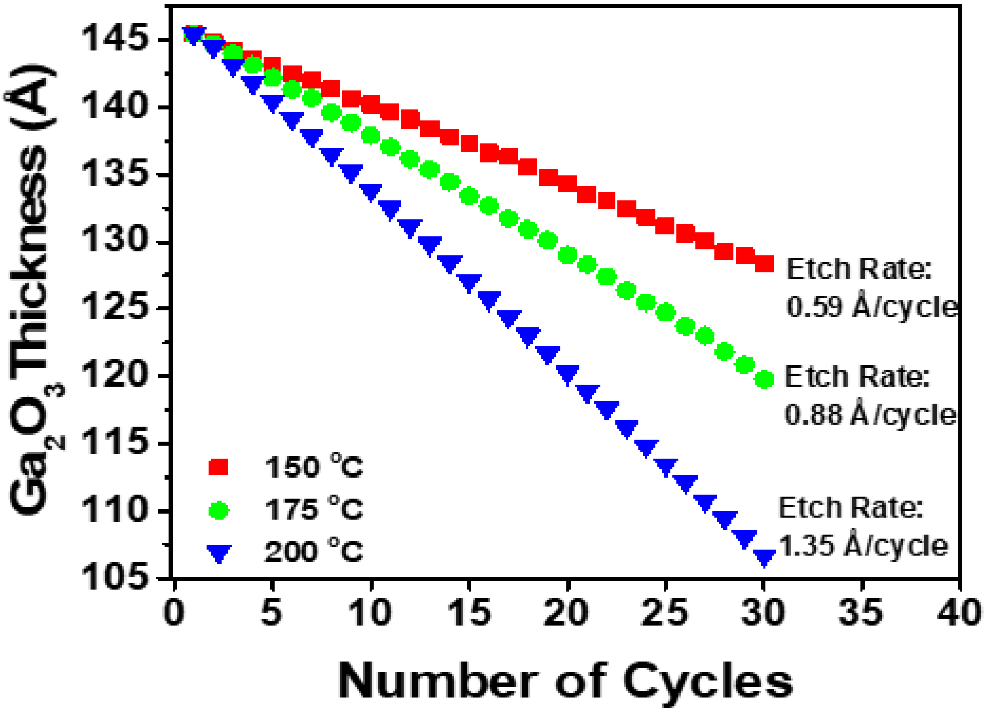

Figure 7-4. Change of Ga_2O_3 vs number of ALE cycles at 150, 175 and 200 ºC.

7.3.4 Temperature Dependence of Ga_2O_3 ALE

Ga_2O_3 ALE was conducted at various temperatures for 30 ALE cycles is shown in figure 4. An 8 second static dose of 500 mTorr BCl_3 and a 0.75 second static dose of HF at 400 mTorr were the conditions used. All Ga_2O_3 thicknesses were normalized to the thickness of 145 Å to show variation in etching at 150, 175 and 200 ^oC The Ga_2O_3 etch rate for 30 cycles at 150, 175 and 200 is 0.59, 0.88, and 1.35 Å/cycle, respectively. The increase in etch rate is a result of an increase in the GaF_3 surface layer formed.

7.4 Conclusions

Thermal etching of Ga_2O_3 films grown by ALD were demonstrated by interaction with BCl_3 and HF. An AB exposure sequence of BCl_3 and HF were used for Ga_2O_3 ALE. The BCl_3 half-reaction was shown to be self-limiting, however, the HF half reaction had a diffusion like dependence. At conditions of 500 mTorr BCl_3 held statically for 8 seconds and 400 mTorr HF held statically for 0.75 seconds, the etch rate was 1.42 Å/cycle. Ga_2O_3 ALE using BCl_3 and HF was temperature dependent with etch rates of 0.59, 0.88 and 1.34 Å/cycle at 150, 175 and 200 ^oC. The thermal ALE of Ga_2O_3 should be useful for next generation HEMT devices.

7.5 Acknowledgements

This work was funded in part by the Semiconductor Research Corporation. The authors would like to thank Scott Clendening and his team at Intel for their discussions.

Bibliography

1. Flowers, T. H., The Design of Colossus. *Annals of the History of Computting* **1983,** *5* (3), 239-252.

2. Levine, A. G., John Bardeen, William Schockley, Walter Brattain-Invention of the Transistor. *American Physical Society* **2008**.

3. Alba, M. Vacuum Tubes: The World Before Transistors. https://www.engineering.com/ElectronicsDesign/ElectronicsDesignArticles/ArticleID/16337/Vacuum-Tubes-The-World-Before-Transistors.aspx (accessed 09/17/2018).

4. Napper, D. B. The University of Manchester Celebrates the Birth of the Modern Computer. https://web.archive.org/web/20120504133240/http://www.computer50.org/.

5. Riordan, M., The Lost History of the Transistor. *IEEE Spectrum* **May 2004**, 48-49.

6. JFET. https://en.wikipedia.org/wiki/JFET.

7. Cambridge, U. o. Metal Oxide Semiconductor Field Effect Transistor (MOSFET). https://www.doitpoms.ac.uk/tlplib/semiconductors/mosfet.php (accessed 08/18).

8. Comparison of MOSFET with BJT. http://www.completepowerelectronics.com/comparison-of-mosfet-with-bjt/ (accessed 09/20/2018).

9. Moore, G. E., Cramming more components onto integrated circuits (Reprinted from Electronics, pg 114-117, April 19, 1965). *P Ieee* **1998,** *86* (1), 82-85.

10. Transistors to Transformations: From Sand to Circuits-How Intel Makes Chips. Intel, Ed. Intel: 2012.

11. Carver, C. T.; Plombon, J. J.; Romero, P. E.; Suri, S.; Tronic, T. A.; Turkot, R. B., Atomic Layer Etching: An Industry Perspective. *Ecs J Solid State Sc* **2015,** *4* (6), N5005-N5009.

12. George, S. M., Atomic Layer Deposition: An Overview. *Chem Rev* **2010,** *110* (1), 111-131.

13. Williams, J. S., Ion implantation of semiconductors. *Mat Sci Eng a-Struct* **1998,** *253* (1-2), 8-15.

14. Kanarik, K. J.; Lill, T.; Hudson, E. A.; Sriraman, S.; Tan, S.; Marks, J.; Vahedi, V.; Gottscho, R. A., Overview of atomic layer etching in the semiconductor industry. *J Vac Sci Technol A* **2015,** *33* (2).

15. Faraz, T.; Roozeboom, F.; Knoops, H. C. M.; Kessels, W. M. M., Atomic Layer Etching: What Can We Learn from Atomic Layer Deposition? *Ecs J Solid State Sc* **2015,** *4* (6), N5023-N5032.

16. Winters, H. F.; Coburn, J. W., Etching of Silicon with Xef2 Vapor. *Appl Phys Lett* **1979,** *34* (1), 70-73.

17. Donnelly, V. M.; Kornblit, A., Plasma etching: Yesterday, today, and tomorrow. *J Vac Sci Technol A* **2013,** *31* (5).

18. Kim, H. W.; Ju, B. S.; Nam, B. Y.; Yoo, W. J.; Kang, C. J.; Ahn, T. H.; Moon, J. T.; Lee, M. Y., High temperature platinum etching using Ti mask layer. *Journal of Vacuum Science & Technology a-Vacuum Surfaces and Films* **1999,** *17* (4), 2151-2155.

19. Matsui, N.; Mashimo, K.; Egami, A.; Konishi, A.; Okada, O.; Tsukada, T., Etching characteristics of magnetic materials (Co, Fe, Ni) using CO/NH3 gas plasma for hardening mask etching. *Vacuum* **2002,** *66* (3-4), 479-485.

20. George, S. M.; Lee, Y., Prospects for Thermal Atomic Layer Etching Using Sequential, Self-Limiting Fluorination and Ligand-Exchange Reactions. *Acs Nano* **2016,** *10* (5), 4889-4894.

21. Metzler, D.; Li, C.; Engelmann, S.; Bruce, R. L.; Joseph, E. A.; Oehrlein, G. S., Fluorocarbon assisted atomic layer etching of SiO2 and Si using cyclic Ar/C4F8 and Ar/CHF3 plasma. *J Vac Sci Technol A* **2016,** *34* (1).

22. Tsutsumi, T.; Kondo, H.; Hori, M.; Zaitsu, M.; Kobayashi, A.; Nozawa, T.; Kobayashi, N., Atomic layer etching of SiO2 by alternating an O-2 plasma with fluorocarbon film deposition. *J Vac Sci Technol A* **2017,** *35* (1).

23. Yoder, M. N. 1988.

24. Athavale, S. D.; Economou, D. J., Realization of atomic layer etching of silicon. *J Vac Sci Technol B* **1996,** *14* (6), 3702-3705.

25. Maki, P. A.; Ehrlich, D. J., Laser Bilayer Etching of Gaas-Surfaces. *Appl Phys Lett* **1989,** *55* (2), 91-94.

26. Sugiyama, T.; Matsuura, T.; Murota, J., Atomic-layer etching of Ge using an ultraclean ECR plasma. *Appl Surf Sci* **1997,** *112*, 187-190.

27. Park, S. D.; Lim, W. S.; Park, B. J.; Lee, H. C.; Bae, J. W.; Yeom, G. Y., Precise depth control and low-damage atomic-layer etching of HfO2 using BCl3 and Ar neutral beam. *Electrochem Solid St* **2008,** *11* (4), H71-H73.

28. Park, J. B.; Lim, W. S.; Park, S. D.; Park, Y. J.; Yeom, G. Y., Etch Characteristics of TiO2 Etched by Using an Atomic Layer Etching technique with BCl3 Gas and an Ar Neutral Beam. *J Korean Phys Soc* **2009,** *54* (3), 976-980.

29. Min, K. S.; Kang, S. H.; Kim, J. K.; Jhon, Y. I.; Jhon, M. S.; Yeom, G. Y., Atomic layer etching of Al2O3 using BCl3/Ar for the interface passivation layer of III-V MOS devices. *Microelectron Eng* **2013,** *110*, 457-460.

30. Sha, L.; Chang, J. P., Plasma etching of high dielectric constant materials on silicon in halogen chemistries. *J Vac Sci Technol A* **2004,** *22* (1), 88-95.

31. Miyawaki, Y.; Kondo, Y.; Sekine, M.; Ishikawa, K.; Hayashi, T.; Takeda, K.; Kondo, H.; Yamazaki, A.; Ito, A.; Matsumoto, H.; Hori, M., Highly Selective Etching of SiO2 over Si3N4 and Si in Capacitively Coupled Plasma Employing C5HF7 Gas. *Jpn J Appl Phys* **2013,** *52* (1).

32. Kastenmeier, B. E. E.; Matsuo, P. J.; Oehrlein, G. S., Highly selective etching of silicon nitride over silicon and silicon dioxide. *Journal of Vacuum Science & Technology a-Vacuum Surfaces and Films* **1999,** *17* (6), 3179-3184.

33. Subramanian, V.; Parvais, B.; Borremans, J.; Mercha, A.; Linten, D.; Wambacq, P.; Loo, J.; Dehan, M.; Gustin, C.; Collaert, N.; Kubicek, S.; Lander, R.; Hooker, J.; Cubaynes, F.; Donnay, S.; Jurczak, M.; Groeseneken, G.; Sansen, W.; Decoutere, S., Planar bulk MOSFETs versus FinFETs: An analog/RF perspective. *Ieee T Electron Dev* **2006,** *53* (12), 3071-3079.

34. Han, Q. H.; Meng, X. Y.; Zhang, H. Y., Challenges and Solutions to Finfet Gate Etch Process. *2015 China Semiconductor Technology International Conference* **2015**.

35. Lee, Y.; George, S. M., Atomic Layer Etching of Al2O3 Using Sequential, Self-Limiting Thermal Reactions with Sn(acac)(2) and Hydrogen Fluoride. *Acs Nano* **2015,** *9* (2), 2061-2070.

36. Lee, Y.; DuMont, J. W.; George, S. M., Mechanism of Thermal Al2O3 Atomic Layer Etching Using Sequential Reactions with Sn(acac)(2) and HF. *Chem Mater* **2015,** *27* (10), 3648-3657.

37. Lee, Y.; DuMont, J. W.; George, S. M., Atomic Layer Etching of AlF3 Using Sequential, Self-Limiting Thermal Reactions with Sn(acac)(2) and Hydrogen Fluoride. *J Phys Chem C* **2015,** *119* (45), 25385-25393.

38. Lee, Y.; DuMont, J. W.; George, S. M., Atomic Layer Etching of HfO2 Using Sequential, Self-Limiting Thermal Reactions with Sn(acac)(2) and HF. *Ecs J Solid State Sc* **2015,** *4* (6), N5013-N5022.

39. Lee, Y.; Huffman, C.; George, S. M., Selectivity in Thermal Atomic Layer Etching Using Sequential, Self Limiting Fluorination and Ligand-Exchange Reactions. *Chem Mater* **2016,** *28* (21), 7657-7665.

40. Co., J. A. W. What is Ellipsometry. https://www.jawoollam.com/resources/ellipsometry-tutorial/what-is-ellipsometry.

41. Co., J. A. W. Polarized Light. https://www.jawoollam.com/resources/ellipsometry-tutorial/polarized-light.

42. Co., J. A. W. Interaction of Light and Materials. https://www.jawoollam.com/resources/ellipsometry-tutorial/interaction-of-light-and-materials.

43. Fijiwara, H., *Spectroscopic Ellipsometry: Principles and Applications*. John Wiley & Sons: 2007.

44. Scientific, T. F. The Photoemission Process. https://sales.xpssimplified.com/whatisxps-photoemission.php.

45. Electronics, P. PHI X-Tool Automated XPS Microprobe. https://www.phi.com/surface-analysis-equipment/xtool.html.

46. Carver, C. T.; Plombon, J. J.; Romero, P. E.; Suri, S.; Tronic, T. A.; Turkot, R. B., Atomic Layer Etching: An Industry Perspective. *ECS J. Solid State Sci. Technol.* **2015,** *4* (6), N5005-N5009.

47. Donnelly, V. M.; Kornblit, A., Plasma etching: Yesterday, today, and tomorrow. *J. Vac. Sci. Technol. A* **2013,** *31* (5), 050825.

48. Kanarik, K. J.; Lill, T.; Hudson, E. A.; Sriraman, S.; Tan, S.; Marks, J.; Vahedi, V.; Gottscho, R. A., Overview of Atomic Layer Etching in the Semiconductor Industry. *J. Vac. Sci. Technol. A* **2015,** *33* (2), 020802.

49. Athavale, S. D.; Economou, D. J., Realization of Atomic Layer Etching of Silicon. *J. Vac. Sci. Technol. B* **1996,** *14* (6), 3702-3705.

50. Sugiyama, T.; Matsuura, T.; Murota, J., Atomic-Layer Etching of Ge Using an Ultraclean ECR Plasma. *Appl. Surf. Sci.* **1997,** *112*, 187-190.

51. Lim, W. S.; Park, S. D.; Park, B. J.; Yeom, G. Y., Atomic Layer Etching of (100)/(111) GaAs with Chlorine and Low Angle Forward Reflected Ne Neutral Beam. *Surf. Coat. Tech.* **2008,** *202* (22-23), 5701-5704.

52. Metzler, D.; Bruce, R. L.; Engelmann, S.; Joseph, E. A.; Oehrlein, G. S., Fluorocarbon Assisted Atomic Layer Etching of SiO_2 using Cyclic Ar/C_4F_8 Plasma. *J. Vac. Sci. Technol. A* **2014,** *32* (2), 020603.

53. Park, J. B.; Lim, W. S.; Park, B. J.; Park, I. H.; Kim, Y. W.; Yeom, G. Y., Atomic Layer Etching of Ultra-Thin HfO_2 Film for Gate Oxide in MOSFET Devices. *J. Phys. D Appl. Phys.* **2009,** *42* (5), 055202.

54. Lim, W. S.; Kim, Y. Y.; Kim, H.; Jang, S.; Kwon, N.; Park, B. J.; Ahn, J.-H.; Chung, I.; Hong, B. H.; Yeom, G. Y., Atomic Layer Etching of Graphene for Full Graphene Device Fabrication. *Carbon* **2012,** *50* (2), 429-435.

55. George, S. M.; Lee, Y., Prospects for Thermal Atomic Layer Etching Using Sequential, Self-Limiting Fluorination and Ligand-Exchange Reactions. *ACS Nano* **2016,** *10*, 4889-4894.

56. Lee, Y.; George, S. M., Atomic Layer Etching of Al_2O_3 Using Sequential, Self-Limiting Thermal Reactions with $Sn(acac)_2$ and HF. *ACS Nano* **2015,** *9*, 2061-2070.

57. Lee, Y.; DuMont, J. W.; George, S. M., Atomic Layer Etching of HfO_2 Using Sequential, Self-Limiting Thermal Reactions with $Sn(acac)_2$ and HF. *ESC J. Solid State Sci. Technol.* **2015,** *4*, N5013-N5022.

58. Lee, Y.; DuMont, J. W.; George, S. M., Trimethylaluminum as the Metal Precursor for the Atomic Layer Etching of Al_2O_3 Using Sequential, Self-Limiting Thermal Reactions. *Chem. Mater.* **2016,** *28*, 2994-3003.

59. Osakada, K., Tranmetalation. In *Fundamentals of Molecular Catalysis, Current Methods in Inorganic Chemistry, Volume 3*, Kurosawa, H.; Yamamoto, A., Eds. Elsevier Science: Amsterdam, 2003.

60. Lockhart, J. C., Redistribution and Exchange Reactions in Groups IIB-VIIB. *Chem. Rev.* **1965,** *65* (1), 131-151.

61. Lee, Y.; DuMont, J. W.; George, S. M., Atomic Layer Etching of AlF_3 Using Sequential, Self-Limiting Thermal Reactions with $Sn(acac)_2$ and Hydrogen Fluoride. *J. Phys. Chem. C* **2015,** *119* (45), 25385-25393.

62. Chen, D.; Xu, D.; Wang, J.; Zhao, B.; Zhang, Y., Dry etching of AlN films using the plasma generated by fluoride. *Vacuum* **2008,** *83* (2), 282-285.

63. Pearton, S. J.; Abernathy, C. R.; Ren, F., LOW-BIAS ELECTRON-CYCLOTRON-RESONANCE PLASMA-ETCHING OF GAN, ALN, AND INN. *Appl. Phys. Lett.* **1994,** *64* (17), 2294-2296.

64. Shul, R. J.; Willison, C. G.; Bridges, M. M.; Han, J.; Lee, J. W.; Pearton, S. J.; Abernathy, C. R.; MacKenzie, J. D.; Donovan, S. M., High-density plasma etch selectivity for the III-V nitrides. *Solid-State Electron.* **1998,** *42* (12), 2269-2276.

65. Clancey, J. W.; Cavanagh, A. S.; Kukreja, R. S.; Kongkanand, A.; George, S. M., Atomic Layer Deposition of Ultrathin Platinum Films on Tungsten Atomic Layer Deposition Adhesion Layers: Application to High Surface Area Substrates. *J. Vac. Sci. Technol. A* **2015,** *33*, 01A130.

66. Cavanagh, A. S.; Baker, L.; Clancey, J. W.; Yin, J.; Kongkanand, A.; Wagner, F. T.; George, S. M., In Situ Characterization of Plasma-Assisted Pt ALD on W ALD Adhesion Layers with Spectroscopic Ellipsometry. *ECS Trans.* **2013,** *58 (10)*, 19-26.

67. Langereis, E.; Heil, S. B. S.; Knoops, H. C. M.; Keuning, W.; van de Sanden, M. C. M.; Kessels, W. M. M., In Situ Spectroscopic Ellipsometry as a Versatile Tool for Studying Atomic Layer Deposition. *J. Phys. D: Appl. Phys.* **2009,** *42*, 073001.

68. Sternitzke, M., GROWTH OF OXIDE LAYERS ON THIN ALUMINUM NITRIDE SAMPLES MEASURED BY ELECTRON-ENERGY-LOSS SPECTROSCOPY. *J. Am. Ceram. Soc.* **1993,** *76* (9), 2289-2294.

69. Edgar, J. H.; Du, L.; Nyakiti, L.; Chaudhuri, J., Native oxide and hydroxides and their implications for bulk AlN crystal growth. *J. Cryst. Growth* **2008,** *310* (17), 4002-4006.

70. Laidani, N.; Vanzetti, L.; Anderle, M.; Basillais, A.; Boulmer-Leborgue, C.; Perriere, J., Chemical structure of films grown by AlN laser ablation: an X-ray photoelectron spectroscopy study. *Surf. Coat. Tech.* **1999,** *122* (2-3), 242-246.

71. Rosenberger, L.; Baird, R.; McCullen, E.; Auner, G.; Shreve, G., XPS analysis of aluminum nitride films deposited by plasma source molecular beam epitaxy. *Surf. Interface Anal.* **2008,** *40* (9), 1254-1261.

72. Watanabe, Y.; Hara, Y.; Tokuda, T.; Kitazawa, N.; Nakamura, Y., Surface oxidation of aluminium nitride thin films. *Surf. Eng.* **2000,** *16* (3), 211-214.

73. Profijt, H. B.; Potts, S. E.; van de Sanden, M. C. M.; Kessels, W. M. M., Plasma-Assisted Atomic Layer Deposition: Basics, Opportunities, and Challenges. *J. Vac. Sci. Technol. A* **2011,** *29*, 050801.

74. Grubbs, R. K.; George, S. M., Attenuation of hydrogen radicals traveling under flowing gas conditions through tubes of different materials. *J. Vac. Sci. Technol. A* **2006,** *24* (3), 486-496.

75. Profijt, H. B.; Kudlacek, P.; van de Sanden, M. C. M.; Kessels, W. M. M., Ion and Photon Surface Interaction During Remote Plasma ALD of Metal Oxides. *J. Electrochem. Soc.* **2011,** *158*, G88-G91.

76. Carr, J. W.; Blades, M. W., EMISSION-SPECTRA OF AN ARGON INDUCTIVELY COUPLED PLASMA IN THE VACUUM ULTRAVIOLET - BACKGROUND SPECTRA FROM 85 TO 200 NM. *Spectrochim. Acta Part B* **1984,** *39* (4), 567-574.

77. Faraz, T.; Roozeboom, F.; Knoops, H. C. M.; Kessels, W. M. M., Atomic Layer Etching: What Can We Learn from Atomic Layer Deposition? *ECS J. Solid State Sci. Technol.* **2015,** *4* (6), N5023-N5032.

78. George, S. M., Atomic Layer Deposition: An Overview. *Chem. Rev.* **2010,** *110* (1), 111-131.

79. Miikkulainen, V.; Leskela, M.; Ritala, M.; Puurunen, R. L., Crystallinity of Inorganic Films Grown by Atomic Layer Deposition: Overview and General Trends. *J. Appl. Phys.* **2013,** *113* (2), 021301.

80. Park, S. D.; Lee, D. H.; Yeom, G. Y., Atomic Layer Etching of Si(100) and Si(111) Using Cl_2 and Ar Neutral Beam. *Electrochem. Solid State Lett.* **2005,** *8* (8), C106-C109.

81. Park, S. D.; Oh, C. K.; Bae, J. W.; Yeom, G. Y.; Kim, T. W.; Song, J. I.; Jang, J. H., Atomic Layer Etching of InP Using a Low Angle Forward Reflected Ne Neutral Beam. *Appl. Phys. Lett.* **2006,** *89* (4), 043109.

82. Min, K. S.; Kang, S. H.; Kim, J. K.; Jhon, Y. I.; Jhon, M. S.; Yeom, G. Y., Atomic Layer Etching of Al_2O_3 Using BCl_3/Ar for the Interface Passivation Layer of III-V MOS Devices. *Microelectron. Eng.* **2013,** *110*, 457-460.

83. Kim, Y. Y.; Lim, W. S.; Park, J. B.; Yeom, G. Y., Layer by Layer Etching of the Highly Oriented Pyrolythic Graphite by Using Atomic Layer Etching. *J. Electrochem. Soc.* **2011,** *158* (12), D710-D714.

84. Vogli, E.; Metzler, D.; Oehrlein, G. S., Feasibility of Atomic Layer Etching of Polymer Material Based on Sequential O_2 Exposure and Ar Low-Pressure Plasma-Etching. *Appl. Phys. Lett.* **2013,** *102* (25), 253105.

85. DuMont, J. W.; George, S. M., Competition Between Al_2O_3 Atomic Layer Etching and AlF_3 Atomic Layer Deposition Using Sequential Exposures of Trimethylaluminum and Hydrogen Fluoride. *J. Chem. Phys.* **2017,** *146*, 052819.

86. Lee, Y.; DuMont, J. W.; George, S. M., Mechanism of Thermal Al_2O_3 Atomic Layer Etching Using Sequential Reactions with $Sn(acac)_2$ and HF. *Chem. Mater.* **2015,** *27* (10), 3648-3657.

87. Lee, Y.; Huffman, C.; George, S. M., Selectivity in Thermal Atomic Layer Etching Using Sequential, Self-Limiting Fluorination and Ligand-Exchange Reactions. *Chem. Mater.* **2016,** *28*, 7657-7665.

88. Johnson, N. R.; Sun, H.; Sharma, K.; George, S. M., Thermal Atomic Layer Etching of Crystalline Aluminum Nitride Using Sequential, Self-Limiting Hydrogen Fluoride and $Sn(acac)_2$ Reactions and Enhancement by H_2 and Ar Plasmas. *J. Vac. Sci. Technol. A* **2016,** *34*, 050603.

89. DuMont, J. W.; Marquardt, A. E.; Cano, A. M.; George, S. M., Thermal Atomic Layer Etching of SiO_2 by a "Conversion-Etch" Mechanism Using Sequential Reactions of Trimethylaluminum and Hydrogen Fluoride. *ACS Appl. Mater. Interfaces* **2017,** *9* (11), 10296-10307.

90. Zywotko, D. R.; George, S. M., Thermal Atomic Layer Etching of ZnO by a “Conversion-Etch” Mechanism Using Sequential Exposures of Hydrogen Fluoride and Trimethylaluminum. *Chem. Mater.* **2017,** *29*, 1183-1191.

91. Chen, Z. Z.; Qin, Z. X.; Tong, Y. Z.; Ding, X. M.; Hu, X. D.; Yu, T. J.; Yang, Z. J.; Zhang, G. Y., Etching damage and its recovery in n-GaN by reactive ion etching. *Physica B* **2003,** *334* (1-2), 188-192.

92. Adachi, S.; Susa, N., Reactive Ion Etching of Tungsten Films Sputter Deposited on GaAs. *J. Electrochem. Soc.* **1985,** *132* (12), 2980-2989.

93. Morel, T.; Bamola, S.; Ramos, R.; Beaurain, A.; Pargon, E.; Joubert, O., Tungsten Metal Gate Etching in Cl_2/O_2 Inductively Coupled High Density Plasmas. *J. Vac. Sci. Technol. B* **2008,** *26* (6), 1875-1882.

94. Tang, C. C.; Hess, D. W., Tungsten Etching in CF_4 and SF_6 Discharges. *J. Electrochem. Soc.* **1984,** *131* (1), 115-120.

95. Balooch, M.; Fischl, D. S.; Olander, D. R.; Siekhaus, W. J., The Kinetics of Tungsten Etching by Atomic and Molecular Chlorine. *J. Electrochem. Soc.* **1988,** *135* (8), 2090-2095.

96. Fischl, D. S.; Rodrigues, G. W.; Hess, D. W., Etching of Tungsten and Tungsten Silicide Films by Chlorine Atoms. *J. Electrochem. Soc.* **1988,** *135* (8), 2016-2019.

97. Bensaoula, A.; Grossman, E.; Ignatiev, A., Etching of Tungsten with XeF_2 - An X-Ray Photoelectron Spectroscopy Study. *J. Appl. Phys.* **1987,** *62* (11), 4587-4590.

98. Winters, H. F., The Etching of W(111) with XeF_2. *J. Vac. Sci. Technol. A* **1985,** *3* (3), 700-704.

99. Blain, M. G.; Jarecki, R. L.; Simonson, R. J., Chemical Downstream Etching of Tungsten. *J. Vac. Sci. Technol. A* **1998,** *16* (4), 2115-2119.

100. Peignon, M. C.; Cardinaud, C.; Turban, G., A Kinetic Study of Reactive Ion Etching of Tungsten in SF_6/O_2 Rf Plasmas. *J. Electrochem. Soc.* **1993,** *140* (2), 505-512.

101. Schloh, M. O.; Leventis, N.; Wrighton, M. S., Microfabrication of WO_3-Based Microelectrochemical Devices. *J. Appl. Phys.* **1989,** *66* (2), 965-968.

102. Strobel, A.; Schnabel, H. D.; Reinhold, U.; Rauer, S.; Neidhardt, A., Room Temperature Plasma Enhanced Atomic Layer Deposition for TiO_2 and WO_3 films. *J. Vac. Sci. Technol. A* **2016,** *34* (1), 01A118.

103. Tagtstrom, P.; Martensson, P.; Jansson, U.; Carlsson, J. O., Atomic Layer Epitaxy of Tungsten Oxide Films Using Oxyfluorides as Metal Precursors. *J. Electrochem. Soc.* **1999,** *146* (8), 3139-3143.

104. Hasper, A.; Holleman, J.; Middelhoek, J.; Kleijn, C. R.; Hoogendoorn, C. J., Modeling and Optimization of the Step Coverage of Tungsten LPCVD in Trences and Contact Holes. *J. Electrochem. Soc.* **1991,** *138* (6), 1728-1738.

105. Kofuji, N.; Mori, M.; Nishida, T., Uniform Lateral Etching of Tungsten in Deep Trenches Utilizing Reaction-Limited NF_3 Plasma Process. *Jpn. J. Appl. Phys.* **2017,** *56* (6), 06hb05.

106. Davidson, B. D.; Seghete, D.; George, S. M.; Bright, V. M., ALD Tungsten NEMS Switches and Tunneling Devices. *Sens. Actuators A* **2011,** *166* (2), 269-276.

107. Gray, J. M.; Houlton, J. P.; Gertsch, J. C.; Brown, J. J.; Rogers, C. T.; George, S. M.; Bright, V. M., Hemispherical Micro-Resonators from Atomic Layer Deposition. *J. Micromech. Microeng.* **2014,** *24* (12), 125028.

108. Liu, R.; Lin, Y. J.; Chou, L. Y.; Sheehan, S. W.; He, W. S.; Zhang, F.; Hou, H. J. M.; Wang, D. W., Water Splitting by Tungsten Oxide Prepared by Atomic Layer Deposition and Decorated with an Oxygen-Evolving Catalyst. *Angew. Chem. Int. Ed.* **2011,** *50* (2), 499-502.

109. Wetchakun, K.; Samerjai, T.; Tamaekong, N.; Liewhiran, C.; Siriwong, C.; Kruefu, V.; Wisitsoraat, A.; Tuantranont, A.; Phanichphant, S., Semiconducting Metal Oxides as Sensors for Environmentally Hazardous Gases. *Sens. Actuators B* **2011,** *160* (1), 580-591.

110. Hilfiker, J. N.; Singh, N.; Tiwald, T.; Convey, D.; Smith, S. M.; Baker, J. H.; Tompkins, H. G., Survey of methods to characterize thin absorbing films with Spectroscopic Ellipsometry. *Thin Solid Films* **2008,** *516* (22), 7979-7989.

111. Wind, R. W.; Fabreguette, F. H.; Sechrist, Z. A.; George, S. M., Nucleation Period, Surface Roughness, and Oscillations in Mass Gain per Cycle during W Atomic Layer Deposition on Al_2O_3. *J. Appl. Phys.* **2009,** *105* (7), 074309.

112. Klaus, J. W.; Ferro, S. J.; George, S. M., Atomic Layer Deposition of Tungsten Using Sequential Surface Chemistry with a Sacrificial Stripping Reaction. *Thin Solid Films* **2000,** *360* (1-2), 145-153.

113. Wilson, C. A.; Goldstein, D. N.; McCormick, J. A.; Weimer, A. W.; George, S. M., Tungsten Atomic Layer Deposition on Cobalt Nanoparticles. *J. Vac. Sci. Technol. A* **2008,** *26* (3), 430-437.

114. Wilson, C. A.; McCormick, J. A.; Cavanagh, A. S.; Goldstein, D. N.; Weimer, A. W.; George, S. M., Tungsten Atomic Layer Deposition on Polymers. *Thin Solid Films* **2008,** *516* (18), 6175-6185.

115. Clancey, J. W.; Cavanagh, A. S.; Kukreja, R. S.; Kongkanand, A.; George, S. M., Atomic Layer Deposition of Ultrathin Platinum Films on Tungsten Atomic Layer Deposition Adhesion Layers: Application to High Surface Area Substrates. *J. Vac. Sci. Technol. A* **2015,** *33* (1), 01A130.

116. Johs, B.; Hale, J. S., Dielectric Function Representation by B-Splines. *Phys. Status Solidi A* **2008,** *205* (4), 715-719.

117. Loopstra, B. O.; Rietveld, H. M., Further Refinement of Structure of WO_3. *Acta Cryst.* **1969,** *B 25*, 1420-1421.

118. Putkonen, M.; Niinistö, L., Atomic Layer Deposition of B_2O_3 Thin Films at Room Temperature. *Thin Solid Films* **2006,** *514* (1–2), 145-149.

119. Cifuentes, S. C.; Monge, M. A.; Perez, P., On the Oxidation Mechanism of Pure Tungsten in the Temperature Range 600-800 C. *Corros. Sci.* **2012,** *57*, 114-121.

120. Gulbransen, E. A.; Andrew, K. F., Kinetics of the Oxidation of Pure Tungsten from 500 C to 1300 C. *J. Electrochem. Soc.* **1960,** *107* (7), 619-628.

121. King, D. A.; Madey, T. E.; Yates, J. T., Interaction of Oxygen with Polycrystalline Tungsten. 2. Corrosive Oxidation. *J. Chem. Phys.* **1971,** *55* (7), 3247-3253.

122. Gulbransen, E. A.; Wysong, W. S., Thin Oxide Films on Tungsten. *T. Am. I. Min. Met. Eng.* **1948,** *175*, 611-627.

123. Sohal, R.; Walczyk, C.; Zaumseil, P.; Wolansky, D.; Fox, A.; Tillack, B.; Mussig, H. J.; Schroeder, T., Thermal Oxidation of Chemical Vapour Deposited Tungsten Layers on Silicon Substrates for Embedded Non-Volatile Memory Application. *Thin Solid Films* **2009,** *517* (16), 4534-4539.

124. Warren, A.; Nylund, A.; Olefjord, I., Oxidation of Tungsten and Tungsten Carbide in Dry and Humid Atmospheres. *Int. J. Refract. Met. H.* **1996,** *14* (5-6), 345-353.

125. Deal, B. E.; Grove, A. S., General Relationship for Thermal Oxidation of Silicon. *J. Appl. Phys.* **1965,** *36* (12), 3770-3778.

126. King, D. A.; Madey, T. E.; Yates, J. T., Interaction of Oxygen with Polycrystalline Tungsten. 1. Sticking Probabilities and Desorption Spectra. *J. Chem. Phys.* **1971,** *55* (7), 3236-3246.

127. Kim, J. K.; Nam, S. W.; Cho, S. I.; Jhon, M. S.; Min, K. S.; Kim, C. K.; Jung, H. B.; Yeom, G. Y., Study on the Oxidation and Reduction of Tungsten Surface for sub-50 nm Patterning Process. *J. Vac. Sci. Technol. A* **2012,** *30* (6), 061305.

128. Romanyuk, A.; Melnik, V.; Oelhafen, P., Oxidation of Tungsten Surface with Reactive Oxygen Plasma. *Nucl. Instrum. Methods Phys. Res. B* **2005,** *232*, 358-361.

129. Xu, S. L.; Diao, L., Study of Tungsten Oxidation in $O_2/H_2/N_2$ Downstream Plasma. *J. Vac. Sci. Technol. A* **2008,** *26* (3), 360-364.

130. Lee, Y.; George, S. M., Thermal Atomic Layer Etching of Titanium Nitride Using Sequential, Self-Limiting Reactions: Oxidation to TiO_2 and Fluorination to Volatile TiF_4. *Submitted to Chem. Mater.* **2017**.

131. Metzler, D.; Bruce, R. L.; Engelmann, S.; Joseph, E. A.; Oehrlein, G. S., Fluorocarbon assisted atomic layer etching of SiO2 using cyclic Ar/C4F8 plasma. *J Vac Sci Technol A* **2014,** *32* (2).

132. Lee, Y. H.; Chen, M. M.; Ahn, K. Y.; Bright, A. A., Reactive Etching Mechanism of Tungsten Silicide in Cf4-O2 Plasma. *Thin Solid Films* **1984,** *118* (2), 149-154.

133. Lim, W. S.; Park, S. D.; Park, B. J.; Yeom, G. Y., Atomic layer etching of (100)/(111) GaAs with chlorine and low angle forward reflected Ne neutral beam. *Surf Coat Tech* **2008,** *202* (22-23), 5701-5704.

134. Lim, W. S.; Kim, Y. Y.; Kim, H.; Jang, S.; Kwon, N.; Park, B. J.; Ahn, J. H.; Chung, I.; Hong, B. H.; Yeom, G. Y., Atomic layer etching of graphene for full graphene device fabrication. *Carbon* **2012,** *50* (2), 429-435.

135. Park, J. B.; Lim, W. S.; Park, B. J.; Park, I. H.; Kim, Y. W.; Yeom, G. Y., Atomic layer etching of ultra-thin HfO2 film for gate oxide in MOSFET devices. *J Phys D Appl Phys* **2009,** *42* (5).

136. Johnson, N. R.; Sun, H.; Sharma, K.; George, S. M., Thermal atomic layer etching of crystalline aluminum nitride using sequential, self-limiting hydrogen fluoride and Sn(acac)2 reactions and enhancement by H2 and Ar plasmas. *Journal of Vacuum Science & Technology A: Vacuum, Surfaces, and Films* **2016,** *34* (5), 050603.

137. Zywotko, D. R.; George, S. M., Thermal Atomic Layer Etching of ZnO by a “Conversion-Etch” Mechanism Using Sequential Exposures of Hydrogen Fluoride and Trimethylaluminum. *Chem Mater* **2017,** *29* (3), 1183-1191.

138. DuMont, J. W.; Marquardt, A. E.; Cano, A. M.; George, S. M., Thermal Atomic Layer Etching of SiO2 by a “Conversion-Etch” Mechanism Using Sequential Reactions of Trimethylaluminum and Hydrogen Fluoride. *ACS Applied Materials & Interfaces* **2017,** *9* (11), 10296-10307.

139. Johnson, N. R.; George, S. M., WO3 and W Thermal Atomic Layer Etching Using "Conversion-Fluorination" and "Oxidation-Conversion-Fluorination" Mechanisms. *Acs Appl Mater Inter* **2017,** *9* (39), 34435-34447.

140. Zhu, H.; Yuan, H.; Li, H. T.; Richter, C. A.; Kirillov, O.; Ioannou, D. E.; Li, Q. L., Design and Fabrication of Ta2O5 Stacks for Discrete Multibit Memory Application. *Ieee T Nanotechnol* **2013,** *12* (6), 1151-1157.

141. Wang, X. G.; Liu, J.; Bai, W. P.; Kwong, D. L., A novel MONOS-type nonvolatile memory using high-k dielectrics for improved data retention and programming speed. *Ieee T Electron Dev* **2004,** *51* (4), 597-602.

142. Salun, A. L.; Mantoux, A.; Blanquet, E.; Djurado, E., ESD and ALD Depositions of Ta2O5 Thin Films Investigated as Barriers to Copper Diffusion for Advanced Metallization. *J Electrochem Soc* **2009,** *156* (5), H311-H315.

143. Lintanf-Salaun, A.; Mantoux, A.; Djurado, E.; Blanquet, E., Atomic layer deposition of tantalum oxide thin films for their use as diffusion barriers in microelectronic devices. *Microelectron Eng* **2010,** *87* (3), 373-378.

144. Bartic, C.; Jansen, H.; Campitelli, A.; Borghs, S., Ta2O5 as gate dielectric material for low-voltage organic thin-film transistors. *Org Electron* **2002,** *3* (2), 65-72.

145. Chen, J. D.; Wang, X. P.; Li, M. F.; Lee, S. J.; Yu, M. B.; Shen, C.; Yeo, Y. C., NMOS compatible work function of TaN metal gate with erbium-oxide-doped hafnium oxide gate dielectric. *Ieee Electr Device L* **2007,** *28* (10), 862-864.

146. Burton, B. B.; Lavoie, A. R.; George, S. M., Tantalum nitride atomic layer deposition using (tert-butylimido) tris(diethylamido) tantalum and hydrazine. *J Electrochem Soc* **2008,** *155* (7), D508-D516.

147. Aarik, J.; Kukli, K.; Aidla, A.; Pung, L., Mechanisms of suboxide growth and etching in atomic layer deposition of tantalum oxide from TaCl5 and H2O. *Appl Surf Sci* **1996,** *103* (4), 331-341.

148. Kukli, K.; Aarik, J.; Aidla, A.; Forsgren, K.; Sundqvist, J.; Harsta, A.; Uustare, T.; Mandar, H.; Kiisler, A. A., Atomic layer deposition of tantalum oxide thin films from iodide precursor. *Chem Mater* **2001,** *13* (1), 122-128.

149. Ibbotson, D. E.; Mucha, J. A.; Flamm, D. L.; Cook, J. M., Selective Interhalogen Etching of Tantalum Compounds and Other Semiconductor-Materials. *Appl Phys Lett* **1985,** *46* (8), 794-796.

150. Jenkins, W. A.; Cook, C. M., Tantalum Oxychloride. *J Inorg Nucl Chem* **1959,** *11* (2), 163-164.

151. Lee, K. P.; Jung, K. B.; Singh, R. K.; Pearton, S. J.; Hobbs, C.; Tobin, P., Inductively coupled plasma etching of Ta2O5. *J Electrochem Soc* **1999,** *146* (10), 3794-3798.

152. Lee, K. P.; Jung, K. B.; Singh, R. K.; Pearton, S. J.; Hobbs, C.; Tobin, P., Comparison of plasma chemistries for dry etching of Ta2O5. *Journal of Vacuum Science & Technology a-Vacuum Surfaces and Films* **2000,** *18* (4), 1169-1172.

153. Kuo, Y., Reactive Ion Etching of Sputter Deposited Tantalum Oxide and Its Etch Selectivity to Tantalum. *J Electrochem Soc* **1992,** *139* (2), 579-583.

154. Seki, S.; Unagami, T.; Tsujiyama, B., Reactive Ion Etching of Tantalum Pentoxide. *J Electrochem Soc* **1983,** *130* (12), 2505-2506.

155. Shimada, H.; Maruyama, K., Highly selective etching of tantalum electrode to thin gate dielectrics using SiCl4-NF3 gas mixture plasma. *Jpn J Appl Phys 1* **2004,** *43* (4B), 1768-1772.

156. Hwang, W. S.; Chen, J. H.; Yoo, W. J.; Bliznetsov, V., Investigation of etching properties of metal nitride/high-k gate stacks using inductively coupled plasma. *J Vac Sci Technol A* **2005,** *23* (4), 964-970.

157. Shin, M. H.; Na, S. W.; Lee, N. E.; Oh, T. K.; Kim, J.; Lee, T.; Ahn, J., Dry etching of TaN/HfO2 gate stack structure by Cl-2/SF6/Ar inductively coupled plasma. *Japanese Journal of Applied Physics Part 1-Regular Papers Brief Communications & Review Papers* **2005,** *44* (7B), 5811-5818.

158. Nakamura, K.; Kitagawa, T.; Osari, K.; Takahashi, K.; Ono, K., Plasma etching of high-k and metal gate materials. *Vacuum* **2006,** *80* (7), 761-767.

159. Shin, M. H.; Park, M. S.; Lee, N. E.; Kim, J.; Kim, C. Y.; Ahn, J., Dry etching of TaN/HfO2 gate-stack structure in BCl3/Ar/O-2 inductively coupled plasmas. *J Vac Sci Technol A* **2006,** *24* (4), 1373-1379.

160. Um, D. S.; Woo, J. C.; Kim, C. I., Etching characteristics of TaN thin film using an inductively coupled plasma. *Surf Coat Tech* **2010,** *205*, S333-S336.

161. Clancey, J. W.; Cavanagh, A. S.; Kukreja, R. S.; Kongkanand, A.; George, S. M., Atomic layer deposition of ultrathin platinum films on tungsten atomic layer deposition adhesion layers: Application to high surface area substrates. *J Vac Sci Technol A* **2015,** *33* (1).

162. Henke, T.; Knaut, M.; Geidel, M.; Winkler, F.; Albert, M.; Bartha, J. W., Atomic layer deposition of tantalum oxide thin films using the precursor tert-butylimido-tris-ethylmethylamido-tantalum and water: Process characteristics and film properties. *Thin Solid Films* **2017,** *627*, 94-105.

163. Lee, Y.; George, S. M., Thermal Atomic Layer Etching of Titanium Nitride Using Sequential, Self-Limiting Reactions: Oxidation to TiO2 and Fluorination to Volatile TiF4. *Chem Mater* **2017,** *29* (19), 8202-8210.

164. Yamagishi, H.; Miyauchi, M., Thermal-Oxidation of Sputtered Tan Films and Properties of the Oxidized Films. *Japanese Journal of Applied Physics Part 1-Regular Papers Short Notes & Review Papers* **1987,** *26* (6), 852-855.

165. Adams, J. R.; Kramer, D. K., Study of Oxidation of Tantalum Nitride by Ellipsometry and Auger-Electron Spectroscopy. *Surf Sci* **1976,** *56* (1), 482-487.

166. Brady, D. P.; Fuss, F. N.; Gerstenberg, D., Thermal-Oxidation and Resistivity of Tantalum Nitride Films. *Thin Solid Films* **1980,** *66* (3), 287-302.

167. Kim, Y. Y.; Lim, W. S.; Park, J. B.; Yeom, G. Y., Layer by Layer Etching of the Highly Oriented Pyrolythic Graphite by Using Atomic Layer Etching. *J Electrochem Soc* **2011,** *158* (12), D710-D714.

168. Vogli, E.; Metzler, D.; Oehrlein, G. S., Feasibility of atomic layer etching of polymer material based on sequential O-2 exposure and Ar low-pressure plasma-etching. *Appl Phys Lett* **2013,** *102* (25).

169. Park, S. D.; Oh, C. K.; Bae, J. W.; Yeom, G. Y.; Kim, T. W.; Song, J. I.; Jang, J. H., Atomic layer etching of InP using a low angle forward reflected Ne neutral beam. *Appl Phys Lett* **2006,** *89* (4).

170. Johnson, N. R.; Sun, H. X.; Sharma, K.; George, S. M., Thermal atomic layer etching of crystalline aluminum nitride using sequential, self-limiting hydrogen fluoride and Sn(acac)(2) reactions and enhancement by H-2 and Ar plasmas. *J Vac Sci Technol A* **2016,** *34* (5).

171. DuMont, J. W.; George, S. M., Competition between Al2O3 atomic layer etching and AlF3 atomic layer deposition using sequential exposures of trimethylaluminum and hydrogen fluoride. *J Chem Phys* **2017,** *146* (5).

172. Zywotko, D. R.; George, S. M., Thermal Atomic Layer Etching of ZnO by a "Conversion-Etch" Mechanism Using Sequential Exposures of Hydrogen Fluoride and Trimethylaluminum. *Chem Mater* **2017,** *29* (3), 1183-1191.

173. DuMont, J. W.; Marquardt, A. E.; Cano, A. M.; George, S. M., Thermal Atomic Layer Etching of SiO2 by a "Conversion-Etch" Mechanism Using Sequential Reactions of Trimethylaluminum and Hydrogen Fluoride. *Acs Appl Mater Inter* **2017,** *9* (11), 10296-10307.

174. Chen, J. K. C.; Altieri, N. D.; Kim, T.; Chen, E.; Lill, T.; Shen, M. H.; Chang, J. P., Directional etch of magnetic and noble metals. II. Organic chemical vapor etch. *J Vac Sci Technol A* **2017,** *35* (5).

175. Lemaire, P. C.; Parsons, G. N., Thermal Selective Vapor Etching of TiO2: Chemical Vapor Etching via WF6 and Self-Limiting Atomic Layer Etching Using WF6 and BCl3. *Chem Mater* **2017,** *29* (16), 6653-6665.

176. Xie, W. Y.; Lemaire, P. C.; Parsons, G. N., Thermally Driven Self-Limiting Atomic Layer Etching of Metallic Tungsten Using WF6 and O-2. *Acs Appl Mater Inter* **2018,** *10* (10), 9147-9154.

177. Rosli, S. A.; Aziz, A. A., Etch characteristics of GaN using inductively coupled Cl-2 plasma etching. *Aip Conf Proc* **2008,** *1017*, 353-357.

178. Kim, D. W.; Jeong, C. H.; Lee, H. Y.; Kim, H. S.; Sung, Y. J.; Yeom, G. Y., A study of GaN etching characteristics using HBr-based inductively coupled plasmas. *Solid State Electron* **2003,** *47* (3), 549-552.

179. Kim, H. S.; Lee, Y. J.; Lee, Y. H.; Lee, J. W.; Yoo, M. C.; Kim, T. I.; Yeom, G. Y., Etch characteristics of GaN using inductively coupled Cl-2/HBr and Cl-2/Ar plasmas. *Mater Res Soc Symp P* **1997,** *468*, 367-372.

180. Lee, Y. H.; Kim, H. S.; Yeom, G. Y.; Lee, J. W.; Yoo, M. C.; Kim, T. I., Etch characteristics of GaN using inductively coupled Cl-2/Ar and Cl-2/BCl3 plasmas. *Journal of Vacuum Science & Technology a-Vacuum Surfaces and Films* **1998,** *16* (3), 1478-1482.

181. Oubensaid, E. H.; Duluard, C. Y.; Pichon, L. E.; Pereira, J.; Boufnichel, M.; Lefaucheux, P.; Dussart, R.; Ranson, P., Effect of the addition of SF6 and N-2 in inductively coupled SiCl4 plasma for GaN etching. *Semicond Sci Tech* **2009,** *24* (7).

182. Hiramatsu, K.; Matsushima, H.; Hanai, H.; Sawaki, N., Selective area etching of GaN and AlGaN by thermally chemical reaction in hydrogen ambient. *Nitride Semiconductors* **1998,** *482*, 991-996.

183. Kauppinen, C.; Khan, S. A.; Sundqvist, J.; Suyatin, D. B.; Suihkonen, S.; Kauppinen, E. I.; Sopanen, M., Atomic layer etching of gallium nitride (0001). *J Vac Sci Technol A* **2017,** *35* (6).

184. Ohba, T.; Yang, W. B.; Tan, S.; Kanarik, K. J.; Nojiri, K., Atomic layer etching of GaN and AlGaN using directional plasma-enhanced approach. *Jpn J Appl Phys* **2017,** *56* (6).

185. Zhuang, D.; Edgar, J. H., Wet etching of GaN, AlN, and SiC: a review. *Mat Sci Eng R* **2005,** *48* (1), 1-46.

186. Denbaars, S. P., Gallium-nitride-based materials for blue to ultraviolet optoelectronics devices. *P Ieee* **1997,** *85* (11), 1740-1749.

187. Ming, B. M.; Wang, R. Z.; Yam, C. Y.; Xu, L. C.; Lau, W. M.; Yan, H., Bandgap engineering of GaN nanowires. *Aip Adv* **2016,** *6* (5).

188. Zhu, D.; Wallis, D. J.; Humphreys, C. J., Prospects of III-nitride optoelectronics grown on Si. *Rep Prog Phys* **2013,** *76* (10).

189. Mishra, U. K.; Shen, L.; Kazior, T. E.; Wu, Y. F., GaN-Based RF power devices and amplifiers. *P Ieee* **2008,** *96* (2), 287-305.

190. Pearton, S. J.; Ren, F., GaN electronics. *Adv Mater* **2000,** *12* (21), 1571-+.

191. Son, D. H.; Jo, Y. W.; Seo, J. H.; Won, C. H.; Im, K. S.; Lee, Y. S.; Jang, H. S.; Kim, D. H.; Kang, I. M.; Lee, J. H., Low voltage operation of GaN vertical nanowire MOSFET. *Solid State Electron* **2018,** *145*, 1-7.

192. Huang, J. Y.; Zheng, H.; Mao, S. X.; Li, Q. M.; Wang, G. T., In Situ Nanomechanics of GaN Nanowires. *Nano Lett* **2011,** *11* (4), 1618-1622.

193. Bermudez, V. M., Investigation of the initial chemisorption and reaction of fluorine (XeF2) with the GaN(0001)-(1x1) surface. *Appl Surf Sci* **1997,** *119* (1-2), 147-159.

194. Leszczynski, M.; Suski, T.; Perlin, P.; Teisseyre, H.; Grzegory, I.; Bockowski, M.; Jun, J.; Porowski, S.; Major, J., Lattice-Constants, Thermal-Expansion and Compressibility of Gallium Nitride. *J Phys D Appl Phys* **1995,** *28* (4a), A149-A153.

195. George, S.; Lee, Y.; DuMont, J.; Johnson, N.; Zywotko, D., Atomic Layer Etching (ALE) using sequential thermal reactions: Atomic Layer Deposition (ALD) in reverse. *Abstr Pap Am Chem S* **2017,** *253*.

196. Lee, Y.; DuMont, J. W.; George, S. M., Trimethylaluminum as the Metal Precursor for the Atomic Layer Etching of Al2O3 Using Sequential, Self-Limiting Thermal Reactions. *Chem Mater* **2016,** *28* (9), 2994-3003.

197. Higashiwaki, M.; Sasaki, K.; Kuramata, A.; Masui, T.; Yamakoshi, S., Gallium oxide (Ga2O3) metal-semiconductor field-effect transistors on single-crystal beta-Ga2O3 (010) substrates. *Appl Phys Lett* **2012,** *100* (1).

198. Higashiwaki, M.; Jessen, G. H., Guest Editorial: The dawn of gallium oxide microelectronics. *Appl Phys Lett* **2018,** *112* (6).

199. Baliga, B. J., Semiconductors for High-Voltage, Vertical Channel Field-Effect Transistors. *J Appl Phys* **1982,** *53* (3), 1759-1764.

200. Ghosh, K.; Singisetti, U., Ab initio velocity-field curves in monoclinic beta-Ga2O3. *J Appl Phys* **2017,** *122* (3).

201. Canali, C.; Ottaviani, G., Saturation Values of Electron Drift Velocity in Silicon between 300 Degrees K and 4.2 Degrees K. *Phys Lett A* **1970,** *A 32* (3), 147-+.

202. Sasaki, K.; Thieu, Q. T.; Wakimoto, D.; Koishikawa, Y.; Kuramata, A.; Yamakoshi, S., Depletion-mode vertical Ga2O3 trench MOSFETs fabricated using Ga2O3 homoepitaxial films grown by halide vapor phase epitaxy. *Appl Phys Express* **2017,** *10* (12).

203. Higashiwaki, M.; Sasaki, K.; Kamimura, T.; Wong, M. H.; Krishnamurthy, D.; Kuramata, A.; Masui, T.; Yamakoshi, S., Depletion-mode Ga2O3 metal-oxide-semiconductor field-effect transistors on beta-Ga2O3 (010) substrates and temperature dependence of their device characteristics. *Appl Phys Lett* **2013,** *103* (12).

204. Shih, H. Y.; Chu, F. C.; Das, A.; Lee, C. Y.; Chen, M. J.; Lin, R. M., Atomic Layer Deposition of Gallium Oxide Films as Gate Dielectrics in AlGaN/GaN Metal-Oxide-Semiconductor High-Electron-Mobility Transistors. *Nanoscale Res Lett* **2016,** *11*, 1-9.

205. *HSC Chemistry*, Outokumpu Research: Oy:Port Finland.

206. Donmez, I.; Ozgit-Akgun, C.; Biyikli, N., Low temperature deposition of Ga2O3 thin films using trimethylgallium and oxygen plasma. *J Vac Sci Technol A* **2013,** *31* (1).

207. Rebien, M.; Henrion, W.; Hong, M.; Mannaerts, J. P.; Fleischer, M., Optical properties of gallium oxide thin films. *Appl Phys Lett* **2002,** *81* (2), 250-252.

208. Geller, S., Crystal Structure of Beta-Ga2o3. *J Chem Phys* **1960,** *33* (3), 676-684.

209. Deal, B. E.; Grove, A. S., General Relationship for Thermal Oxidation of Silicon. *J Appl Phys* **1965,** *36* (12), 3770-&.